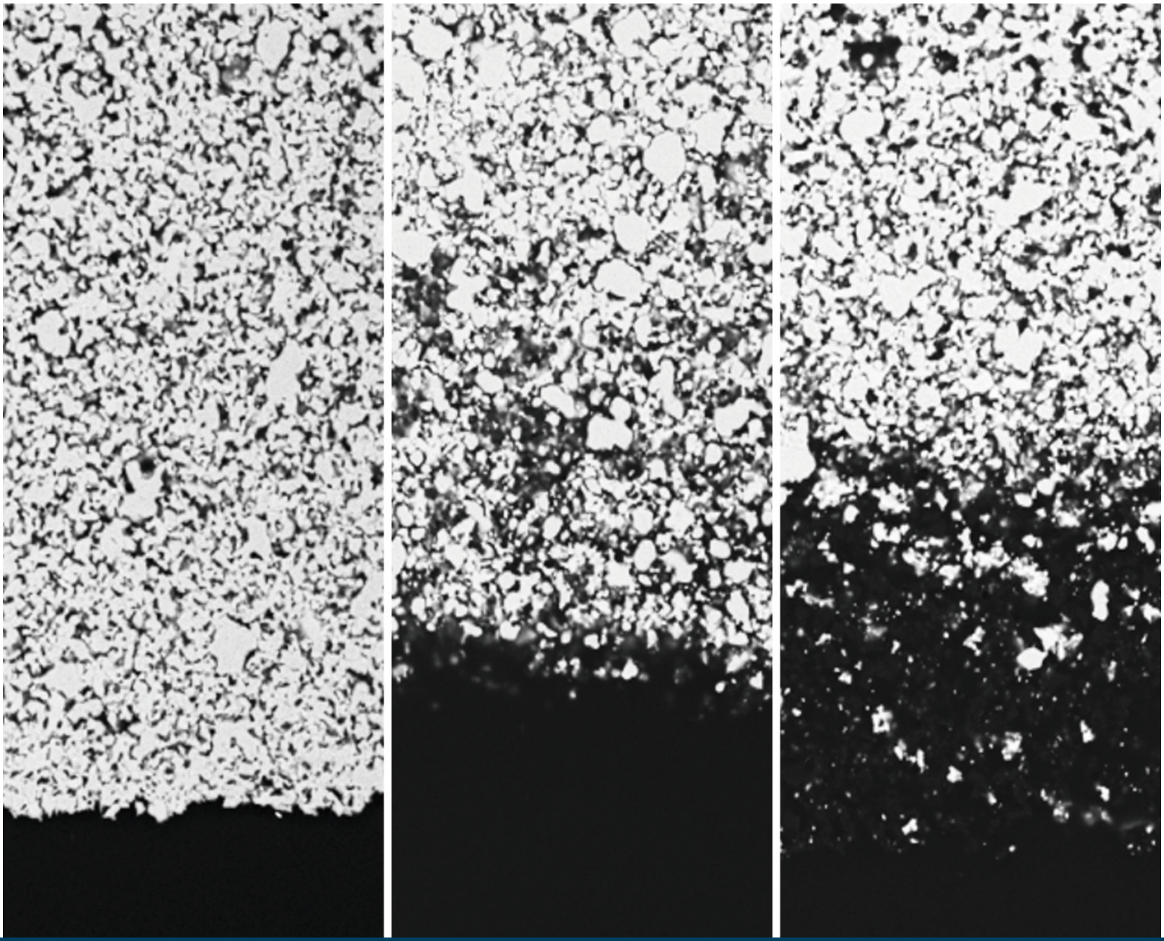

Coupling a Solid Oxide Fuel Cell with a Biomass Gasifier: Degradation Mechanisms and Alternative Anode Materials

Hyeondeok Jeong

Energie & Umwelt / Energy & Environment
Band / Volume 460
ISBN 978-3-95806-398-3

Mitglied der Helmholtz-Gemeinschaft

JÜLICH
Forschungszentrum

Schriften des Forschungszentrums Jülich
Reihe Energie & Umwelt / Energy & Environment Band / Volume 460

Forschungszentrum Jülich GmbH
Institut für Energie- und Klimaforschung
Werkstoffsynthese und Herstellungsverfahren (IEK-1)

Coupling a Solid Oxide Fuel Cell with a Biomass Gasifier: Degradation Mechanisms and Alternative Anode Materials

Hyeondeok Jeong

Schriften des Forschungszentrums Jülich
Reihe Energie & Umwelt / Energy & Environment Band / Volume 460

ISSN 1866-1793 ISBN 978-3-95806-398-3

Bibliografische Information der Deutschen Nationalbibliothek.
Die Deutsche Nationalbibliothek verzeichnet diese Publikation in der
Deutschen Nationalbibliografie; detaillierte Bibliografische Daten
sind im Internet über http://dnb.d-nb.de abrufbar.

Herausgeber und Vertrieb: Forschungszentrum Jülich GmbH
Zentralbibliothek, Verlag
52425 Jülich
Tel.: +49 2461 61-5368
Fax: +49 2461 61-6103
zb-publikation@fz-juelich.de
www.fz-juelich.de/zb

Umschlaggestaltung: Grafische Medien, Forschungszentrum Jülich GmbH

Druck: Grafische Medien, Forschungszentrum Jülich GmbH

Schriften des Forschungszentrums Jülich
Reihe Energie & Umwelt / Energy & Environment, Band / Volume 460

D 82 (Diss., RWTH Aachen University, 2019)

ISSN 1866-1793
ISBN 978-3-95806-398-3

Abstract

Anode-supported solid oxide fuel cells (SOFCs) with a state-of-the-art Ni/YSZ anode have been tested in simulated bio-syngas with controlled addition of tars and sulfur as model molecules to study the influence of impurities on the degradation of SOFCs. The phenol tar causes macro- and micro-scale structural changes in the support including erosion, Ni coarsening, and carbon fiber formation. However, the effect of phenol on the cell performance was not pronounced below a content of 8 g/Nm^3 in the few hundreds of hour test period. On the other hand, the cell responded immediately after 0.5 g/Nm^3 of naphthalene were added in the fuel. There was no microstructure change and the carbon deposition was found only on the surface of the support. A stack test with real bio-syngas derived from wood pellets showed more practical problems. The stack showed considerable performance degradation and the test was stopped after 5 hours of operation due to an increase of the pressure drop. There were heavy carbon depositions at the support surface and the Ni mesh current collector. The microstructure change of support was also observed near and under the carbon deposition area, and the Ni metal dusting behavior was observed from the Ni particles in support and Ni mesh current collector.

Ni/gadolinia-doped-ceria (GDC) anode was implemented instead of Ni/YSZ as an alternative anode material. The ceria-based anodes are expected to show superior electrochemical performance and enhanced sulfur and coking tolerance in comparison to the zirconia-based anodes. However, the cell performance of a Ni/GDC anode cell decreased approximately by 50% compared to the standard Ni/YSZ cell. The performance loss is attributed to inter-diffusion of ceria and zirconia during cell fabrication between YSZ electrolyte and GDC in anode layer, because the YSZ-GDC mixed phase has poor electrical properties and the different diffusion rates of Gd^{3+} and Ce^{4+} in YSZ and Y^{3+} and Zr^{4+} GDC cause pore formation (Kirkendall voids) and Ni agglomeration in the anode layer. In the cell test of Ni/GDC anode cell with bio-syngas, the electrochemical degradation was faster than in Ni/YSZ anode cell.

Another alternative for a sulfur- and coking-tolerant anode was molybdenum (Mo) containing materials, which are known as excellent desulfurization material. Various kinds of Mo containing precursors such as MoO_3, $NiMoO_4$, $Ce_{1-x}Mo_xO_{2+\delta}$ (CMO), and $Ce_{1-x}Gd_{0.1}Mo_xO_{2+\delta}$ (CGMO) were tried for screen printing. However, the sintering temperature of anode and/or electrolyte layer was limited due to the poor thermal stability of Mo. Other manufacturing processes were attempted to keep the Mo in the anode layer, such as gas diffusion and thermal diffusion, but the results showed either the absence of Mo in the anode layer or an unsuitable microstructure for cell tests. An electrolyte supported cell was prepared with Ni/GDC anode and Mo solution was infiltrated to the anode. The cell performance and sulfur tolerance were improved by Mo infiltration.

Kurzfassung

Ziel der vorliegenden Arbeit war die Untersuchung des Einflusses von Verunreinigungen des Brenngases auf die Degradation von anodengestützten Festoxidbrennstoffzellen. Hierfür wurden elektrochemische Einzelzellmessungen von Zellen mit gängiger Ni/YSZ Anode in simuliertem Bio-Synthesegas unter kontrollierter Zugabe von Teer- und Schwefelspezies durchgeführt. Teer-Zugabe in Form von Phenol verursacht makro- und mikrostrukturelle Veränderungen des Anodensubstrats, wie Erosion, Ni-Vergröberung und faserförmige Ablagerungen von Kohlenstoff. Eine erhebliche Verringerung der Zellleistung wurde jedoch erst ab einer Phenol-Zugabe in Höhe von 8 g/Nm^3 über eine Testdauer von einigen hundert Stunden beobachtet. Im Gegensatz hierzu verursacht Naphthalin schon bei einer Zugabe von 0,5 g/Nm^3 eine signifikante Beeinträchtigung der Zellleistung. Die Nachuntersuchung zeigte keine Hinweise auf eine Mikrostrukturänderung und Kohlenstoffablagerungen beschränkten sich auf die Substratoberfläche. In einem Stacktest mit aus Holzpellets gewonnenem realem Bio-Synthesegas wurde eine erhebliche Leistungsdegradation beobachtet. Die Ablagerung großer Mengen Kohlenstoff an der Substratoberfläche und im Bereich des als Stromsammler verwendeten Ni-Netzes verursachte einen hohen Druckverlust in der Brenngasversorgung, so dass der Test schon nach fünf Betriebsstunden beendet werden musste. Im Bereich der Kohlenstoffabscheidungen wurde eine Mikrostrukturänderung des Substrats ermittelt. Korrosion der Ni Partikel des Substrats und des Ni Kontaktnetzes durch „Metal Dusting“ wurde nachgewiesen.

Anoden mit Ni und Gd dotiertem Ceroxid (Ni/GDC) wurden als Alternative zu Ni/YSZ untersucht. Ceroxid-basierte Anoden versprechen eine verbesserte elektrochemische Leistungsfähigkeit als auch eine erhöhte Resistenz gegenüber S- und C-haltigen Verunreinigungen im Vergleich zu Ni/YSZ. Die in den gegenwärtigen Versuchen ermittelte um etwa 50 % verringerte Leistung der Zellen mit Ni/GDC Anode wird Interdiffusionsphänomenen zwischen GDC der Anode und YSZ des Elektrolyten zugeschrieben. Während der Hochtemperatursinterung des Elektrolyten bilden sich Mischphasen mit geringerer Ionenleitfähigkeit. Des Weiteren führen unterschiedliche Diffusionskoeffizienten von Gd^{3+} und Ce^{4+} in YSZ sowie Y^{3+} und Zr^{4+} in GDC zu Kirkendall-Porosität und Ni Agglomeration in der Anode. Während des Zelltests von Ni/GDC basierten Zellen mit Bio-Synthesegas wurde eine erhöhte elektrochemische Degradation im Vergleich zu Ni/YSZ basierten Zellen beobachtet.

In der Literatur wird Mo-haltigen Werkstoffen eine erhöhte Stabilität unter C- und S-haltigen Brenngasatmosphären zugeschrieben. Zugabe der Mo-haltigen Ausgangsstoffe MoO_3, $NiMoO_4$, $Ce_{1-x}Mo_xO_{2+\delta}$ und $Ce_{1-x}Gd_{0,1}Mo_xO_{2+\delta}$ wurde im Siebdruckprozess untersucht. Aufgrund der geringen thermischen Stabilität von Mo-Verbindungen ist die Sintertemperatur in der Anoden- und Elektrolytherstellung beschränkt, wodurch die Zellleistung beeinträchtigt wird. Mo Zugabe über Gasphasendiffusion oder thermisch aktivierte Festphasendiffusion führten entweder zu keiner nennenswerten Mo Anreicherung oder zu einer ungeeigneten Mikrostruktur der Anode. Durch Verwendung eines elektrolytgestützten Konzepts konnte eine Herstellung über Infiltration einer Mo Lösung in eine Ni/GDC Anode umgesetzt werden. Diese Zelle zeigte eine verbesserte elektrochemische Leistung und erhöhte Toleranz gegenüber S-Verunreinigungen des Brenngases.

Content

1. Introduction

1.1. Energy crisis and alternative energy source

Fossil fuel is not only limited in supply but also polluting the environment through the emission of greenhouse gases such as CO_2. Nuclear fission, which is considered as an alternative energy source, faces issues of safety and radioactive waste. Therefore, the development of new types of power production systems is essential for a sustainable energy infrastructure. Biomass is a promising alternative energy source since it is renewable and carbon-neutral. Moreover, primary sources of biomass such as wood, crops, grass, and food waste are spread all over the world and are easy to store. Thus it is safe from supply-and-demand mismatch, unlike solar and wind power generation which are affected by climate conditions.

1.2. SOFC and bio-syngas application

Solid oxide fuel cells (SOFCs) are one of the most efficient energy conversion technologies from chemical energy directly to electricity via an electrochemical cell. Another advantage of SOFCs is the fuel flexibility due to the high operating temperature (650-950 °C), enabling operation on carbohydrate fuels such as natural gas, in addition to pure H_2 [1-4]. A combination of an SOFC supplied by syngas obtained from biomass gasification (bio-syngas) is strongly recommended by many authors [5-7] as a new power supplying unit. SOFC systems are well suited to produce electricity in small or intermediate scale (~ kW_{el}) power plants instead of a large one, thereby avoiding power losses during transfer. This local energy system also enables the utilization of thermal energy in a so-called combined heat and power (CHP) concept which provides even higher system efficiency of 90 % [8-10]. However, when bio-syngas is applied to Ni/YSZ, serious cell degradation is observed from impurities in the fuel such as tar [11-14] and sulfur [15-17]. These tar and sulfur impurities easily react with Ni, cover the surface, and induce particle coarsening and depletion. These changes dramatically degrade the electrochemical performance of SOFCs by reducing the active area of triple phase boundaries (TPB). Although clean bio-syngas is available through catalytic removal of tar and sulfur before supply to SOFCs, the system loses a considerable amount of energy during tar removal, and the catalysts for cleaning also shows poisoning and degradation [18]. Thus, internal reforming of the sulfur and tar in SOFCs with an alternative anode material would be more favorable than external reforming due to the higher energy conversion efficiency and simpler system design.

1.3. Aims of this work and outline

This PhD work is part of the SynSOFC project, which is a collaborative work of Forschungszentrum Jülich GmbH (JÜLICH) and the Technical University of Munich (TUM) with funding of the Deutsche Forschungsgemeinschaft (DFG). As mentioned in the previous section 1.2, the SynSOFC project suggests a new power generation system by fueling SOFCs with bio-syngas. Current SOFC anode materials are highly degraded by sulfur and tar in bio-syngas, so this project first aimed to understand the cell degradation mechanism and then to develop an alternative anode material. Figure 1.1 shows a flow chart of the SynSOFC project, including the missions of TUM and JÜLICH respectively. At first, to understand the effect of impurities, current state-of-the-art SOFCs were tested with sulfur and tar containing simulated bio-syngas. The tests were repeated with alternative anodes and the results were evaluated as a function of the degradation rate. The chemical and physical changes of cells after each test are analyzed to understand the poisoning mechanism and the effect of different anode materials. At the end of the project, 2- and 4-layer SOFC stacks were tested with real gasified bio-syngas to have more practical information.

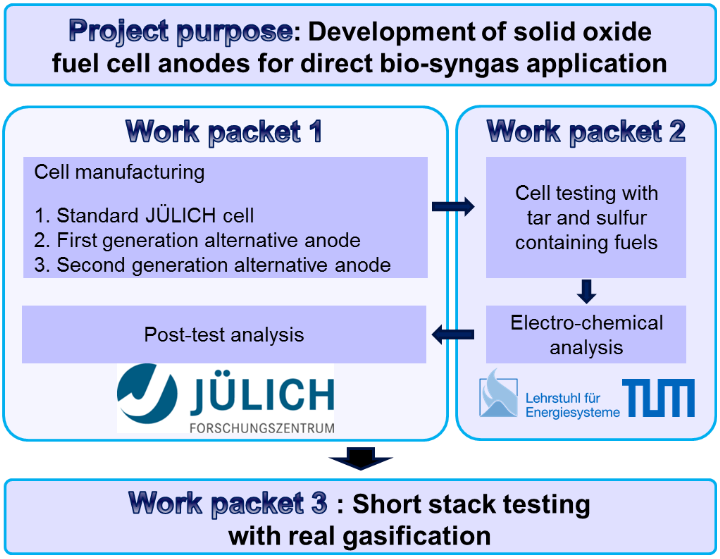

Figure 1.1: Flow chart of development process and cooperation system of between TUM and JÜLICH

2. Fundamental background

2.1. Solid oxide fuel cells

2.1.1. Working principles and history of fuel cells

Fuel cells generate electricity from chemical energy in fuels and oxygen (or other oxidizing agent) through an electrochemical reaction. For example, the typical hydrogen fuel is oxidized in the anode (Equation 2.1) and oxygen is reduced in the cathode (Equation 2.2); Equation 2.3 shows overall reaction of hydrogen and oxygen.

$$H_2 + O^{2-} \rightarrow H_2O + 2e^-, \text{ (hydrogen oxidation, anode)} \qquad \text{Equation 2.1}$$

$$\frac{1}{2}O_2 + 2e^- \rightarrow O^{2-}, \text{ (oxygen reduction, cathode)} \qquad \text{Equation 2.2}$$

$$H_2 + \frac{1}{2}O_2 \rightarrow H_2O \text{ (overall reaction)} \qquad \text{Equation 2.3}$$

This energy conversion is possible due to the special property of the electrolyte layer, which does not conduct electrons but only ionic charge carriers (oxide ions or protons). Unlike combustion, which is a direct reaction of hydrogen and oxygen, the partial reactions are spatially separated by the electrolyte in the fuel cell. These two partial reactions require ions and electrons, but as only ions can flow through the electrolyte, the electrons flow through an external circuit as electric current. Therefore, the electrolyte requires high ionic conductivity and low electronic conductivity, with oxide ion transport number (the ratio of ionic conductivity to total conductivity) greater than 0.99. The microstructure of electrolytes should be gas impermeable to avoid direct combustion.

Figure 2.1 is a schematic diagram of various types of fuel cells, including their operating temperature, fuels and oxidizing agents, and conducting ions. Most of the fuel cells are named by electrolyte materials which are the core components in fuel cells; the properties of fuel cells are mainly determined by the electrolyte they use.

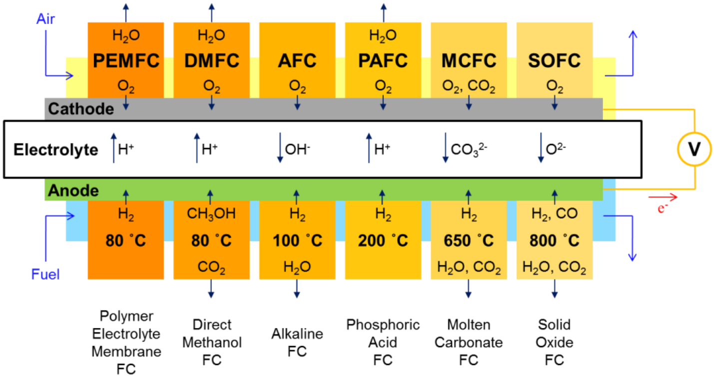

Figure 2.1: Schematic diagram of various types of fuel cells

The first hydrogen fuel cell was introduced by W. R. Grove in 1842 [19]. This first fuel cell was similar to phosphoric-acid fuel cells used today. The commercial usage of fuel cells began in the 1950s as General Electric Company collaborated with NASA for spacecraft shuttles during the human spaceflight program project Gemini. In 1966, the first fuel cell road vehicle was developed by General Motors with a polymer electrolyte membrane fuel cell. The first large stationary fuel cell system was manufactured by UTC Power for use in combination heat and power (CHP) systems for large scale buildings like universities or hospitals.

2.1.2. Properties and advantages of solid oxide fuel cells (SOFCs)

Figure 2.2 shows a schematic illustration of an SOFC structure with an oxygen ion conductor as electrolyte, as well as the reaction of fuel and oxygen. An SOFC has the structure of a porous anode and cathode that are separated by a dense electrolyte. The reactions at anode and cathode presented in Figure 2.2 represent the most common fuels (hydrogen and carbon monoxide), and oxygen as the oxidant. Since ceramic ion conductors are used as electrolyte, the system needs a high operating temperature (600 ~ 1000 °C) for sufficient ionic conductivity. This high operating temperature enables the utilization of various types of hydrocarbon fuels such as natural gas, reformed coal gas, and bio-syngas, without high cost catalysts or external reformers. Furthermore, the high operating temperature provides high energy conversion efficiency of about 60 % and provides high quality waste heat that can be utilized to further increase the system efficiency; this co-generation system efficiency of a CHP reaches up to 90 % [8-10]. SOFCs are made of only solid components, so the cell and stack have compact design, and there is no depletion or corrosion by liquid electrolyte. These stable properties of solid oxide materials provide a long-term stability compared with other fuel cells.

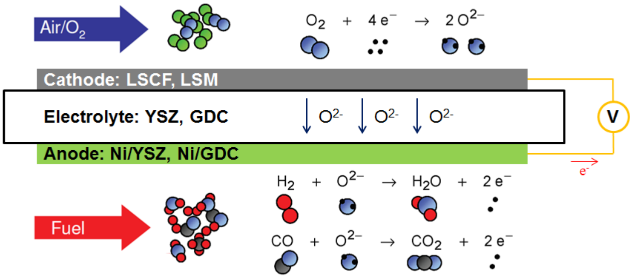

Figure 2.2: Schematic illustration of structure and working principle of SOFCs

The electromotive force (e.m.f.) or reversible (thermodynamic) voltage (E_r) of fuel cell is well described in the literature [20]. For example, if the reactants and the products are in their standard states, the ideal standard potential E^0 can be represented as

$$E^0 = -\frac{\Delta G^0}{nF} \qquad \text{Equation 2.4}$$

for the typical fuel cell reaction of hydrogen and oxygen in Equation 2.1 and Equation 2.2, where n is the number of electrons exchanged in the total reaction (2 for hydrogen and oxygen reaction), F is the Faraday constant (96485 As/mol), and $\Delta G^0{}_{298} = -286\ kJ/mol$. Therefore, at the standard condition (25 °C and 1 atm), E^0 is calculated as below.

$$E^0 = -\frac{286\ kJ/mol}{2 \times 96485\ As/mol} = 1.23\ V \qquad \text{Equation 2.5}$$

The relationship between the ideal standard potential E^0 and the ideal equilibrium potential E_r at other temperatures and pressures of reactants and products can be calculated by Nernst equation as below [21].

$$E_r = E^0 + \frac{RT}{4F} lnP_{O_2} + \frac{RT}{2F} ln\frac{P_{H_2}}{P_{H_2O}} \qquad \text{Equation 2.6}$$

where E^0 is the standard potential, R is the gas constant, T is the temperature, and P is the partial pressure of the reactants. At standard state E_r is same as E^0. The cell voltage of the actual cell in operation (E) is always lower than the reversible voltage because of ohmic losses in the electrolyte, as well as activation polarization losses and concentration polarization losses in the electrodes. The actual cell voltage of an operating cell is

$$E = E_r - (\eta_a + \eta_\Omega + \eta_c) \quad \text{Equation 2.7}$$

where η_a is the activation polarization, η_Ω is the internal resistance (ohmic losses), and η_c is the concentration polarization. Figure 2.3 shows typical voltage curves related to current density [20].

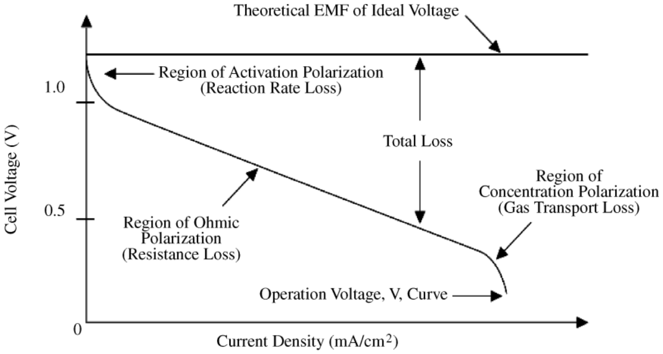

Figure 2.3: Ideal and actual performance of a fuel cell with respect to the potential current response [20]

The activation polarization depends principally on the electrochemical reaction rate. Electrode polarization results from the exchange current density at the electrodes, which is temperature activated and bias dependent. Thus, activation polarization is dominant at low current density and becomes a minor contribution to cell polarization at high current density. The electrode polarization can be reduced by microstructural changes which can provide more electrochemically active areas, such as triple phase boundaries (TPB).

The ohmic losses in the cell are primarily caused by the resistance of ionic transport in the electrolyte. Since this resistances obeys Ohm’s law, the overall ohmic over-potential can be decreased by low current density of the cell, as well as reduced thickness and low resistivity of the electrolyte material.

Concentration polarization becomes significant in the high current density region where the fuel utilization is high and the reaction rate at the electrodes are sufficiently fast to deplete fuel or oxygen in the electrochemically active regions of the electrodes. The transport of fuel or oxygen in the pores of the electrodes by gas diffusion then becomes rate-limiting. In the experiment, the concentration polarization is observed as a drastic degradation at a certain critical current density.

2.1.3. SOFC materials

2.1.3.1. Electrolyte

First of all, electrolyte materials require high ionic conductivity with negligible electronic conductivity for their basic function in SOFCs. To avoid direct combustion of fuel and oxygen, the structure should be gas-tight. During the operation, the electrolyte layer is exposed to both oxidizing and reducing atmospheres at relatively high temperature, thus the electrolyte materials need sufficient chemical and thermal stability. In addition, the electrolyte should not form secondary phases during high-temperature processing of the cell. Yttria-stabilized zirconia (YSZ) remains the state-of-the-art electrolyte material since it provides the best compromise between all the requirements mentioned above. The ion conduction mechanism of YSZ is based on an oxygen vacancy migration mechanism. The creation of oxygen vacancies by substitution of Zr^{4+} by Y^{3+} ions can be described as below with the Kröger-Vink notation.

$$\mathrm{Y_2O_3} \xrightarrow{\mathrm{ZrO_2}} 2Y'_{Zr} + V_O^{**} + 3O_O^x \qquad \text{Equation 2.8}$$

The Equation 2.8 indicates that two Y^{3+} ions on the zirconia lattice site generate one oxygen vacancy. These oxygen vacancies are mobile in the YSZ lattice and provide ionic conductivity. The most common composition of YSZ is 8 mol% yittria-doped-zirconia (8YSZ), which is cubic structure. The low content of YSZ shows an instable tetragonal phase and low conductivity due to low density of oxygen vacancy [22-25]. In the case of high doping content, YSZ also shows low ionic conductivity due to the decrease of the defects mobility by point defects [25] and increase of activation energy by interaction between oxygen vacancies [22-24]. Although the ionic conductivity of YSZ is not the highest compared with other materials (Figure 2.4), YSZ satisfies most of the mentioned requirements for an electrolyte. Various kinds of materials have been tried to improve electrolyte performance, but they have obvious disadvantages. Due to their high ionic conductivity, ceria-based materials are one of the strong candidates as an alternative SOFC electrolyte. For example, gadolinia-doped ceria (GDC) shows higher ionic conductivity of (~0.025 S cm^{-1}) than YSZ (<0.005 S cm^{-1}) at the low temperature of 600 °C. However, ceria based material become electronically conductive by the reduction of Ce^{4+} to Ce^{3+} from the temperatures above about 650 °C in reducing atmosphere [26]. Moreover, this reduction is accompanied by chemical expansion that can lead to crack formation in the electrolyte. Therefore, the application of GDC is limited to the low temperature range below 600 °C. Scandia-doped zirconia (ScSZ) also has high conductivity, but scandia is more expensive than yttria, and it has a vital weakness of phase stability by phase transition from cubic to rhombohedral at the temperature of 300–500 °C [27, 28]. The high ionic conductivity of a perovskite structure (La,Sr)(Ga,Mg)O_3 (LSGM) has been reported by Ishihara et al. [29]. The conductivity of LSGM is significantly higher than that of YSZ; it shows sufficient conductivity even at 400 °C. However, it reacts with almost all electrode materials such as zirconia and ceria, forming secondary phase of $LaSrGa_3O_7$ which considerably increase the resistance of the cell [30].

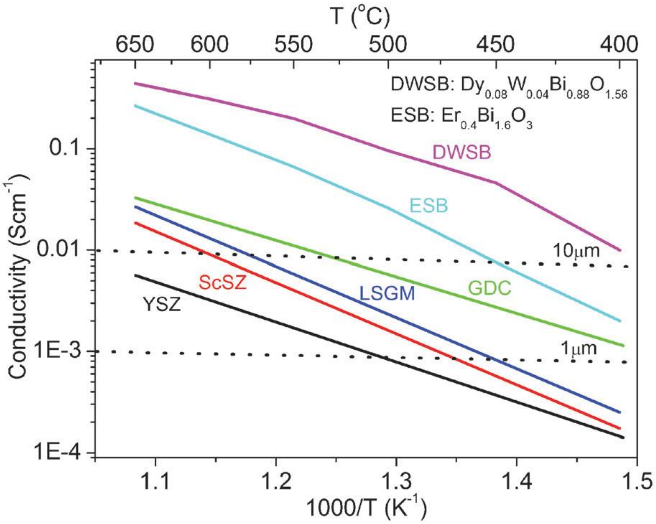

Figure 2.4: Specific ionic conductivity of various SOFC electrolyte materials [31]

2.1.3.2. Cathode

The cathode, or air electrode, reduces oxygen molecules to oxygen ions. The cathode microstructure should be porous to allow the approach of oxygen gas near to the electrolyte, and have a high internal surface area to increase the density of active sites where the electrochemical reaction takes place. After the reduction of oxygen, the ions and electrons flow through the cathode to the electrolyte and the current collector, respectively. Therefore, the cathode needs sufficient electronic and ionic conductivity. The physical properties of a cathode such as thermal expansion coefficient should be well matched with the electrolyte, and there should be negligible chemical interaction during sintering or operation (such as secondary phase formation). Because of these particular requirements, only few materials have proved to have suitable properties up to now.

Conducting perovskite oxides are typically used for SOFC cathode material. The performance of various perovskite cathodes in full cell tests is presented in Figure 2.5 [32]. Strontium-substituted lanthanum manganate (LSM) provides high p-type electronic conduction by the formation of mixed Mn^{3+}/Mn^{4+} valence states and charge carrier hopping between the Mn centers. LSM also shows an excellent electro-catalytic activity for the reduction of the oxygen molecule and adapted thermal expansion to YSZ electrolyte. However, the performance of LSM is limited to the high operating temperature region due to its low oxygen diffusion coefficient, requiring the use of composite cathodes with an ionic conductor such as YSZ to improve the electrode performance. Another common cathode material is lanthanum strontium cobalt ferrite (LSCF), which has a higher ionic conductivity than LSM [33]. However, the LSCF cathode interacts with the YSZ electrolyte during cathode sintering, forming insulating $SrZrO_3$ which highly degrades cell performance [34, 35], so an additional diffusion barrier layer of gadolinia-doped ceria (GDC) is applied between cathode and electrolyte. The cell with strontium substituted lanthanum cobaltite (LSC) cathode shows the highest performance, but is much less chemically stable than LSCF [36].

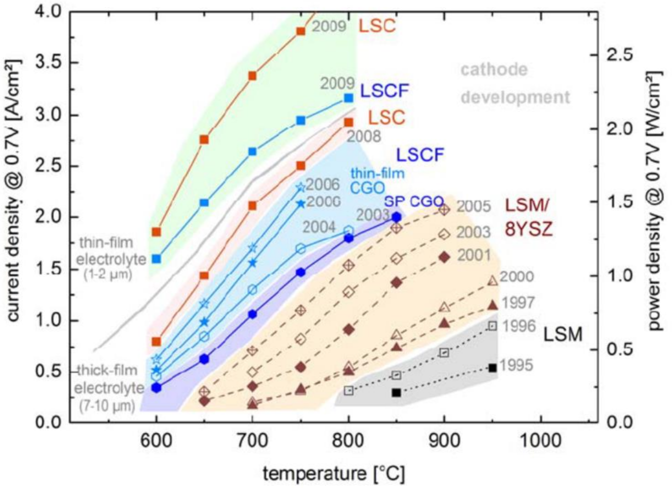

Figure 2.5: Current density as function of operating temperature for single cell tests with various cathode materials [37]

2.1.3.3. Anode

The anode, or fuel electrode, is a catalyst which oxidizes fuels such as hydrogen and carbon monoxide into water and carbon dioxide, respectively. Although the electrochemical reaction of the anode is different from that of the cathode, the physical requirements are similar. An anode requires sufficient electronic and ionic conductivity for electrochemical reactions and charge-carrier transfer. The microstructure of the anode should be porous for the diffusion of fuel near the electrolyte and a high internal surface area for a high reaction rate. The thermal expansion behavior also needs to be close to the electrolyte and interconnect materials, without chemical interactions. Additionally, the anode material should be stable in reducing environment at relatively high temperature.

Ni-based cermet anodes fulfill most of the above requirements. Since Ni is a purely electronic conductor, a composite with an ion-conducting phase is necessary to increase the density of active sites of the anode. YSZ is a good ionic conductor, thus Ni/YSZ cermet anodes are widely used. Currently, there are no competitive materials to Ni/YSZ in terms of performance and material stability; however, it still has several issues to be overcome. First, the Ni-NiO redox cycle causes a volume change in the Ni grains due to the Kirkendall effect [38], which in turn causes mechanical stress and damage to the electrolyte [39, 40]. Therefore, the cell should always be kept in reducing atmosphere once the operation is started. Another problem with the Ni/YSZ anode is the deactivation of Ni surface by carbon or sulfur deposition when the cell is used with contaminated fuels. Ni is a good catalyst for reforming hydrocarbon fuels, and it is also one of the best materials for carbon formation (catalytic cracking). There are many studies about alternative anodes to improve anode performance related to carbon deposition and sulfur poisoning; more details about alternative anodes will be discussed in section 2.4.

2.1.3.4. Interconnect materials

For the commercial application, SOFCs need to be assembled as a stack to produce the appropriate amount of power. Interconnects are the components used for connecting the cells in a stack. The interconnect requires high electronic conductivity for current collection, chemical stability in both reducing and oxidizing atmospheres, and proper mechanical strength to protect the cells in the stack from external forces. Additionally, the coefficient of thermal expansion should match that of cell components relatively well to avoid thermal stresses. Since the interconnect has complex shape, the machinability of materials is also an important factor.

For the intermediate temperature SOFC, highly oxidation-resistant metallic alloys are used as interconnects because of their simple manufacturing, low cost, and high strength compared with ceramic based interconnects. Stainless steels with a high content of chromium (Cr) are one of the typical interconnect materials. Due to the formation of a dense Cr-oxide scale on the metal surface, it shows high oxidation resistance. But the material is not fully stable over application periods of > 40,000 h on the air side. At high temperatures and high oxygen partial pressures, significant Cr evaporation takes place as CrO_3 (which is more severe when residual moisture is present in the air). The gaseous Cr-species react with the cathode materials, resulting in a strong increase of the polarization resistance of the cathode [41-43]. Therefore, perovskite and/or spinel materials are applied as evaporation barrier layers to reduce Cr evaporation [44-46].

2.1.4. SOFC design

There are three common cell designs: electrolyte-supported cells (ESC), anode-supported cells (ASC), and metal-supported cell (MSC). Figure 2.6 shows schematic diagrams of each cell type and its characteristics. The ESCs are the first generation of SOFCs which were manufactured using electrolyte of several hundreds of micrometers in thickness. This thick and pre-sintered electrolyte provides mechanical stability and facilitates further electrodes deposition process. However, it also brings high ohmic polarization, so the ESCs need high operating temperature of 800 ~ 1000 °C. Although high operating temperature reduces activation polarization of ESCs, the thick electrolyte reduces the cell performance by high ohmic polarization. Therefore, in an attempt to reduce the electrolyte thickness to 5~20µm, a second generation of cells (ASCs) has been developed. The mechanical stability of ASCs is provided through a porous, thick Ni/YSZ support, enabling the fabrication of thin electrolytes (typically 10, but can be as thin as 1-2 micrometers). This thin electrolyte enables the reduction of the operating temperature of ASCs to 600 ~ 800 °C with higher performance than ESCs due to the significantly lowered ohmic polarization of electrolyte. Currently, ASCs seems most suitable for stationary stack systems, according to operating temperature, performance, and stability. However, ASCs have inevitable problems such as brittleness (ESCs are even more brittle) and low thermal conductivity of zirconia or ceria based materials which are typical electrolyte and anode materials. This becomes a big issue for the application as an auxiliary power unit (APU), which requires short start up time, high mechanical durability and thermal cycling capability. Metal-supported cells (MSCs) are suggested to overcome these problems of ceramic-supported type cells like ESCs and ASCs. MSCs use porous metal support, which has better mechanical properties and are more resistant against thermal shock. However, it has complex and expensive processing to avoid oxidation of the support, and their practical performance is still lower than ASCs

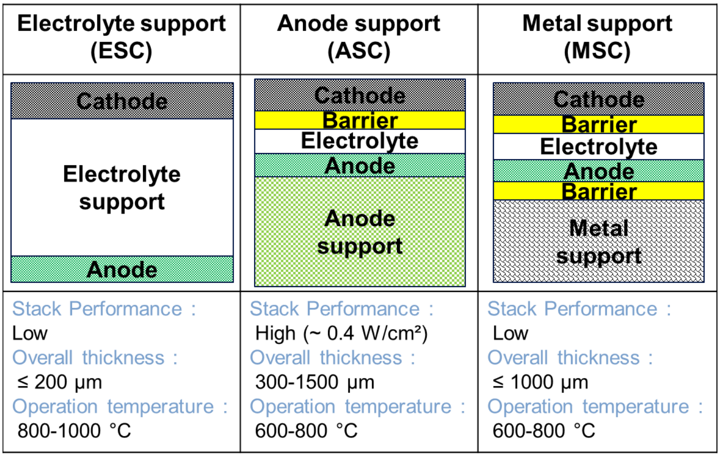

Electrolyte support (ESC)	Anode support (ASC)	Metal support (MSC)
Cathode Electrolyte support Anode	Cathode Barrier Electrolyte Anode Anode support	Cathode Barrier Electrolyte Anode Barrier Metal support
Stack Performance : Low Overall thickness : ≤ 200 μm Operation temperature : 800-1000 °C	Stack Performance : High (~ 0.4 W/cm²) Overall thickness : 300-1500 μm Operation temperature : 600-800 °C	Stack Performance : Low Overall thickness : ≤ 1000 μm Operation temperature : 600-800 °C

Figure 2.6: Three different types of SOFC and their properties

2.2. Bio-syngas

2.2.1. Biomass gasification

Biomass gasification indicates a synthesized gas (syngas) producing process, involving the burning of biomass under restricted air supply. During the gasification, biomass goes through three steps: drying, pyrolysis, and gasification (partial oxidation) [47]. Figure 2.7 shows the most relevant types of gasifiers: fixed bed (up and down draft), fluidized bed, and entrained flow gasifiers. The main differences among these gasifiers are how the biomass, oxidizer, and fuel gas are moved in the reactor.

Fixed bed gasifiers are the oldest and simplest method. In a fixed bed, the feedstock moves down in a vertical container and the chemical reactions happen in the bottom part. Fixed bed gasifiers are relatively inexpensive due to their simple structure. They show high overall carbon conversion, but have limited scalability [48]. Fixed bed gasifiers are classified as four different types according to oxidant and gas flows: updraft, downdraft, cross-draft, and open-core.

In fluidized bed gasifiers, a large amount of feedstock is kept as fluid-like state by the oxidizer agent injection from the bed underneath. Fluidized bed system has several advantages compared to the conventional fixed bed system, for instance high feedstock capacity and wide feedstock basis. However, the temperature of the fluidized bed is fairly low compared to that of the oxidation zone in fixed bed gasifiers. The low reactor temperature also affects tar cracking negatively. There are two main ways of fluidizing methods of bubbling (BFB) and circulating (CFB). Due to the faster velocity of CFB, the carbon conversion of CFB is generally better than BFB.

The entrained flow gasifiers use very fine particles as feedstock, either dry powder or suspended in water. The gasification is very fast due to the high chamber temperature of over 1400 °C, usually with oxygen or with a mixture of oxygen and steam. Entrained flow gasification is a suitable method for hard coals, but in the case of biomass utilization, it has not drawn yet much attention due to the complex feedstock preparation. Entrained flow gasification is suitable for large scale conversion and the product gas quality is very high [49].

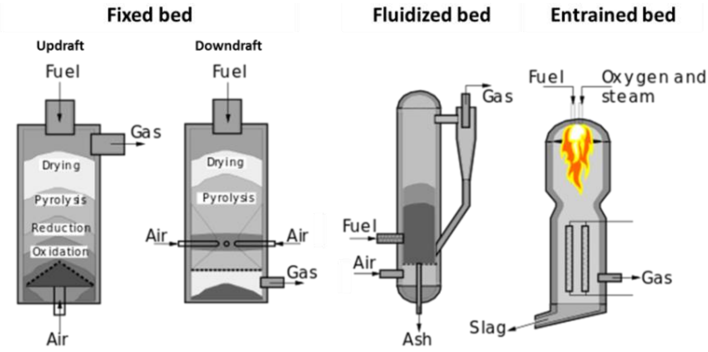

Figure 2.7: Schematic diagrams of type of gasifiers

2.2.2. Gas composition of bio-syngas

As the result of gasification, a mixture of bio-syngas is achieved including carbon monoxide, carbon dioxide, hydrogen, methane, water vapor, nitrogen, and various kinds of minor contaminant like tar, sulfur, and chlorine species. The gas compositions are dependent on biomass feedstock, gasification method, and oxidant types.

The list of bio-syngas compositions using different feedstock are shown in Table 2.1. The result shows similar composition of each product regardless of feedstock. The main combustible species of wood are cellulose, hemicelluloses, and lignin, which are made of carbon, hydrogen, and oxygen. Most kinds of biomass have a relatively constant carbon-hydrogen-oxygen ratio [50], thus the types of biomass are less important for the gas composition.

Table 2.1 Influence of different feedstock in chemical composition of bio-syngas, fixed bed (downdraft) gasifier [51]

Feedstock	Gas produced (mol/kg)				
	H_2	CO	CO_2	CH_4	C_nH_m
Rice husk	0.00236	0.00651	0.00717	0.00209	0.000932
Nut shell	0.00485	0.00788	0.00477	0.00293	0.000869
Pine	0.00529	0.00722	0.00505	0.00272	0.000947
Eucalyptus	0.00275	0.00712	0.0038	0.00316	0.000726

Table 2.2 shows the chemical composition of bio-syngas produced by different types of gasifiers. The results show a higher CO content with a fixed bed than a fluidized bed. The temperature, pressure, and residence time, which are also critical for gas composition, are also related to the gasifier type.

Table 2.2 Influence of reactor type in chemical composition of bio-syngas, air-blown [52]

Gas	Fixed bed		Bubbling fluidized bed
	Downdraft	Updraft	
H_2 (vol. %)	17	11	9
CO (vol. %)	21	24	14
CO_2 (vol. %)	13	9	20
CH_4 (vol. %)	1	3	7
N_2 (vol. %)	48	53	50

Table 2.3 shows the influence of the oxidant on bio-syngas compositions. Generally, steam and pure oxygen produce more hydrogen and carbon monoxide than air [53]. Although CO_2 and N_2 are not desired gases, air is used in many cases because it does not produce additional cost.

Table 2.3 Influence of oxidant type in chemical composition of bio-syngas with wood feedstock [53]

Oxidizing agent	Composition (vol. %, dry base)				
	H_2	CO	CO_2	CH_4	N_2
Air (downdraft)	17	21	13	1	48
Air (BFB)	9	14	20	7	50
Air (CFB)	14.1	18.7	14.7	3.5	47.7
O_2 (downdraft)	32	48	15	2	3
Steam (CFB)	34.2	27.2	22.7	11.1	4.8
Steam (BFB)	52	23	18	7	Not defined

2.2.3. Impurities in bio-syngas

During the gasification, the hydrocarbon shows secondary reaction with gasifying agents and generally exists in the producer gas stream. The typical tar species in bio-syngas are benzene, toluene, xylene, phenol, and naphthalene. The tar quantities are mostly related with the gasifier and oxidant types; downdraft fixed bed shows best tar cracking ability [52] and air as oxidant produces less tar than oxygen and steam [53]. In the case of downdraft fixed bed gasifiers, the total tar content shows from 0.01 to 6 g/Nm^3 [54]. The tar generally condenses at the low-temperature area like plugging and fouling of pipes, tubes, and other equipment. On the other hand, above 400 °C, the tars dehydrate and form solid coke.

In woody biomass, various metal and inorganic elements are also included. These elements are mostly emitted as ash or slag in gasifier, but sulfur is easily turned to dihydrogen sulfide (H_2S) or sulfur dioxide (SO_2) and included in syngas. Since the content of sulfur species are normally less than 0.1 %, which is a much lower percentage compared to coal, the sulfur content in bio-syngas is negligible for internal combustion engine and gas turbine applications [54]. However, in the chemical synthesis or fuel cell application, the catalyst materials are highly sensitive to sulfur [15, 55, 56]. The sulfur tends to chemically adsorb on the catalyst surface and deactivate the catalyst.

2.3. Degradation of SOFC

2.3.1. General degradation phenomena of SOFCs

In SOFCs, general degradation behavior can be classified as three types: intrinsic, extrinsic, and cyclic degradation [57]. The cyclic degradation mechanisms are mostly related to thermal stress during on-off cycles, which is not too critical in stationary applications. Cracking of the electrolyte by thermal stress or redox instability (anode expansion by Ni oxidation) are typical cycling degradation behaviors.

The intrinsic degradation can be divided again into physical and chemical degradation. The physical degradation includes electrolyte fracturing [58] and electrode particle coarsening [59]. Cracks in the electrolyte allow gas cross-over, which decreases cell efficiency and can lead to fuel burning and larger electrode particles provide less catalytically active points. The causes of these physical changes are mainly thermally activated processes. One of the well-known chemical degradations in common SOFC configuration is strontium (Sr) segregation of the cathode [60] and reaction with the electrolyte [34, 35]:

the cathode is deactivated by segregation and insulating $SrZrO_3$ phase formed at the interface of cathode and electrolyte, respectively. Material selection is thus crucial for cell degradation.

The extrinsic degradations are caused by either metallic interconnect in stack or impurities in fuel gas. From the interconnect material, Cr poisoning is most critical especially with regards to the cathode [41, 61]. Gaseous Cr-species are easily formed from the metallic interconnect in oxidizing atmosphere, and it reacts with cathode materials and forms non-conducting phase such as $SrCrO_4$ [62, 63]. On the other hand, anode sulfur poisoning and carbon deposition is a crucial topic for syngas or natural gas utilization. The details of anode poisoning behavior according to the fuel impurities will be described in following chapters.

2.3.2. Carbon related degradation

One advantage of SOFC is the possibility of direct hydrocarbon fuel utilization through internal reforming reactions. For example, carbon monoxide, methane, and other hydrocarbons are reformed by water-gas-shift reaction (Equation 2.9) and steam reforming (Equation 2.10 and Equation 2.11) if the fuel includes enough steam.

$$\mathrm{CO + H_2O \rightarrow CO_2 + H_2}$$ Equation 2.9

$$\mathrm{CH_4 + H_2O \rightarrow CO + 3H_2}$$ Equation 2.10

$$\mathrm{C_nH_m + nH_2O \rightarrow nCO + \left(n + \frac{m}{2}\right) H_2}$$ Equation 2.11

However, when the steam-to-carbon ratio or the operating temperature is too low, solid carbon is formed via the Boudouard reaction (Equation 2.12) or decomposition reactions (Equation 2.13, Equation 2.14).

$$\mathrm{2CO \rightarrow C + CO_2}$$ Equation 2.12

$$\mathrm{CH_4 \rightarrow C + 2H_2}$$ Equation 2.13

$$\mathrm{C_nH_m \rightarrow nC + \frac{\mathit{m}}{2} H_2}$$ Equation 2.14

Ni, currently the most common anode material, is a good catalyst for reforming fuel species, but it is also well-known as a highly active catalyst for carbon formation; thus a Ni surface can easily be covered by carbon or nickel carbide under low steam conditions [64-66]. Figure 2.8 shows TEM images of Ni/YSZ anode after cell operation with hydrogen (a and b), syngas (CH_4 - 23.64 %, CO - 7.60 %, CO_2 - 14.27 %,

H_2 - 49.48 % and H_2O - 5.00 %) for 15 min (c) and 2 h (d) [64]. The images show a continuous carbon film formation on Ni surface after syngas operation. This surface change significantly deactivates Ni catalyst for fuel utilization. Moreover, under extreme condition, carbon fibers are easily grown in anode and the anode structures are changed by Ni coarsening or depletion [67-70]. A high steam-to-carbon ratio can reduce these poisoning behaviors, but the high steam ratio deactivates fuel reforming activities due to diluted fuel concentration [71].

Additionally, tar species (benzene, toluene, phenol, and naphthalene) cause more aggressive carbon deposition [11-13, 72] and the performance degradation [73-75] even under high enough steam-to-carbon ratio to avoid solid carbon formation. The mechanism of tar reforming and cell degradation is not fully understood yet. One possible reason is the chemisorption of tar on the anode surface, reducing the surface area due to the slow reforming reaction.

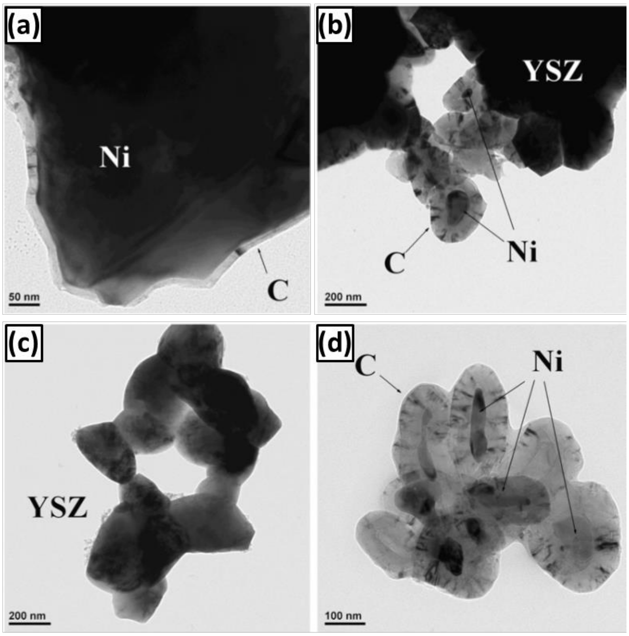

Figure 2.8: Transmission electron microscope result of the Ni/YSZ anode operated with syngas for 15 min (a) and 2 h (b~c) [64]

2.3.3. Sulfur poisoning

In the case of Ni/YSZ anode, sulfur poisoning can be divided into two different types; nickel sulfide (Ni_xS_y) formation and surface sulfur adsorption. Figure 2.9 shows calculated Ni-H-S-O phase diagrams at (a) 800 and (b) 1000 °C related with P_{O_2} (x-axis) and P_{H_2S} (y-axis) [15]. As shown in the diagram, in the case of typical anode side atmosphere with low P_{O_2}, Ni does not chemically react with H_2S up to the P_{H_2S} level of about 10^{-3} atm (1000 ppm). This percentage level of H_2S is not typical in real syngas or natural gas, which include up to several hundred ppm of H_2S [76]. Therefore, it is rarely found in literature that the Ni_xS_y formation from in-situ Raman spectroscopy result at low temperature of 440 ℃ with 100 ppm H_2S test [16] or at 800 ℃ with 2000 ppm H_2S test [77]. Ni can be transformed to nickel-sulfide like Ni_3S_2 which has a much lower conductivity than the Ni metal. Moreover, in general SOFCs working temperature (700 - 1000 °C), Ni_3S_2 is in liquid state, thus the cell structure easily destroyed by melting or evaporation.

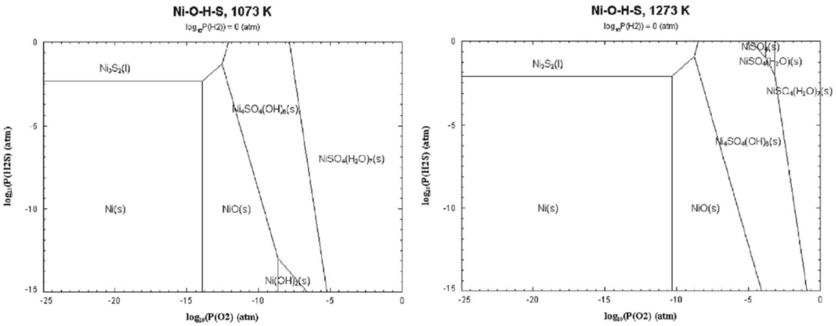

Figure 2.9: Ni–O–H–S diagrams in thermodynamic equilibrium at (a) 800 and (b) 1000 °C [15]

If the P_{H_2S} is not high enough to react with Ni, it can be reformed by direct oxidation without poisoning behavior as below

$$H_2S + 3O^{2-} \rightarrow H_2O + SO_2 + 6e^- \qquad \text{Equation 2.15}$$

Otherwise, H_2S can be decomposed first by electrochemical oxidation or thermal decomposition as below

$$H_2S + O^{2-} \rightarrow H_2O + \frac{1}{2}S_2 + 2e^- \qquad \text{Equation 2.16}$$

$$H_2S \rightarrow H_2 + \frac{1}{2}S_2 \qquad \text{Equation 2.17}$$

The sulfur formed by reactions of Equation 2.16 and Equation 2.17 can be electrochemically oxidized by the following reaction.

$$\frac{1}{2}S_2 + 2O^{2-} \rightarrow SO_2 + 4e^- \qquad \text{Equation 2.18}$$

If this series of reactions takes place during cell operation, the anode performance should be kept at the initial state. However, in the practical cases, a few ppm of sulfur content in the fuel gas is enough for poisoning. Many experimental and computational works have tried to define the mechanism of sulfur poisoning by surface adsorption, but it is still not completely clear. A computational study provides the various states of sulfur chemisorption model and the range of sulfur content to be caused the chemisorption on Ni surface. The result shows extremely sensitive behavior of Ni to sulfur, for example, only 0.1 ppm of H_2S in H_2 is enough to cover Ni surface at 800 ℃ and below [78]. Since the sulfur covers the surface of Ni, the catalytically active area at the TPBs is decreased and Ni re-oxidation can be caused by blocking of oxygen ion transfer as shown in Figure 2.10 [15].

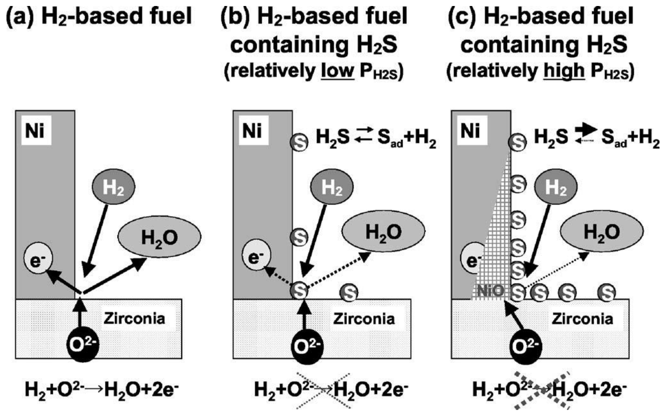

Figure 2.10: Sulfur poisoning mechanisms: (a) H_2-based fuel containing no H_2S, (b) H_2-based fuel with relatively low P_{H_2S}, and (c) H_2-based fuel with relatively high P_{H_2S} [15]

2.4. Alternative anode materials

A new anode component should have high catalytic activity for impurities or hydrocarbons in fuel (CH_4, C_nH_m, tar, H_2S, and etc.). At the same time, the anode should also fulfill the general requirements of anode materials such as chemical and electrochemical stability, electrical conductivity, and compatibility with the other components. Many studies have been carried out to find a material which corresponds to the above mentioned requirements. In this section, previous results are briefly summarized with a particular focus on their electrochemical behavior.

2.4.1. Ni-YSZ with incorporation of other materials

Because of the excellent catalytic performance of Ni-YSZ anodes with clean fuel condition, attempts have been made to modify Ni-YSZ surfaces via incorporation of various materials in an effort of develop a sulfur tolerant anode. For example, Sasaki et al. tried impregnation or infiltration by CeO_2, Y_2O_3, La_2O_3, MgO, Nb_2O_5, Sc_2O_3, ZrO_2, TiO_2, Ru, CaO, Co and Al_2O_3 in to the Ni/YSZ anode [15]. The result is presented in Figure 2.11. Although impregnation of CeO_2, Y_2O_3 or La_2O_3 significantly reduces the voltage drop by H_2S, it still displays the typical poisoning behavior even under ppm-level of H_2S concentration. Other studies of impregnation or infiltration with ceria-based conducting ceramic materials [79, 80] or single elements (W, Sn, or Sb) [81, 82] cannot avoid the rapid initial degradation. In a few cases, the cell shows less voltage drop and better stability, but the improvement is not only an effect of the materials, but also tailored microstructure made by impregnation and infiltration techniques, which are difficult and costly.

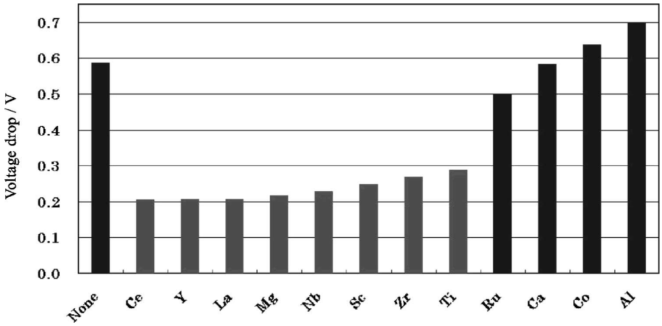

Figure 2.11: Cell voltage drop with various additives impregnated in porous anode layers at 200 mA/cm² 800 °C, H_2S conc. = 20 ppm, H_2/CO = 100:0, electrolyte/ScSZ, anode/Ni–YSZ + additives [15]

2.4.2. Cermet anode

Ni with an alternative conducting ceramic anode can be used instead of the Ni/YSZ anode to improve sulfur tolerance. Since carbon deposition takes place mainly on the Ni surface, Ni modification or alternation seems essential to prevent carbon deposition. Doped ceria electrolytes are good candidates for SOFC components because of their high ionic conductivity and low activation energy and stability. In the case of gadolinia doped ceria (GDC), the ionic conductivity is higher than YSZ and it also has electronic conductivity in reducing atmosphere through the reduction of cerium ions from the Ce^{4+} state to the Ce^{3+} state at high temperatures [83, 84]. Several previous works reported a higher sulfur tolerance of Ni/GDC anode than Ni/YSZ anode. For example, tests of button cell performances compared with 5-700 ppm H_2S in H_2 at 800 °C for 2 h show the voltage of the button cells with Ni/YSZ anode and Ni/GDC anode decreased from 0.61 V to 0.34 V and from 0.78 V to 0.72 V, respectively [85]. This can be explained by the mixed ionic-electronic conductivity of GDC. In another study, with 2 ppm H_2S added to the fuel at 850 °C, the single cell stack voltages decreased with Ni/8YSZ and Ni/10GDC anodes to 86.5% and 98.7% of their initial voltages, respectively [76]. The cell with a Ni/10GDC anode had a one-stage poisoning with a relatively small power drop, whereas the Ni/8YSZ anode cell had two poisoning stages and a second slower degradation in the following 15 h (see Figure 2.12). After removal of the H_2S atmosphere, the Ni/GDC anode regenerated its performance to almost to 100 % of the initial performance, but Ni/YSZ recovered 1 % less than the initial voltage.

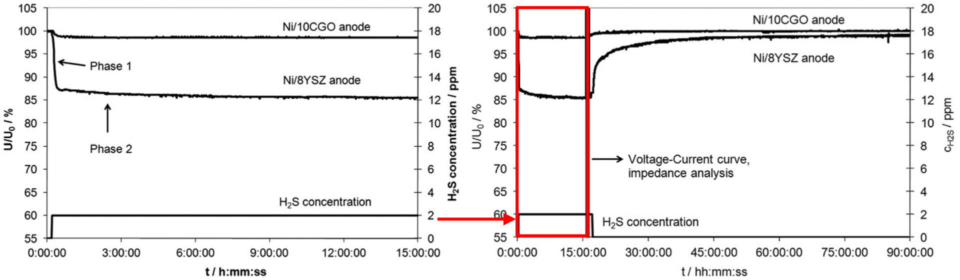

Figure 2.12: Comparison of the ratios of the contaminated stack voltages to initial voltages with respect to time with Ni/8YSZ and Ni/10CGO anodes during and after 2 ppm H_2S contamination at 850 °C [76]

Similarly, the Ni can also be replaced by other metals that have better catalytic activity to carbon and sulfur species. For example, Cu and Ag have much less affinity for sulfur adsorption because of the more positive free energy change for sulfur adsorption than nickel [86]. For example, it is reported that Cu-ceria-

YSZ cermet showed a stable power output until the pH_2S/pH_2 was increased up to 450 ppm [87]. However, both Cu and Ag have low melting points, which makes manufacturing difficult and limit operation temperature. When hydrocarbon fuels are applied to Ni-based cermet anodes, carbon is formed on the Ni surface rapidly by electron interaction of Ni 3d and C 2p orbitals. Thus, coking resistivity can be enhanced by adjusting the atomic orbital and electronic structure. There are several studies of Ni alloy with transition metals, such as Cu, Co, Mn, or Fe [88, 89]. Although some cases show improvement in coking resistivity, most of the cases show limitation as well. The case of Cu incorporation can be improved in electrochemical property, but it again has low thermal stability. Fe and Co show good overall performances; however, apparent degradation of the fuel cells are still observed in long-term operation [65, 90].

In the case of Ni-molybdenum (Mo) alloy, stable cell operations are reported for wet or dry methane [91, 92] and methane with H_2S fuels [93]. It is related to catalytic activity change from pure Mo to Ni-Mo bimetallic state. The clean Mo (110) plane surface is not chemically active for hydro-desulfurization; similar to Ni, sulfur chemically adsorbs on Mo surface. The reactivity of Mo with sulfur is increased by bimetallic bonding with other transition metals [94, 95]. Figure 2.13 shows Mo 3d XPS spectra acquired after dosing S_2 to clean and covered (~ 1.5 monolayers of Ag, Zn, Cu, and Ni) Mo (110) surfaces. The Mo 3d peak at ~ 228 eV corresponds to metallic Mo, while the peak at ~ 229.2 eV denotes the formation of molybdenum sulfides (MoS_y) in these systems. In the case Ni-Mo alloy, the MoS_y peak intensity was most strong. In general, a good correlation is observed between MoS_y formation and desulfurization. The presence of Ni leads a significant enhancement in the Mo-S interactions and a large desulfurization activity [96].

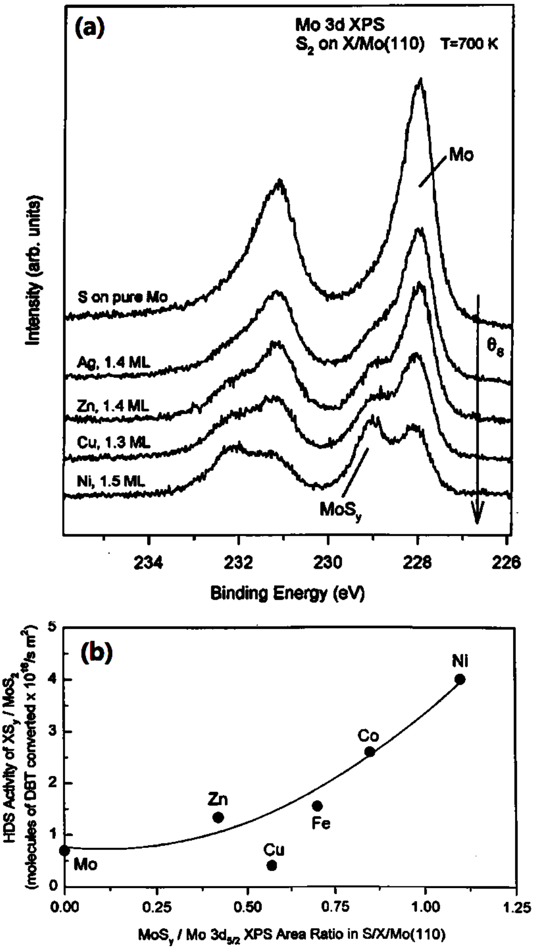

Figure 2.13: Mo 3d core-level photoemission spectra acquired after dosing S_2 to Mo (110) and X (X: Ag, Zn, Cu, Fe, Co, or Ni)/Mo (110) surfaces [70, 71] (a), and XSy/MoS_2 catalysts activity for the hydro-desulfurization (HDS) of dibenzothiophene (DBT) versus amount of MoS_y formed in each S_2/X/Mo (110) system [72] (b)

2.4.3. Mixed ionic and electronic conductors (MIEC)

Nickel-free metal oxide conductors have been studied as potential SOFC anode materials. For example, $La_{0.35}Sr_{0.65}TiO_3$–$Ce_{1-y}La_yO_2$ composite [97], $La_{0.8}Sr_{0.2}Cr_{0.8}Mn_{0.2}O_3$ (LSCM) [98] and $Sr_2MgMoO_{6-\delta}$ (SMMO) [99] show better tolerance than Ni-YSZ against low concentrations of sulfur. In some case, electrochemical performance increased upon exposure to high concentrations of H_2S at high temperature. $La_{0.35}Sr_{0.65}TiO_3$–YSZ composite anodes and $La_{0.7}Sr_{0.3}VO_3$ anodes display lower interfacial resistance under percentage level of H_2S balanced by H_2 than in pure H_2 [100, 101] and $Gd_2Ti_{1.4}Mo_{0.6}O_7$ displays a maximum power density of 340 mW/cm^2 in a fuel mixture of H_2S - 10%, H_2 - 90 %, while $P_{\max}$ in pure H_2 is only 225 mA/cm^2 [102]. The reason for this enhancement is not clear. One possibility is the formation of conducting sulfides upon exposure to sulfide-containing gas.

The conductive metal oxide anodes have potential to solve anode poisoning problem due to their stability against impurities. However, most studies are carried out under very limited conditions and their general performances are much worse than Ni/YSZ. In addition, it is difficult to fabricate anode supported cells with ceramic anodes and YSZ electrolyte, because these oxide anodes have limited physical, chemical and/or thermal compatibility with YSZ.

3. Experimental

3.1. Cell manufacturing

3.1.1. Standard cell

3.1.1.1. Single-cell manufacturing*

Two different types of anode-supported SOFCs are used in this work, in-house manufactured cells (IIIb) and commercially purchased cells (CeramTec cell, Germany). The IIIb cells were manufactured by tape casting of the support and subsequent screen printing of all functional layers as described in Figure 3.1. The anode support was prepared by tape casting using NiO (Mallinckrodt Baker Inc., USA) and $Y_{0.148}Zr_{0.852}O_{1.926}$ (8YSZ, Imerys, France) slurry with a weight ratio of 44:56. In order to achieve finer microstructure, anode layer was applied by screen printing with same Ni(O) and different 8YSZ (Tosoh, Japan). Dense 8YSZ electrolyte was also processed by screen printing, then the half-cell (support-anode-electrolyte) was sintered at 1400 °C for 5 h. Subsequently, 20 % gadolinia-doped ceria (20GDC, Treibacher, Austria) was applied as a Sr-diffusion barrier layer between electrolyte and cathode by screen printing and sintering at 1300 °C for 3 h. Finally, a $La_{0.58}Sr_{0.4}Co_{0.2}Fe_{0.8}O_{3-\delta}$ (LSCF, synthesized in-house) cathode was applied by screen printing, and the cells were sintered at a temperature of 1080 °C for 3 h. The CeramTec cells were manufactured with almost the same processes and materials as IIIb cells (based on a JÜLICH license), except that the support was $Ni/Y_{0.058}Zr_{0.942}O_{1.971}$ (3YSZ). CeramTec cells have been used to show that the test could be conducted with commercially available cell types. Previous investigations using JÜLICH and CeramTec cells for SOFC stack testing in JÜLICH have shown a nicely comparable performance of both cell types. Both, IIIb and CeramTec cells are manufactured with 100×100 mm^2 support dimension and 90×90 mm^2 active cathode area.

---

* This part (3.1.1.1) has been published in the journal "International Journal of Hydrogen Energy" Volume 43, Issue 45, 8 November 2018

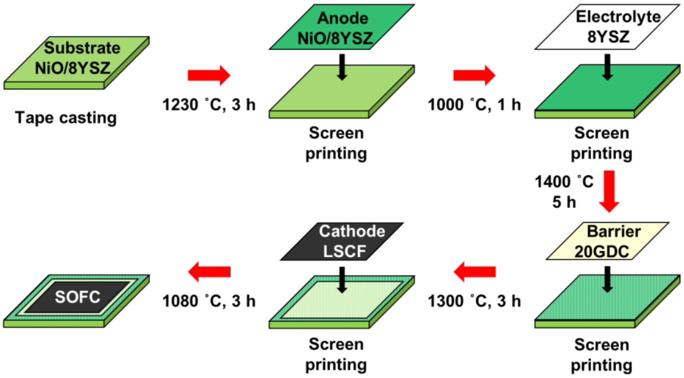

Figure 3.1: Manufacturing process of JÜLICH standard anode-supported cell

3.1.1.2. Stack manufacturing

A JÜLICH standard 4-layer stack was used in this study [103]. The commercially purchased CeramTec cells were used in the stack, as described in 3.1.1.1. All interconnects, cell frames, top and bottom plates were based on Crofer 22 APU [104]. A $MnCo_{1.9}Fe_{0.1}O_4$ (MCF) coating was applied on the interconnect surfaces facing the cathode side by atmospheric plasma spraying (APS) as a Cr-poisoning protection layer [46, 105]. For the contact between cell and interconnect, Ni mesh was used on the anode side, and a $LaMn_{0.45}Co_{0.35}Cu_{0.2}O_{3-\delta}$ (LCC10) coating was applied for the cathode by screen printing directly on the cell. Type 87 ZYBF-2 glass sealant was used for stack assembly [106] and the entire stack was held at 850 °C for 100 h to ensure glass crystallization and gas-tightness. The designation of cell and stack components is shown in Figure 3.2 as a schematic diagram with a direction of fuel gas flow.

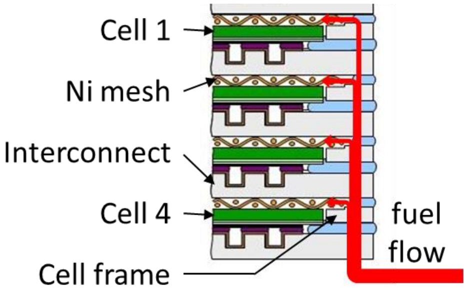

Figure 3.2: Schematic diagram of stack structure with a direction of fuel gas flow

3.1.2. Cells with a Ni/GDC anode

3.1.2.1. Study of the YSZ-GDC interaction

Two different compositions of powder mixtures were prepared: NiO:YSZ:GDC=1:1:1 and YSZ:GDC=1:1 in weight ratios. Each powder was mixed in a polyethylene bottle with zirconia balls (∅: 3mm:10 mm=1:1, total powder to ball ratio was 1:20) and ethanol by a tumbling mixer for 24 h. To evaporate the ethanol after mixing, the mixture was dried in an oven at 70 ℃ for 8 h. The powder mixtures were then pressed by hand press to button shape pellets and sintered at temperatures of 1000, 1100, 1200, 1300, and 1400 ℃ for 5 h. The reduced samples were then prepared by heat treatment at 900 ℃ for 5 h in 2.9 % H_2/Ar atmosphere.

3.1.2.2. Cell manufacturing

The Ni/GDC anode cell was manufactured with the same process of standard Ni/YSZ anode cells except for anode paste modification. The same NiO powder for the Ni/YSZ anode was used, and the YSZ was replaced by 20GDC, which is the same material used for cathodic barrier layer paste. The anode thickness and composition were optimized by using a different number of screen printing steps and different Ni to 20GDC ratios in the paste. For the cell development and performance test, in-house manufactured Ni/8YSZ supports were used with a size of 50×50 mm^2. Also, the larger size of 100×100 mm^2 cells for long-term poisoning tests and stack application were manufactured using commercially purchased pre-sintered Ni/3YSZ support from CeramTec.

3.1.3. Cells with Mo incorporation into the anode

3.1.3.1. The conventional screen printing process

$Ce_{1-x-y}Mo_xGd_yO_{2+\delta}$ (CMGO) as Mo precursor was used for anode screen printing paste. The CMGO was synthesized in-house by the conventional solid-state reaction method with MoO_3 (Sigma-Aldrich, USA), CeO_2 (Alfa Aesar, USA), and 20GDC (Treibacher, Austria). The CMGO was then prepared as a powder by the ball milling process with ethanol solvent and zirconia balls. The powder was mixed with a liquid binder (terpineol) (Sigma-Aldrich, USA) and dispersing additive (NUOSPERSE FX 9086) (Elementis, UK) by a tumbling mixer with zirconia balls (∅: 3mm:10 mm=1:1, total powder to ball ratio was 1:20) for 24 h.

The pre-suspensions were finally mixed with NiO pre-suspension and ethyl cellulose by a Thinky mixer at 1400 rpm during 2 min with the ratio of 50 to 50 wt%. The anode pastes were printed on the standard Ni/YSZ support and the cell manufacturing process was followed which is already described in section 3.1.1.1.

3.1.3.2. Mo gas infiltration

The process had two different variations: MoO_3 gas infiltration after half-cell sintering (Figure 3.3a) or during half-cell sintering (Figure 3.3b). In the case of MoO_3 infiltration into the sintered half-cell, the Ni/YSZ support—Ni/GDC anode and YSZ electrolyte construction of the half-cell—was used. To keep the electrolyte away from MoO_3 gas, a half-cell was placed like a crucible cover plate with the electrolyte side up and the MoO_3 powder was placed in the crucible. A heat treatment temperature of 1000 °C was chosen, which is higher than the MoO_3 evaporation temperature but as low as possible to prevent cell structure deformation. In contrast, for the experiment of Mo infiltration during half-cell sintering, the green state half-cell was used. The cell was placed in a crucible together with MoO_3 powder and sintered at a temperature of 1400 °C for 5 h to achieve a dense electrolyte structure. To adjust the amount of MoO_3 infiltration, MoO_3 powder weight was varied from 0.1 to 0.2 and 0.5 g in the crucible.

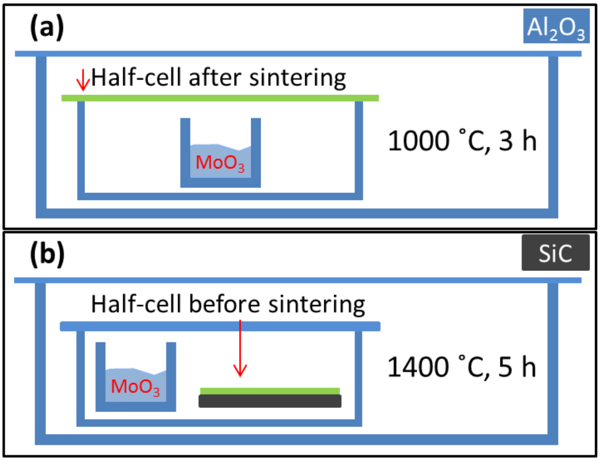

Figure 3.3: Schematic diagram of the MoO_3 gas infiltration experiment setup

3.1.3.3. Mo thermal diffusion

First, the Ni/GDC anode was printed on the Ni/YSZ support and sintered without an electrolyte at 1400 °C for 5 h. Then, MoO_3 and $NiMoO_4$ were prepared as the sub-micron scale ethanol-based suspension by conventional ball milling with zirconia balls (∅: 3mm:10 mm=1:1, total powder to ball ratio was 1:20) for 24 hours. Two different Mo suspensions were dropped on the Ni/GDC anode surface and dried in room-temperature then heat-treated with three different programs of 600 °C for 10 h, 800 °C for 5 h, and 1000 °C for 5 h for Mo thermal diffusion into the anode layer. After the heat treatment, the residual unstable material on the anode surface was removed by blowing with air.

3.1.3.4. ESC cell to reduce anode sintering temperature

A dense electrolyte support of $Zr_{0.887}Sc_{0.113}O_{1.943}$ (6ScSZ) (Kerafol Keramische Folien GmbH, Germany) was used for ESC cell manufacturing. At first, the 20GDC Sr-diffusion barrier layer was applied to the electrolyte by screen printing and sintered at 1300 °C for 3 h, which is the highest temperature treatment in the manufacturing process. Ni/GDC anode paste, which is described in section 3.1.2.2, was then screen printed on the opposite side of the support and sintered at 1200 °C for 3 h. The LSCF cathode was then applied by screen printing and sintered at 1080 °C for 3 h. In addition, the ammonium molybdate tetrahydrate ($(NH_4)_6Mo_7O_{24}•4H_2O$, 99 %), (Alfa Aesar, USA) water-based solution was prepared with a density concentration of 0.4 M, and the solution was infiltrated in the anode structure by drop on the anode in a vacuum chamber. After infiltration, the residual solution on the anode surface was removed by blowing with air and the cell was dried in an oven at 80 °C for 8 h. Finally, the anode was calcined at 600 °C for 1 h.

3.2. Cell test

3.2.1. Single cell measurements at Karlsruhe Institute of Technology (KIT)

The single cell performance was measured in a test bench at the Institute for Applied Materials (IAM-WET, KIT), as described by Timmermann et al. [107]. The cells were contacted by Au mesh on the air side and Ni mesh on the fuel side. After a defined heat-up and reduction procedure, the current-voltage characteristics were recorded at 820°C using laboratory air (1000 sccm) as the oxidant and dry hydrogen (1000 sccm) as the fuel.

3.2.2. Long-term test with bio-syngas (TU Munich)

The cell was contacted by a Ni mesh and gold wire on the fuel side, and Au mesh with Au wires on the air side in an alumina housing. A load of 400 N was applied to sustain a good electrical contacting during the test. Simulated syngas with a composition of 50 % H_2O, 25 % H_2, 10 % CO_2, 10 % CO, and 5 % CH_4 was used as fuel, which is similar to real bio-syngas produced with allothermal fluidized bed gasification [108]. The tar species was added according to the experiment plans, and the content was adjusted by the temperature control of the tar station. The actual tar content was measured by the solid phase adsorption (SPA) method [109]. In the case of sulfur, 100 ppm H_2S/H_2 gas was used to prepare simulated syngas instead of H_2 to have 5 ppm H_2S content in total gas composition. The operation temperature was set to 700 °C, but the anode and support are pre-reduced before test under dry H_2 atmosphere at 900 °C. The fuel and air flow rates were 1 Nl/min and 2 Nl/min, respectively. The tests were performed in galvanostatic mode at a current density of 0.34 A/cm^2, and the voltage was recorded as a function of time.

3.2.3. Stack test with biomass gasifier (TU Munich)

The biomass feedstock was 8 mm diameter and 6 - 12 mm in length of wood pellets with low moisture and ash content, which has high energy density. The bubbling fluidized bed was used for gasification of biomass via a vibrating and feeding system from top. The superheated steam was supplied as oxidant gas from bottom. The gasifier was heated up electrically with two separated heating zones for the fluidized bed (790 °C) and the freeboard (600°C). 2 L of silica sand and 0.25 L of biomass char (from previous runs) were used as bed material. After the gasification, sulfur and chlorine were removed by catalyst of ActiSorb S2 and ActiSorb Cl2 Clariant (Clariant, Swiss). There were still certain contents of hydrocarbon fuel such as CH_4, C_2 - C_5, and especially tars, so a Ni-based catalyst was used for reforming of hydrocarbon fuels at 800 °C. The stack was operated with syngas after tar reforming (clean-syngas) during the first 2 h, and when a stable operating point was reached the tar cleaning was bypassed (tar-syngas). The composition of fuel and tar content is presented in Table 3.1 and various molecule structures of tars are presented in Figure 3.4.

Table 3.1: The composition of fuel and tar content

Composition			After gasifier	Clean-syngas	Tar-syngas
Fuel	H_2	v-%$_{db*}$	23.9	36.4	26.9
	CO_2	v-%$_{db}$	11.3	11.5	14.1
	CO	v-%$_{db}$	8.7	9.5	7.3
	CH_4	v-%$_{db}$	3.6	0.2	3.7
	C_2-C_5^{**}	v-%$_{db}$	1.5	0.0	1.5
	N_2	v-%$_{db}$	Bal.	Bal.	Bal.
H_2O		v-%	42.0	-	-
Impurities	H_2S	ppm$_{v\,db}$	12.2	0.0	0.0
	Benzene	g/Nm$^3_{db}$	0.9	0	0.8
	Toluene	g/Nm$^3_{db}$	0.6	0	0.5
	Phenol	g/Nm$^3_{db}$	0.9	0	0.5
	m-Cresol	g/Nm$^3_{db}$	0.6	0	0.2
	Naphthalene	g/Nm$^3_{db}$	0.2	0	0.2
	Other tars	g/Nm$^3_{db}$	1.8	0	1.3

* dry basis, ** not measured, average value in similar condition

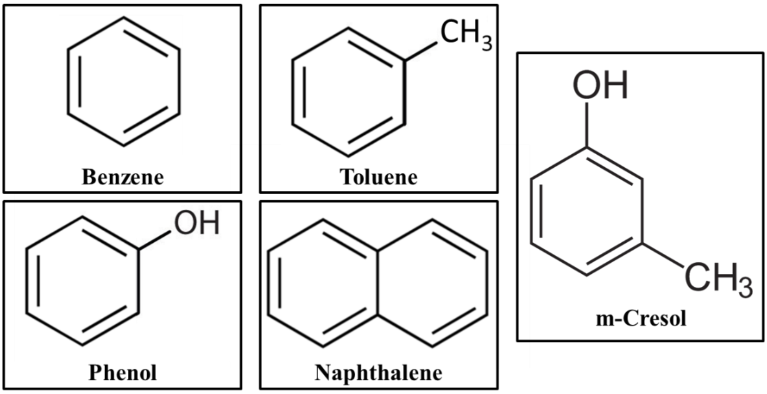

Figure 3.4 The molecular structure of various tar species

The stack was operated at 715 °C with a temperature measurement of each interconnect and cell frame. Fuel gas and air were supplied from the bottom of the stack via an adapter plate as shown in Figure 3.2. The test was carried out in galvanostatic operation mode with PLI 2106 controller (Höcherl & Hackl GmbH, Germany) at 0.5 (for 2 layer stack) and 0.25 (for 4 layer stack) A/cm². Each cell voltage was measured and recorded individually using a 4-channel data logger (Onset Hobo) and the stack voltage was recorded via two rods made of Inconel and two sense cables. The current rods were screwed to the bottom and the top plate of the stack and the sense cables consist of platinum wires that were welded to the end plates and interconnects and extended by silver wires to the respective measurement devices. The pressure drops of fuel inlet and air outlet were measured by comparison with ambient pressure, and the pressure drop of the entire stack was measured by comparing inlet and outlet pressures.

3.3. Characterization of precursor materials and cells after manufacturing

3.3.1. DTA-TG analysis

The reduction study of YSZ-GDC powder was performed by thermogravimetric measurements in a NETZSCH STA 449 F3 Jupiter using Al_2O_3 crucibles. Buoyancy was then corrected through a reference measurement with the empty crucible. For the oxidizing and reducing atmosphere, air and 2.9 % H_2/Ar gases were supplied.

The DTA-TG analysis was applied to various Mo containing materials, and the thermal stability and reaction temperatures of the $NiMoO_4$, $Ce_{1-x}Mo_xO_{2+\delta}$, and $Ce_{1-x-y}Mo_xGd_yO_{2+\delta}$ composites were analyzed.

3.3.2. Electrolyte leakage test

The half-cell leakage test was performed with air and He. The test principle measures gas that passes through the target by pressure change (air) or mass spectrometer (He). The values were then normalized by measured area and a typical pressure difference of 100 hPa for an SOFC stack [110]. Also, the internally determined maximum leakage rates are 8×10^{-6} for air and 2×10^{-5} $hPa \cdot dm^3 \cdot s^{-1} \cdot cm^{-2}$ for He for cells in the oxidized state.

3.3.3. X-ray diffraction (XRD)

X-ray diffraction measurements of raw material and synthesized samples were performed using a Bruker D4 diffractometer to analyze the crystal structure and phase transformation. The samples were scanned by Cu-Kα radiation with a step size of 0.02°. A subsequent Rietveld refinement method was applied to quantify the phase content as needed.

3.3.4. Conductivity measurement

The conductivity was measured by the four-point probe method, as shown in Figure 3.5, with Ag wire as contacting material using a custom-built setup in a tube furnace. The specimens were prepared as ceramic bars after sintering at 1400 °C for 5 hours. For the measurement, the specimens were first heated up to 870 °C, and the conductivity was measured every 50 °C from 850 °C down to 450 °C. Then, for the reduced state conductivity measurement, the sintered specimens were pre-reduced at 900 °C for 5 hours in a 2.9 % H_2-Ar atmosphere. The conductivity was measured with the same procedure but in a reducing atmosphere of 2.9 % H_2/Ar with a low oxygen partial pressure (P_{O_2}:10^{-18} to 10^{-20} atm).

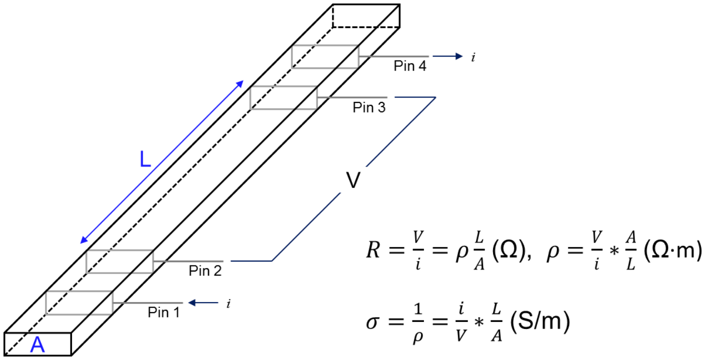

$$R = \frac{V}{i} = \rho\frac{L}{A}\,(\Omega),\quad \rho = \frac{V}{i} * \frac{A}{L}\,(\Omega\cdot\mathrm{m})$$

$$\sigma = \frac{1}{\rho} = \frac{i}{V} * \frac{L}{A}\,(\mathrm{S/m})$$

Figure 3.5: Schematic diagram of the four point-probe method

3.4. Post-test analysis of cells after poisoning test

3.4.1. An introduction of post-test analysis of cells after test

The cell test rig and contacting material for the fuel side is shown in Figure 3.6. The housing material was alumina and contains 20 gas channels. The current collecting contact material was Ni mesh with gold wire, which was inserted in every other channel of the alumina housing. In this study, the cell would be presented with always the same orientation as the support side up schematic diagram in Figure 3.6. There are three different possible changes that can appear after the cell test, and they are marked in Figure 3.6.

(1) Discoloration by fuel and impurities: The discoloration appeared near the fuel inlet after the phenol test with a brighter color than the non-changed area. This area was used to analyze the effect of impurities such as carbon deposition.

(2) Crack and re-oxidation: In many cases, cracks appeared after the cell test and re-oxidation by air cross over. If the cell does not show any significant performance change in the cell test, the cracks are assumed to be formed after the test while cooling down.

(3) Edge re-oxidation: Due to the small gap between cells with housing, the edge of the cell can be re-oxidized. Since the airflow is in the opposite direction of the direction of the fuel, the re-oxidation occurred near the fuel outlet.

Based on the three different possible changes, the cell was analyzed by various tools such as laser microscope, SEM, XRD, and Raman spectroscopy.

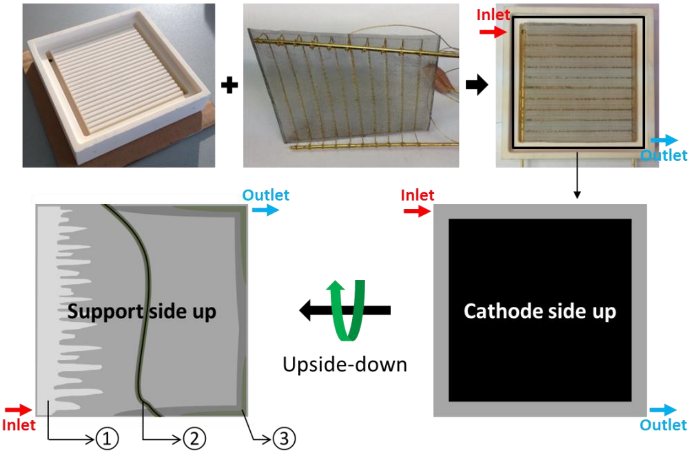

Figure 3.6: Photos of the alumina housing, contact material, and the schematic diagram of the cell after testing

3.4.2. Scanning electron microscope (SEM)

The microstructures of the raw materials and cells were analyzed by scanning electron microscope (SEM) using a Zeiss Gemini Ultra 55 electron microscope (Carl Zeiss NTS GmbH, Germany). The specimens were prepared by two different ways depending on the purpose of the measurement: surface and fractured cross-sectional images for morphology changes or detecting external particles after cell test, and polished cross-sectional images for microstructural changes or quantification of porosity or specific phase fraction.

3.4.3. Raman spectra

An inVia Raman Microscope (Renishaw, UK) was used for collecting Raman spectra using a 532 nm laser, a grating with 1800 lines/mm, and a CCD Detector. The Raman spectroscopy was applied after the cell test with tar or sulfur-containing fuel to detect carbon deposition or sulfide phases, and the cell surface or fractured cross-section was investigated by Raman point mapping with a step size of 2 µm. If necessary, the live track function (autofocus software solution) was applied.

Data processing was performed with the Wire software (Wire 5.1) as follows: In a first step, the cosmic rays were removed by the implemented process in the Wire Software. If necessary, spectra that saturated the detector during measurement were set to zero via the zap-procedure. A statistical noise filtering was also used to smooth the spectra. To obtain an average spectrum from the mappings of the anode, the background was subtracted and the spectra were averaged. Then, the mapping of the carbon distribution of the cross-sections was determined by using a statistical component analysis (Empty modeling, Wire 5.1).

4. Degradation of standard cells with impurities containing syngas

In the following sections, single cell tests with the state-of-the-art Ni/YSZ anode, using synthetic syngas with the controlled addition of single contaminants as fuel are presented and discussed. Finally, an SOFC stack test using a JÜLICH F10-design 4 layer stack coupled to a gasifier producing syngas from wood pellets is presented and discussed. The tests were performed at TUM, and the post-test characterization was performed in JÜLICH.

4.1. Single cell test with impurities containing simulated syngas

4.1.1. The cell microstructure before test

Figure 4.1 shows polished, cross-sectional SEM images of the IIIb and CeramTec full cell structure before testing. Although the manufacturing process and materials of the cells was nearly the same, the microstructure is different due to the different pre-treatment of raw materials, different tape casting and screen printing paste recipes and a difference in support thickness. The CeramTec cell (Figure 4.1a) shows more homogeneous and finer particles in cathode, barrier, and anode layer than IIIb cell (Figure 4.1b). In addition, the particle size in the support of the IIIb cells is larger than in the CeramTec cell. The differences in particle sizes are related to the thickness of the support: since the IIIb support is thicker (~ 550 µm) than CeramTec support (~ 300 µm), larger size particles are used for IIIb support to form a higher amount of large pores in order to avoid gas diffusion polarization in the support.

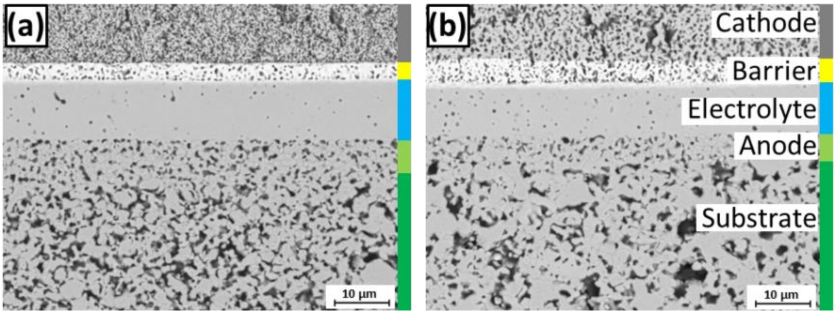

Figure 4.1: Cross-sectional SEM images of (a) CeramTec and (b) IIIb full cell structures in reduced state

4.1.2. Effect of phenol*

4.1.2.1. Cell test result (TU Munich)

The voltage-time plots of the tested cells characterized by post-test analysis are presented in Figure 4.2. The cell test with pure syngas (Figure 4.2a: denoted as SYN test) shows about 3 %/1000 h voltage degradation rate — the cell voltage drops from 0.813 V to 0.805 V during 250 h of operation. This degradation rate was higher than previously reported test results with humidified hydrogen fuel. For example, a 2 layer stack test with 20 % humidified hydrogen shows 0.9 %/1000 h, and a single cell test with 3 % humidified hydrogen shows 0.9 ~ 1.5 %/1000 h of voltage degradation [32, 111]. More recently, degradation rates below 0.3 %/1000 h have been achieved in stack operation at JÜLICH [112, 113]. Moreover, the voltage was also fluctuating during the whole test under syngas. The reasons for this high degradation rate and instability are estimated to be due to an unstable test rig, and/or degradation of electrical contact between electrodes and contacting materials, as well as degradation of the actual cell [114].

Figure 4.2b presents the result of cell operation on syngas, with 2 g/Nm^3 phenol introduced in multiple cycles (denoted as 2PHEN test). It shows a high degradation rate of 13 %/1000 h during the first cycle of phenol addition. However, when the phenol was removed after 50 hours, the cell voltage recovered and it did not exhibit a higher degradation rate in further phenol cycles. Moreover, the average degradation rate during 500 h of operation with 5 cycles of exposure to 2 g/Nm^3 of phenol (total exposure ~ 250 h) was about 3 %/1000 h, which is similar to the SYN test with pure syngas.

In a further test, the phenol content was increased stepwise from 1 g/Nm^3 to 8 g/Nm^3 (Figure 4.2c: denoted as 8PHEN test). The phenol content of 1 to 8 g/Nm^3 corresponds to common tar concentrations in bio-syngas. For example, total tar concentration ranges are 0.01 to 6 g/Nm^3 with downdraft fixed bed gasifier and 1.5 ~ 10 g/Nm^3 with fluidized bed gasifier [54]. The initial voltage was about 0.1 V lower than in the previous two tests. The difference is due to different cell types: in the SYN test and 2PHEN test, CeramTec cells were used whereas in this test, a IIIb cell was utilized. As already mentioned in the experimental part, the microstructure of the CeramTec cell was more homogeneous than IIIb cell. In particular, the IIIb cell shows an inhomogeneous microstructure of the GDC barrier layer, so that more insulating $SrZrO_3$ phase can be formed during manufacturing/sintering at the YSZ-GDC interface [34, 35]. This difference in microstructure seems to be the reason for the difference in initial cell performance. In terms of the

---

* This part (4.1.2) has been published in the journal "International Journal of Hydrogen Energy" Volume 43, Issue 45, 8 November 2018

degradation behavior, the 8PHEN test shows a similar tendency as the 2PHEN test — about 3 %/1000 h average voltage degradation with fluctuations. However, when a phenol concentration of 8 g/Nm^3 was applied, a drastic degradation rate of 200 %/1000 h was observed. The voltage increases by 0.013 V at the beginning of the phenol dosing cycle with 8 g/Nm³, followed by strong degradation. About 50 h after the beginning of phenol addition, there is a strong voltage recovery, although not to the initial value that was measured at the beginning of the exposure period with 8 g/Nm^3 phenol. The cell performance is not visibly affected by 2 g/Nm^3 during a relatively long time period of 250 h, but a strong, partly reversible degradation was observed when phenol content increased to 8 g/Nm^3. Thus, the cell performance seems more dependent on tar content than on exposure time.

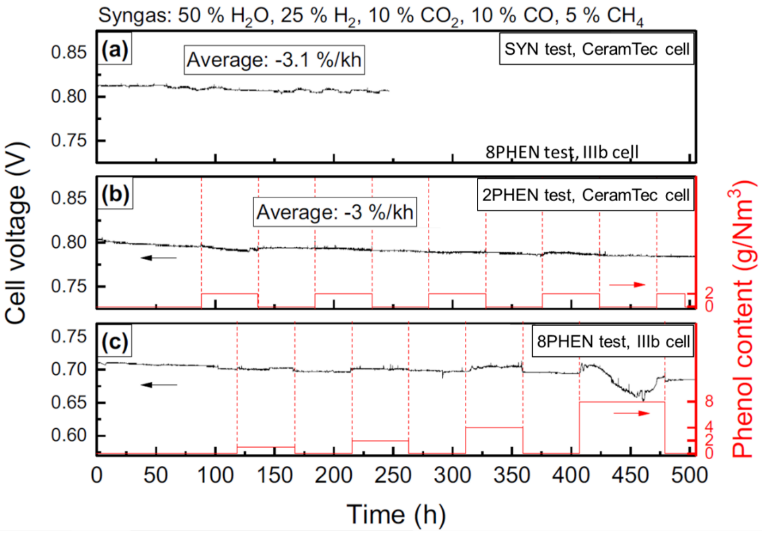

Figure 4.2: Voltage-time plot of syngas test (a: SYN), syngas + 2 g/Nm^3 phenol cycling test (b: 2PHEN), and the test with syngas + phenol with increasing concentration (c: 8PHEN) cell test (at 700 °C, 0.34 A/cm^2)

4.1.2.2. Structural changes after cell test

In order to analyze the effect of microstructural changes on the cell degradation, the tested cells were investigated by SEM. Optical images and SEM micrographs recorded on the surface of the support of each cell after testing are presented in Figure 4.3. The cell after SYN test (Figure 4.3b) shows cracks and re-oxidized areas (green color). However, the cell performance does not contain indications of significant gas leakage in the voltage-time plot (Figure 4.2a), so it is assumed that the cracks are formed during cooling down. The SEM images of the support surface at both the fuel inlet and outlet after SYN test (Figure 4.3a, c respectively) show a typical Ni/YSZ cermet structure. On the other hand, the pictures of the cells after the 2PHEN and 8PHEN tests (Figure 4.3e, h respectively) show a discoloration of the support surface, which proceeds from fuel inlet towards fuel outlet along the gas channels in the anode flow field. The surface SEM images of the fuel inlet areas show drastic microstructural changes (Figure 4.3d, g for 2PHEN and 8PHEN, respectively) in contrast to the fuel outlet area (Figure 4.3f, i for 2PHEN and 8PHEN, respectively), which is basically unchanged. The observed changes include the loss of connectivity between particles, as well as seemingly coarsened particles and increased porosity. Carbon fibers are sometimes observed in the inlet area after the 2PHEN test, as shown in the high magnification SEM image in Figure 4.3d, but no carbon fibers could be found in the outlet area. A higher amount of carbon fibers is observed in the inlet area of the cell after the 8PHEN test, and carbon fibers are also present in the outlet area (SEM micrographs set into Figure 4.3g and i, respectively). The large particle size in the inlet area after the 8PHEN test seems to be related with the different cell type (IIIb cell with coarser particles in support).

The pattern of discoloration consists of alternating, deep and shallow eroded trenches in the support for both the cells subjected to 2PHEN and 8PHEN tests, as can be seen in the line scan with confocal laser microscopy shown in Figure 4.3j. The deepest trenches have been eroded 150 μm into the support, which is roughly 1/3 of the entire support thickness. The erosion pattern correlates to the presence of the gold contacting wires that are inserted into every second flow channel — the flow channel with gold wires show shallow erosion, while those without show deeper erosion. In addition, the erosion of the support proceeds along the flow direction of the fuel gas (from inlet to outlet), and has progressed much further towards the outlet in the channels without contacting wires. This indicates that the gas flow has an influence on the erosion behavior, most likely because the flux density is higher in the flow channels without wires and therefore more tar is transported along these channels. Furthermore, the fact that the erosion proceeds along the channels and can also be observed in the entire area of the gas manifold (the area on the inlet side in front of the flow field) indicates that the erosion is correlated with the gas composition, for example the tar concentration in the fuel gas. A likely explanation is that the erosion is related with the cracking or reformation of the tar molecules in the support; this will be discussed in more detail below.

To summarize the main findings shortly, although the 2PHEN test does not show remarkable performance degradation like the 8PHEN test, both cells show strong support erosion. This result indicates that 2 g/Nm^3 of phenol does not change the electrochemical mechanism of the cell within the total phenol testing time of 250 h. However, it chemically reacts with Ni/YSZ support and changes its microstructure. We hypothesize that if the test continued for longer times, the cell performance would also be affected with low phenol content of 2 g/Nm^3, since the erosion of the support would eventually affect the anode performance if the erosion front exceeds to the functional layer.

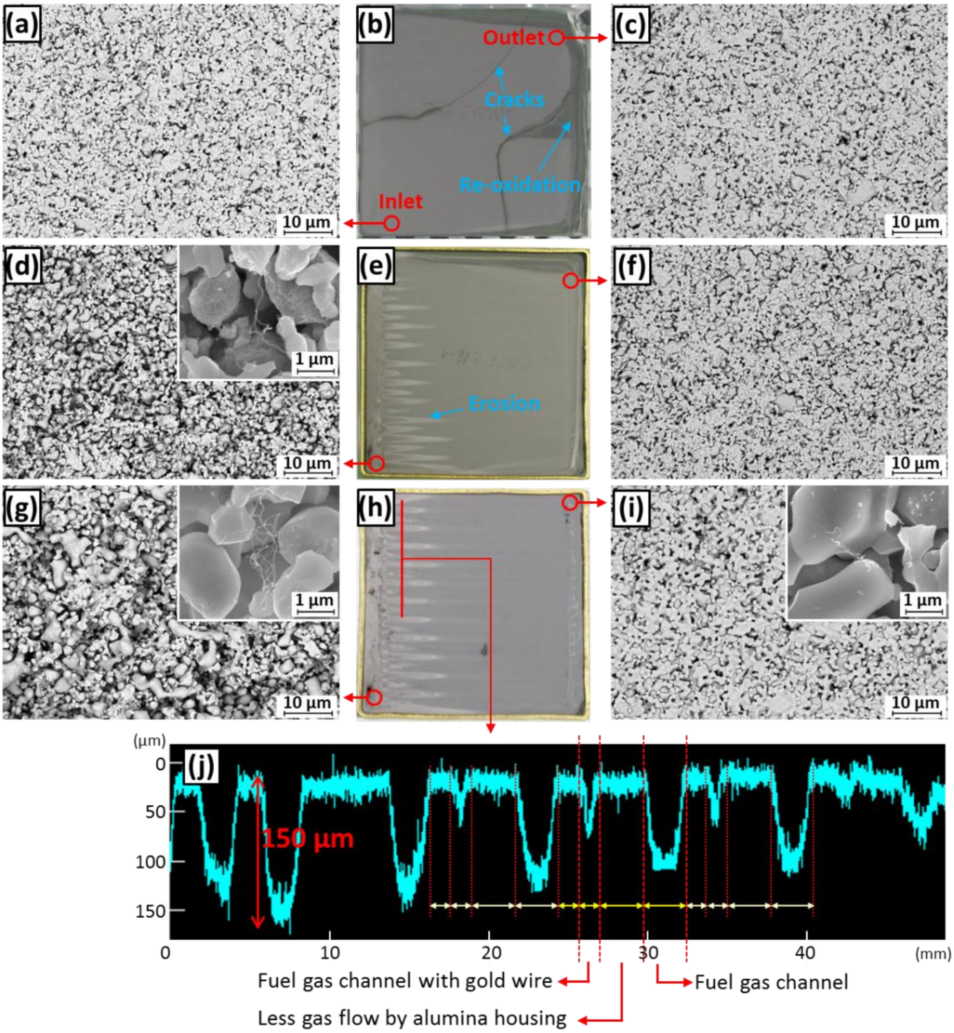

Figure 4.3: Support surface photos and SEM images after SYN test (a-c), 2PHEN test (d-f), and 8PHEN test (g-i), and a depth profile of the erosion pattern on the surface of the support after 8PHEN test (j).

Figure 4.4 shows polished cross-sections from the inlet area of each cell after the cell tests. From the SEM images, it can easily be seen that the microstructure in the eroded areas (Figure 4.4b, c) after the PHEN tests is completely changed, compared with the cell after the SYN test (Figure 4.4a). The cell after 8PHEN test (Figure 4.4c) also shows a larger particle size than the others. However, the original particle size of IIIb support was also larger than the CeramTec support (see Figure 4.1), thus the larger particle size likely originates from the different raw powders of the support. The pore fraction was calculated from the corresponding SEM images by quantification of pore (dark) area with image analysis software (Image J), and the Ni content of each microstructure was calculated from EDX data Using Equation 4.1.

$$\text{Ni content} = \frac{[\text{Ni}]}{[\text{Ni}] + [\text{Zr}] + [\text{Y}]} \times 100\ (\text{at.}\,\%) \qquad \textbf{Equation 4.1}$$

As a reference for the initial microstructure, cell pieces of IIIb and CeramTec cells are reduced in 2.9 % H_2/Ar atmosphere and prepared as polished cross-sections. The porosity and the Ni content of the tested cells, along with the data for the reference cells reduced in 2.9 % H_2/Ar, are presented in Table 4.1. The reference cells and cell after SYN test show about 25 % porosity. Although CeramTec and IIIb cell show different microstructure, the total volume fraction of porosity was comparable. However, the material erosion in the fuel inlet area of the cells after the 2PHEN and 8PHEN tests increases the porosity to 59.7 and 58.5 %, respectively; the porosity has more than doubled. This high porosity value is well corresponding with SEM image of Figure 4.4 with reliable standard deviation value.

The reference cells and the cell after SYN test show about 66 at-% of Ni content. On the other hand, after the 2PHEN and 8PHEN tests, the Ni content was 53.8 and 53.6 at-% , respectively, which is more than 10 %-points lower than the Ni content of phenol free cells. This result indicates that Ni is preferentially removed from the support in the presence of phenol. However, 10 %-points of Ni depletion are insufficient to explain such a high increase in porosity, from which we deduce that YSZ is also lost during the erosion.

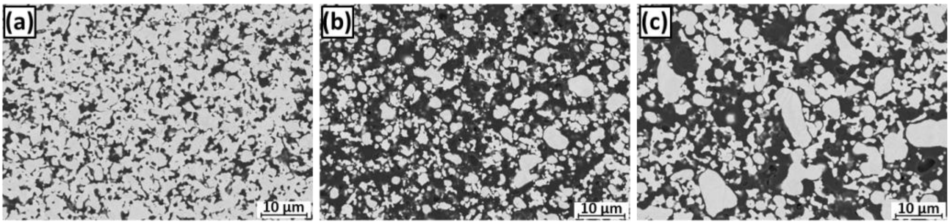

Figure 4.4: Polished cross-section of the cell supports in the fuel inlet area after SYN test (a), 2PHEN test (b), and 8PHEN test (c)

Table 4.1: Porosity and Ni content of 2.9 % H_2/Ar reduced reference cell and syngas tested cell

Cell type	Test	Porosity (%)	Ni content (at-%)
CeramTec	H_2/Ar reduced	26.7 (0.6)*	65.8 (1.5)**
JÜLICH IIIb	H_2/Ar reduced	24.8 (1.0)	67.4 (1.6)
CeramTec	SYN	25.1 (0.1)	65.1 (1.6)
CeramTec	2PHEN	59.7 (0.7)	53.8 (1.1)
JÜLICH IIIb	8PHEN	58.5 (1.1)	53.6 (1.1)

* Standard deviation ** Error (%)

Figure 4.5 shows the X-ray diffraction pattern from the support inlet area and the dusty powder that was collected from the alumina housing underneath the anode side after 2PHEN and 8PHEN tests. The XRD result from the support at the fuel inlet shows Ni and YSZ patterns without any detectable secondary phases. Since the XRD patterns of cubic and tetragonal YSZ are indistinguishable in the present conditions (small particle size, low angular resolution of the detector), both cubic and tetragonal phase are denoted with Y.

From the literature, it is known that 3YSZ has a tetragonal (CeramTec cell, 2PHEN) and 8YSZ a cubic unit cell (IIIb cell, 8PHEN) [115]. In the case of 2PHEN test, a monoclinic YSZ phase was detected as well due to the phase instability of 3YSZ [115, 116]. The XRD results from the collected powder show also both Ni and YSZ phases, which proves the erosion of not only Ni but also YSZ. Monoclinic zirconia is detected from the dusty powder eroded from the CeramTec cell as well. It has been reported than Ni and Ni-based alloys show metal dusting or Ni depletion in the SOFC anode [11, 67-69, 75], but YSZ is known as a relatively stable material. The YSZ bulk or grain boundary reactivity to carbon and the relation between Ni depletion and YSZ depletion is unclear. Therefore, further study is necessary to explain the YSZ erosion mechanism.

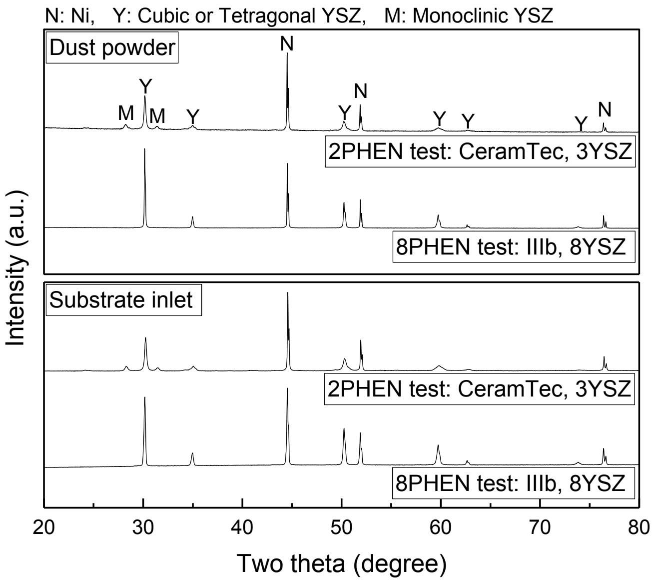

Figure 4.5: XRD results of the support in the area of the fuel inlet and the powder collected from the alumina housing after PHEN test

4.1.2.3. Raman spectroscopy of cells after test

Raman spectroscopy was used to detect carbon deposition on the anode and support material surface. Figure 4.6 shows Raman spectra collected on the surface of the support in the inlet and outlet positions, which is the same position as marked in Figure 4.3. Although the total operation time of SYN test was 250 h, which is half of total phenol test time of 500 h, it was in principle long enough for carbon deposition to occur. However, carbon peaks were not detected from either the inlet or outlet areas of the cell after SYN test, indicating that the steam-to-carbon ratio is high enough to prevent carbon formation in syngas. On the other hand, the peaks of disordered (D) and graphitic (G) carbon were detected at the Raman shift of 1350 and 1580 cm^{-1}, respectively, from the cell inlet area after 2PHEN and 8PHEN test. The 8PHEN test shows a higher carbon peak intensity and larger area of carbon deposition compared to the 2PHEN test. Carbon peaks are also detected in the outlet area after the 8PHEN test. We conclude that phenol is the cause of carbon deposition on the materials surface. These findings agree nicely with the microstructural changes and detection of carbon fibers by SEM shown in Figure 4.3, which also occurred only for the PHEN tests.

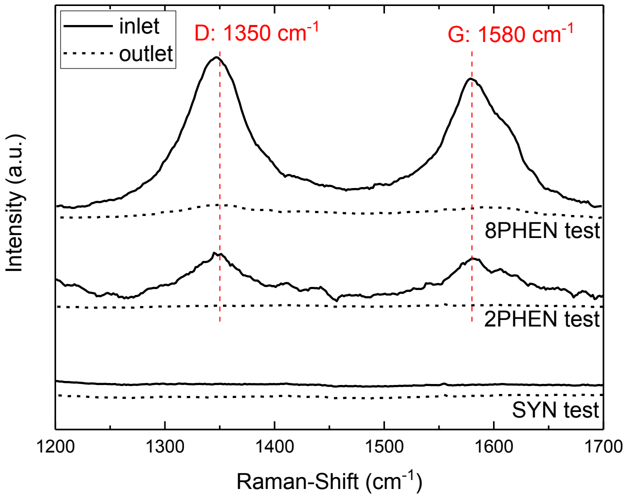

Figure 4.6: Raman spectra of cell support inlet (solid line) and outlet (dotted line) area after SYN test, 2PHEN test, and 8PHEN tests

To examine the carbon deposition throughout the support, fractured cross-sections were investigated by Raman spectroscopy. Since the Raman results of the support surface after the SYN tests did not show any carbon peak, the measurement was carried out only for the 2PHEN and 8PHEN samples. The results with a schematic diagram of the measured areas are presented in Figure 4.7. The thickness of the remaining support was 160 µm and 220 µm for the samples after 2PHEN and 8PHEN test, respectively. The distributions of detected carbon are indicated by a red color scale in the area from electrolyte to support. Brighter red means higher spectral intensity in the spectral range corresponding to the carbon signal. The cell after 2PHEN test shows carbon deposition in a limited area close to the support surface only (Figure 4.7a). In contrast, the cell after 8PHEN test shows carbon deposition throughout the entire support, while the amount of detected carbon clearly decreases from the support surface towards the anode layer (Figure 4.7b). Exemplary Raman spectra for spots 1 and 2 are provided in Figure 4.7. The fractured cross-sections were also investigated by SEM from near surface to near anode layer. The SEM images of fractured cross-sections of cells after 2PHEN and 8PHEN tests are shown in Figure 4.7a and b, respectively, with carbon fibers clearly visible. The cell after 2PHEN test shows only a few carbon fibers in a limited area near the support surface, whereas the cell after 8PHEN test shows numerous fibers up to a distance of roughly 100 µm from the support surface. However, SEM can only provide limited information that is restricted to the areas under investigation, whereas the Raman results are collected across the entire cell cross-section. We therefore assume the Raman results to be more reliable in this regard. Furthermore, it is possible that another species of carbon deposit exists in addition to the fibers, which may not be imaged well with SEM. For example, the carbon fibers growing from the catalyst surface are related to carbon nanotubes (which are commonly grown from methane using a transition metal catalyst, e.g. Fe), which are chemically similar to graphene (sp^2-hybridized carbon species). Since graphite consists of layered graphene sheets, we can assume that the G-line in the Raman spectra corresponds mostly to the carbon fibers, while the D-line may indicate a disordered or amorphous carbon species that is not easily detected by SEM.

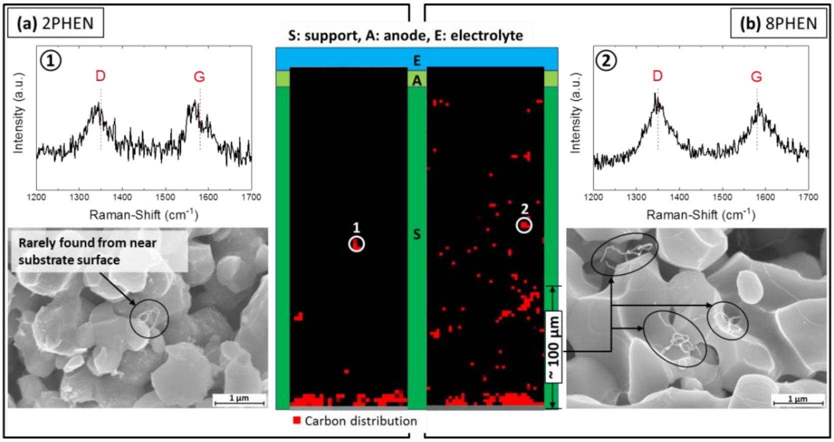

Figure 4.7: Carbon deposition analysis of fractured cell cross-section after 2PHEN and 8PHEN test; carbon distribution mapping by Raman with example spectra and carbon fibers observation by SEM

4.1.3. Effect of naphthalene

4.1.3.1. Test result (TU Munich)

Figure 4.8 shows the result of a cell test using syngas with naphthalene using a CeramTec cell with the same operating conditions as the previous test. The test was started with syngas, and 0.5 g/Nm^3 of naphthalene was added in two cycles alternating with syngas (NAPH test). The initial voltage was about 0.82 V at 700 ℃ with a 0.34 A/cm^2 current density, and there was no significant voltage degradation during 65 h, which is a similar trend for the test with pure syngas (SYN test). In the first naphthalene cycle, the voltage significantly drops immediately after the introduction of naphthalene opposite to the tests with phenol, showing relatively stable performance during a few hundred hours with phenol even with a higher content of 2 g/Nm^3. The voltage degradation rate was about 375 %/1000 h during 80 h, and the voltage stabilized at about 0.680 V. Although the voltage was recovered during the syngas operation after the first naphthalene cycle, the voltage was about 0.04 V lower than the initial performance after 180 h. In the second naphthalene cycle, the degradation rate was higher than the first cycle (about 780 %/1000 h). However, the voltage stabilized in a shorter time than in the first cycle, and the voltage reached a steady state similar to the value in the first cycle.

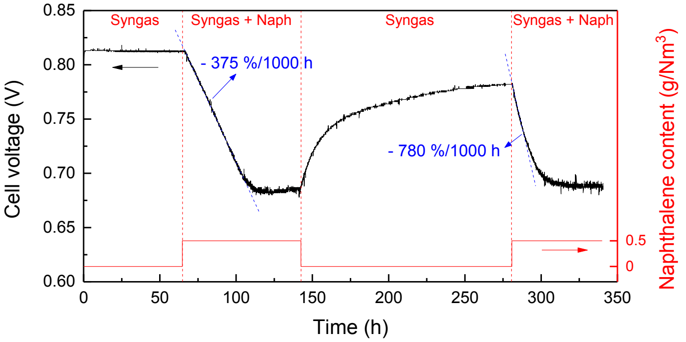

Figure 4.8: Voltage-time plot of syngas + naphthalene test (NAPH) at 700 °C, 0.34 A/cm^2

4.1.3.2. Microstructural and phase analysis

Figure 4.9 shows a picture of the cell and fractured cross-sectional SEM images after the NAPH test. Several cracks and discoloration were observed from the support side cell picture (Figure 4.9a) by the re-oxidation of Ni to NiO. However, similar to SYN test, the cell performance did not show any indication of gas leakage that caused the cell to break (Figure 4.8), so it is assumed that the cracks again formed during cool down after the cell test. There was no macro-scale structural change on the support unlike the support after phenol test; thus, the inner cell structure was investigated by SEM. Figure 4.9b shows the fractured cross-sectional SEM image of the outlet area, and the figure shows two different particle morphologies in the structure: particles with relatively flat surfaces and sponge-like surfaces. The particles with sponge-like surfaces seem to be re-oxidized NiO according to the similar observations in the literature [117, 118]. Furthermore, the XRD result of the support outlet area shows the NiO phase, as shown in Figure 4.10, corresponding to previous estimations. The Ni metal phase was also presented in the result, which was estimated as the remaining Ni at the core of NiO. The result shows the YSZ phase transformation as well the transformation from the tetragonal structure to the monoclinic structure due to the instability of 3YSZ which was already described in section 4.1.2.3. In the case of the fuel inlet area, the fractured cross-sectional SEM images of the anode (Figure 4.9c) and the support (Figure 4.9d) show the typical Ni/YSZ cermet structure since it was not re-oxidized due to the H_2/N_2 gas flow from the fuel inlet during cool down. Additionally, numerous nano-scaled particles were observed on the support and anode layers. These particles are also estimated as carbon species, but the size and the shape of the carbon structure were different from carbon fibers or filaments that formed after the PHEN test. One of the reasons for different types of carbon formation can be the test time. The cell operation time with naphthalene (~ 130 h) was shorter than the time with phenol (~ 250), so there was not enough time to grow fibers or filament structures. Otherwise, the tar reforming and carbon deposition mechanism can differ between phenol and naphthalene.

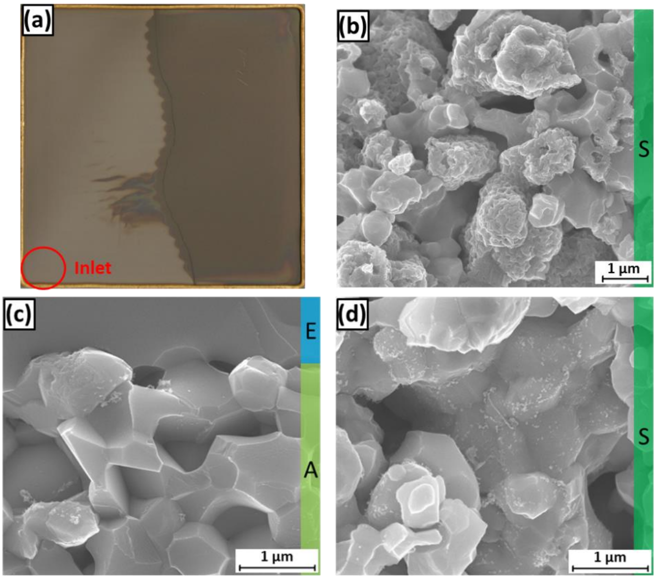

Figure 4.9: Cell photo (a) and fractured cross-sectional SEM images of outlet support (b), inlet electrolyte and anode (c), and inlet support (d) after the NAPH test

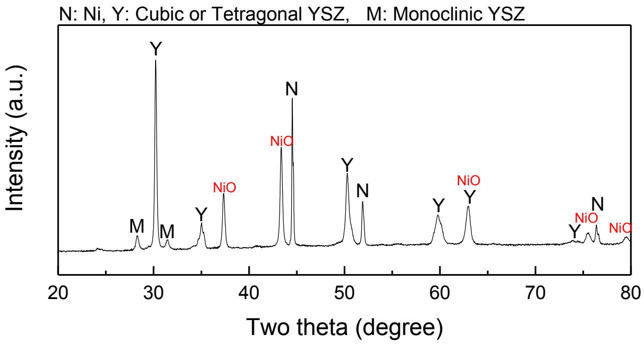

Figure 4.10: XRD result of the Ni/YSZ support surface in the outlet area after the NAPH test

4.1.3.3. Raman spectroscopy of cells after the NAPH test

Figure 4.11 shows the Raman spectroscopy result of the inlet area of the support surface the after NAPH test. The Raman result shows the spectral pattern of the D band at 1350 cm^{-1}, the G band at 1580 cm^{-1} and the D’ band at 1620 cm^{-1}. As already described in section 4.1.2.4, the D bands are due to disordered carbon species, such as amorphous carbon, and the G band is due to graphene or a layered graphene structure (graphite, carbon nanotube, and carbon fiber) [119]. The result shows D’ band more clearly than the PHEN test result in Figure 4.6. The D’ band is also induced by disordered carbon nano-crystalline graphite [120]. The Raman result shows the carbon clearly in the support with ordered and disordered structure, and the small particles in SEM images are estimated as being one of the carbon species.

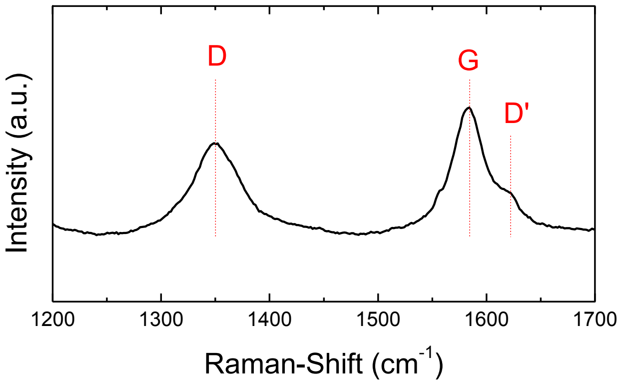

Figure 4.11: Raman spectra of the cell support inlet surface after the NAPH test

4.1.4. Effect of H_2S

4.1.4.1. Cell test result

Figure 4.12 shows the test result of the CeramTec cell with syngas and 5 ppm of H_2S as a sulfur poisoning substance (H_2S test). The initial cell voltage was about 0.81 V at 700 ℃ with 0.34 A/cm^2, and the cell shows steady operation with syngas for about 50 h, which is similar to the SYN test result. When 5 ppm of H_2S was applied, the voltage dropped instantaneously, and it shows a voltage drop of about 0.15 V in 4 h. The voltage decreased without changes in the degradation rate; therefore, the H_2S supply was stopped after 4 h to test its recovery behavior. Then, the voltage was increased with syngas operation without H_2S, but the voltage reached only about 0.75 V after 50 h. The cell voltage was further increased by the supply of dry hydrogen, but it was saturated again at about 0.77 V. Several studies have reported that surface chemisorption of sulfur on the Ni occurs at low content of sulfur, causing significant degradation in a short-term period by reducing the catalytically active area [15, 121, 122]. The cell test result shows the typical sulfur poisoning behavior of a fast and sensitive response to sulfur.

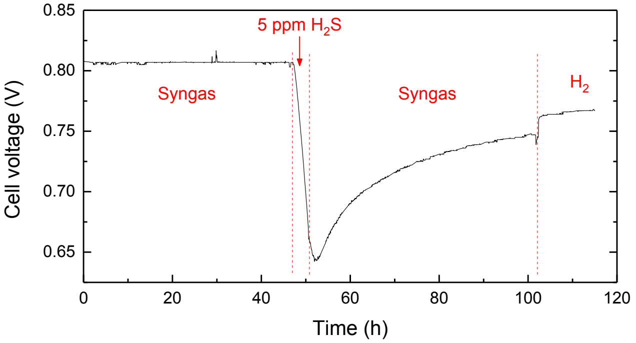

Figure 4.12: Voltage-time plot of syngas + H_2S test at 700 °C, 0.34 A/cm^2

4.1.4.2. Microstructural and phase analysis

As shown in Figure 4.13 a), the cell picture shows cracks and re-oxidation that is estimated to occur while the cell cools down, which is similar to the NAPH test in Section 4.1.3.2. The cell support near the outlet area also shows the re-oxidized NiO and YSZ structure, as shown in Figure 4.13b. In the case of the inlet area, the cell anode and support show particles similar to the support after the NAPH test, but the number of particles was much less. The XRD measurement was performed to analyze the phase changes of the support such as the Ni_xS_y formation. Figure 4.14 shows the XRD result of the inlet and outlet support surfaces, and the XRD result of the support after the SYN test was presented together as a comparable reference. There was no considerable difference between the inlet results after the SYN and H_2S tests, indicating no phase transformation. The result of outlet support also shows the NiO peak with a higher intensity than Ni. Thus, the cracks are formed at relatively high temperature, causing strong re-oxidation kinetics. In both the support inlet and outlet XRD results, the sulfur-related phase was not detected such as Ni_4S_3, Ni_3S_2, and NiS. Consequently, either there is no sulfide formation or the sulfide phase concentration is below the detecting limit of XRD.

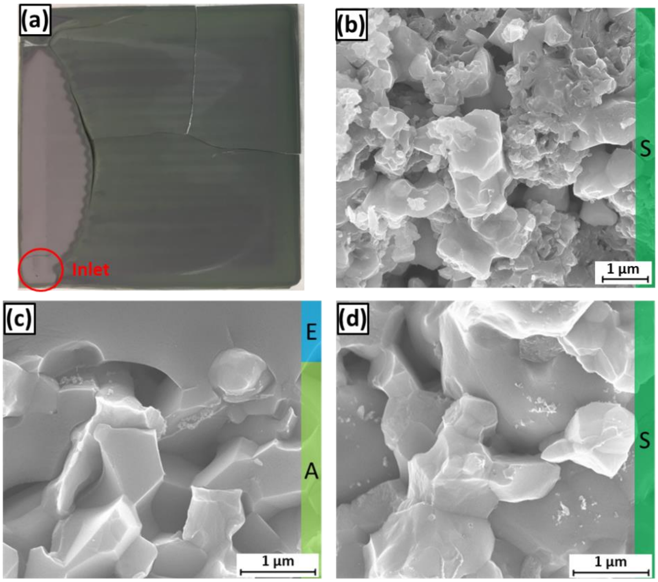

Figure 4.13: Cell photo (a) and fractured cross-sectional SEM images of the outlet support (b), inlet electrolyte and anode (c), and inlet support (d) after the H_2S test

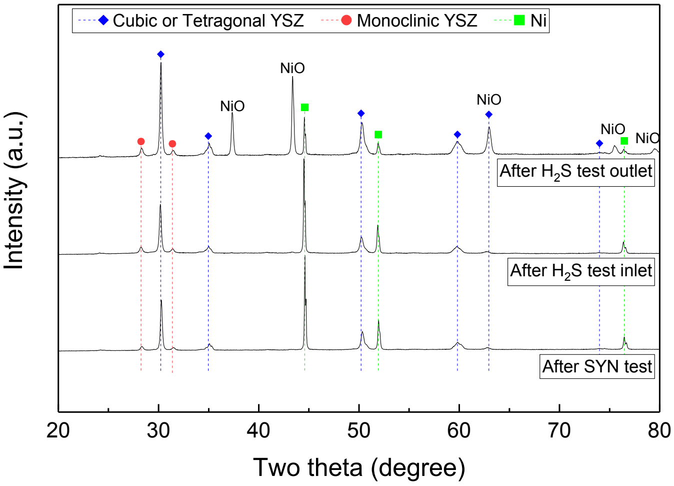

Figure 4.14: XRD result of the Ni/YSZ support surface from fuel inlet and the outlet area after NAPH test and referent result of the support after the SYN test

4.1.4.3. Raman spectroscopy of cells after the H_2S test

Raman spectroscopy was used to detect surface Ni_xS_y formation, which was not observed in XRD measurement, since the Raman is more surface sensitive. Figure 4.15a shows the result of support surface Raman spectroscopy after the H_2S test, and the reference Raman result of zirconia material with different crystallographic structures are presented together in Figure 4.15b-d. The Raman shift for both zirconia phase and Ni_xS_y phases are detected in the range of 100–1000 cm^{-1}; therefore, the zirconia peak was identified first by comparing with the reference result. Through the comparison with a reference sample, the YSZ spectra in the support (Figure 4.15a) were identified as a mixture of all the tetragonal and monoclinic phases that are already shown in XRD results in Figure 4.14. Actually, the existence of the cubic phase is ambiguous due to peak overlap with the tetragonal phase. However, the support material was 3YSZ, which is partially stabilized zirconia and has tetragonal structure [123-125]. Except for the zirconia peaks, there was no identical result for any kinds of Ni_xS_y phases compared to the previously reported result [16, 126, 127]. Additionally, there was no carbon deposition found in the range of 1300-1700 cm^{-1}.

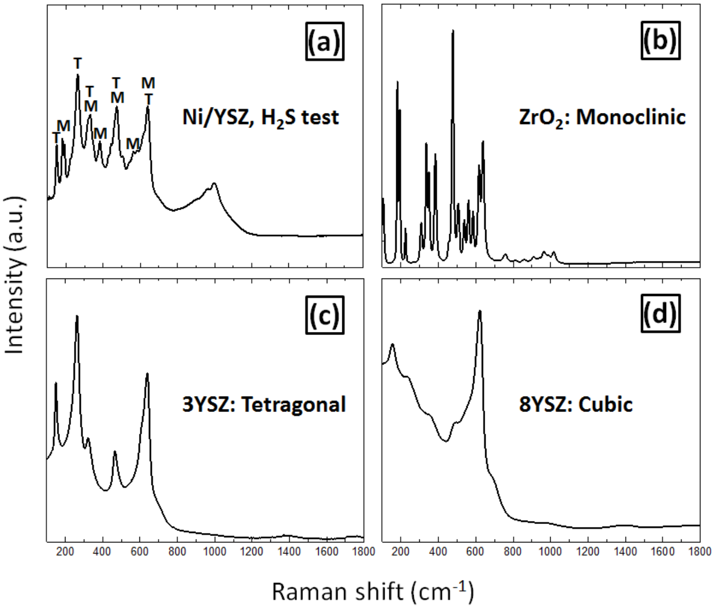

Figure 4.15: Raman spectra of the Ni/YSZ support after the H_2S test (a), and the reference zirconia spectra of ZrO_2 (b), 3YSZ (c), and 8YSZ (d)

4.2. Stack test with real bio-syngas*

4.2.1. Stack performance (TU Munich)

The stack test results are presented in Figure 4.16, showing voltage, current and the pressure drop across the stack as a function of time. The test was started with clean-syngas (bio-syngas with removed tar, sulfur, and chlorine). The open-circuit voltage (OCV) was almost identical for all four cells (0.97 V) which is a lowered value by diluting of fuel with N_2, CO_2 and a higher steam fraction compared to the OCV value of 1.05 V under 20 % humidified hydrogen at 700 ℃. During operation at a current density of 0.25 A/cm², cell 1 shows a lower voltage (0.75 V) than the other three cells (0.84 V) during the test. This is a well-known feature of the JÜLICH stacks [128], but the reason is not fully understood yet. One possible reason is the cell 1 is located at the bottom position in the stack where the temperature is always lower than for the other layers shown in Figure 3.2. The lower temperature reduces the ionic conductivity of the electrolyte and increases the activation polarization of the electrodes. The performance of all cells was stable with clean-syngas for an operation time of 2 hours. After the test with clean-syngas, a mixture of H_2/N_2 was applied at the anode side for one hour under OCV and an I-V curve was recorded for electrochemical characterization. The syngas with tars (with removed sulfur and chlorine, but tar reformer bypassed; called tar-syngas from here on) was then applied to the stack. Before the test, the tar species were identified through the solid phase adsorption (SPA) method [109] as total content of 3.5 g/Nm^3 including benzene, toluene, phenol, naphthalene, m-cresol, and minor traces of undefined tars as shown in Table 3.1. During the tar-syngas test, cell 1 shows again lower initial voltage than the others, in the same manner as in clean-syngas test, but the voltages of cells were similar as the voltage during clean-syngas test. Although the test does not shows significant power loss or cell failure, the test was terminated after 5 hours on real syngas since an increase of the pressure drop across the stack triggered an overpressure-safety valve in the gas supply line to open.

As an attempt to clarify the effect of tar on stack, another stack was operated under clean-syngas with relatively longer time period of 15 h. Figure 4.17 shows the test result of 2 layer stack with 2 cycles of operation. The test result shows a stable voltage (about 0.7 V for cell 1 and 0.72 V for cell 2) and stack pressure over the whole test period at a current density of 0.5 A/cm².

The I-V characterizations of individual cells in stacks were performed before, during, and after stack test. In the case of the stack test with tar-containing syngas (Figure 4.18a), cell 1 shows much higher

---

* This part (4.2) has been published in the journal "Journal of The Electrochemical Society" Volume 166, Issue 2, 30 January 2019

performance degradation than the other cells: about 2.5 % lower power output at 0.25 A/cm^2 under dry hydrogen atmosphere compare to the power output before test with same condition, while the other cells show about 1 % lower power. The performance loss was not high, but it is a considerable value in the short operation time of only about 5 h. On the other hands, after only clean-syngas operation (Figure 4.18b), cell 1 shows slight lower performance, but cell 2 shows almost identical I-V curves after 15 h operation.

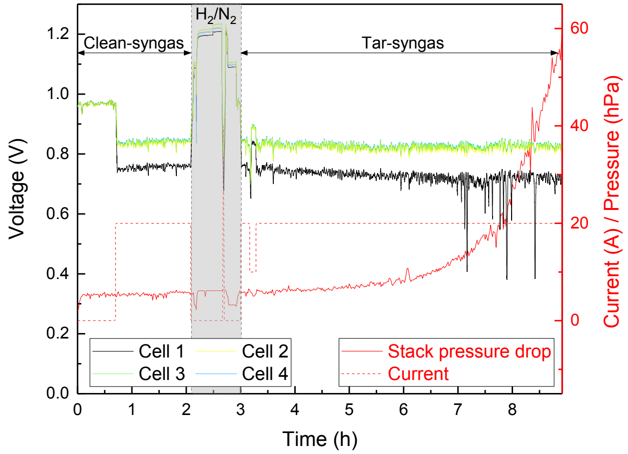

Figure 4.16: Stack test result with cleaned syngas (tar, sulfur, and chlorine removed) and tar-syngas (sulfur and chlorine removed) at 715 ℃, 0.25 A/cm². Note: the voltage curves of cell 2 to 4 (yellow, green, and blue) overlap completely

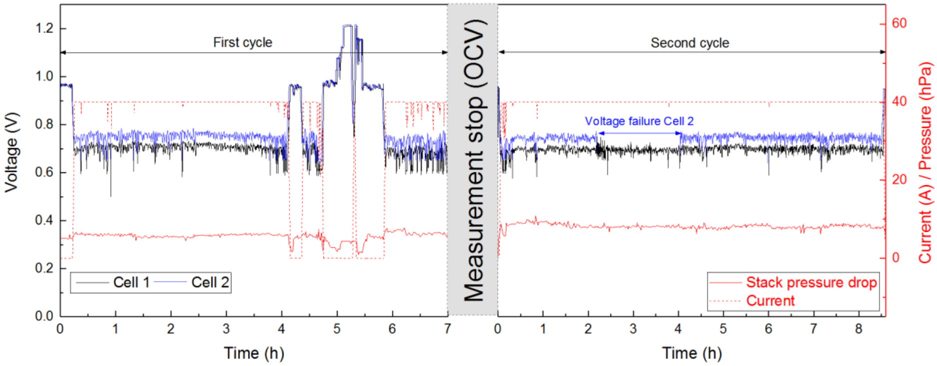

Figure 4.17: Stack test result with clean-syngas at 715 ℃, 0.5 A/cm²

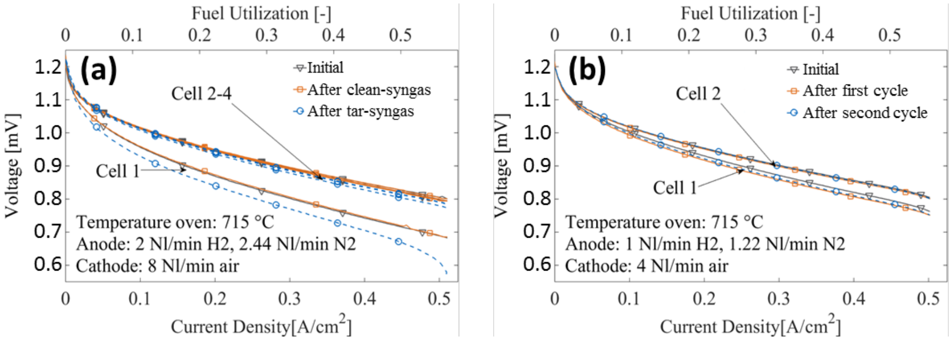

Figure 4.18: I-V characterization before, intermediate, and after stack test with clean- and tar-syngas (a, correspond to Figure 4.16) and clean-syngas (b, correspond to Figure 4.17)

4.2.2. Post-test analysis: optical investigations

After stack operation, the stack was opened at ZEA-1 in JÜLICH and a post-test analysis was performed. Figure 4.19 shows optical photographs of cells with frames and interconnects after test and disassembly according to [129]. In Figure 4.19a, the entire cell No. 1 with gas manifolds, the whole frame, and from the other three layers only the fuel-in manifold areas are presented. All four cells show heavy carbon deposition on the support surface near the fuel inlet (black). Since carbon deposition was not observed after stack operation using clean-syngas as shown in Figure 4.19b, the tar is estimated as the cause of carbon deposition. This carbon deposition was more pronounced at the edge of the cells. Another visible change of the cell is a discoloration on the support surface downstream from the area where carbon was deposited (more light grey). The image of cell 1 appears slightly different since all carbon powder was removed for chemical analysis. Figure 4.19c shows the photo of an interconnect in the stack with a Ni mesh current collector. Similar to the cells, carbon deposition is also observed on the Ni mesh near the area of the fuel inlet. It is obvious that only Ni plays the role of catalyst for carbon formation since there was no carbon deposited on the stainless steel interconnect surface. Carbon deposition in the Ni meshes was found in each layer. Figure 4.19d shows a cross-sectional optical microscope image of the mesh structure. The image shows a clear boundary between carbon (darker area) and polymer resin (brighter area) which was used for sample preparation. The carbon deposition shows thick and dense structure which seems to be enough to hinder the fuel gas flow and cause the pressure drop of the stack. On the other hand, there was no carbon deposition on the Ni mesh after clean-syngas test (Figure 4.19e). Additionally, both, cell frame and interconnect show discoloration near the fuel inlet area. It is estimated to be a Cr- and Mn-oxide scale, which appears after test with not only hydrocarbon fuel but also pure hydrogen. Therefore, this discoloration seems to be not a result of tar addition in the fuel, but the oxidation behavior of the interconnect material itself.

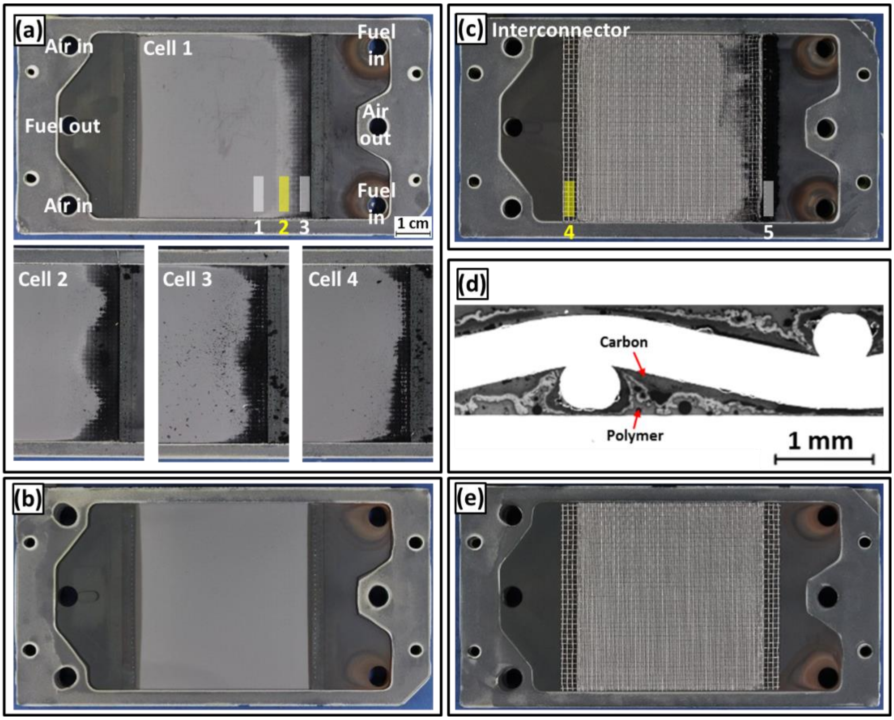

Figure 4.19: The photo of cells with frame after tar-syngas test (a), clean-syngas test (b); the photo of interconnects after tar-syngas test (c), and clean-syngas test (e); the cross-sectional optical microscope image of contacting Ni mesh (d)

4.2.3. Carbon deposition and microstructural changes

From the cell photographs, the cell support surface shows two visible changes: carbon deposition and discoloration. For the microstructural analysis, SEM is used at three different areas: optically unchanged area (1), discolored area (2), and the area with accumulated carbon (3), which are indicated in Figure 4.19. SEM images of these areas are presented in Figure 4.20 with different magnifications. The image of the unchanged area (Figure 4.20a) shows a typical Ni/YSZ anode surface morphology. On the other hand, the SEM image of the discolored area (Figure 4.20b) shows structural changes that include the loss of connectivity between particles, as well as seemingly coarsened particle sizes. A similar result of structural changes and discoloration of the anode support was reported in a previous study about single cell tests with phenol in simulated syngas [72, 114]. The SEM image of the area with strong carbon deposition (Figure 4.20c) shows a complete surface coverage by carbon fibers. Several studies reported similar results of carbon-fiber formation in the anode or anode support after dry hydrocarbon fuel tests [11, 130, 131], but it is unusual in steam reforming tests with light hydrocarbons, especially with such heavy surface deposition. As shown in the high magnification images of the carbon fibers, Ni particles were also observed at the tip of carbon fibers. This type of carbon growth has been reported in studies of methane reforming with a Ni catalyst [132-134]. The Ni particle sizes at the tip of the fibers are significantly smaller than the initial ones.

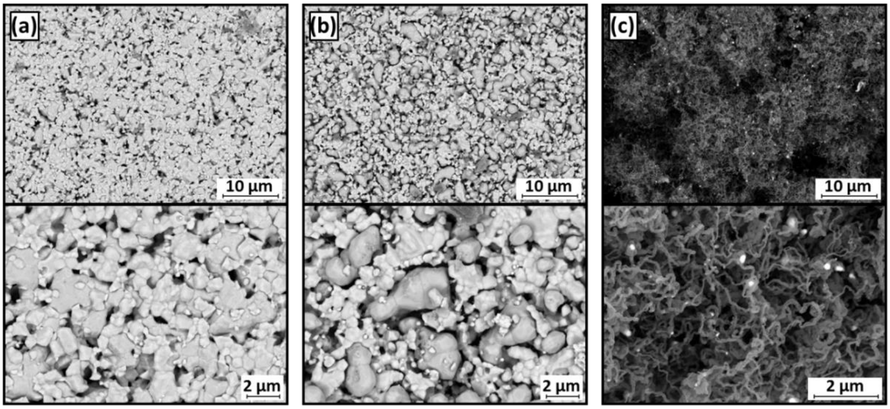

Figure 4.20: Surface SEM images of anode support with low (upper images) and high (below images) magnification from different positions, the figure labels (a), (b), and (c) are correspond with the area of 1, 2, and 3 in Figure 4.19

Figure 4.21 shows polished cross-sectional SEM images of the anode support and their EDX element mapping images for Ni and Zr (representing YSZ). The image of the unchanged area in Figure 4.21a (area 1 in Figure 4.19) shows a porous Ni/YSZ microstructure with strong connectivity between particles. The EDX mapping images show a relatively homogeneous distribution of both Ni and YSZ particles. The discolored area in Figure 4.21b (area 2 in Figure 4.19) shows a different microstructure compared with the unchanged image in Figure 4.21a. It shows less connectivity between particles, with a larger amount of pores (dark area). The discoloration can be explained by a change in the optical reflectivity through a roughening of the surface. Structural changes are mainly caused by a coarsening of the Ni particles as shown in Figure 4.21b, while there was no considerable change in the YSZ microstructure. The microstructure in the area showing heavy carbon deposition (area 3 in Figure 4.19) is presented in Figure 4.21c. In the cross-section, carbon deposition on the material surface is not visible since a carbon-based polymer resin was used for sample embedding, which is almost indistinguishable from the carbon deposited during the stack test. However, the thickness of the carbon deposition layer is estimated to be about 40 to 50 µm by the distribution of Ni and YSZ particles which are detached from the support. These detached particles in the carbon deposition layer indicate that the carbon has not simply accumulated on the support surface, but is caused by interaction with Ni and/or YSZ. The EDX mapping images show a smaller quantity of Ni than YSZ and reduced size of Ni particles compared to the unchanged image (corresponding with Ni particles at the tip of carbon fibers in Figure 4.20c). It seems then, that Ni acts as catalyst for carbon fiber growth and the particle size was reduced by metal dusting behavior [67-69]. While YSZ particles were physically pushed away from the support by carbon fiber growth, the YSZ particles do not show apparent changes of size or shape.

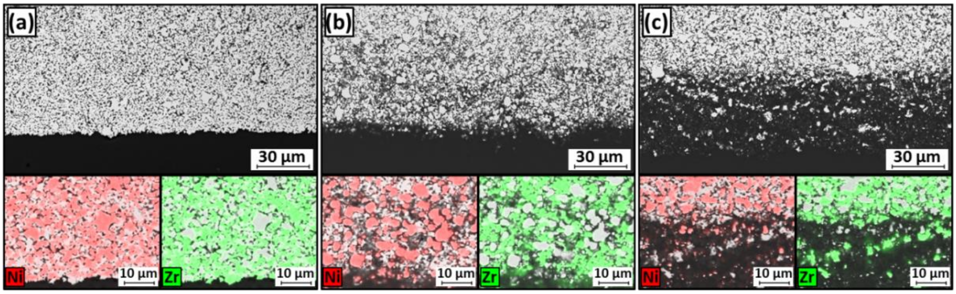

Figure 4.21: Polished cross sectional SEM images and EDX element mapping results of the cell supports, the figure labels (a), (b), and (c) are correspond with the area of 1, 2, and 3 in Figure 4.19

Figure 4.22 shows SEM images of the contacting Ni mesh between cell anode supports and interconnect. The clean Ni mesh images of Figure 4.22a were taken from area 4 in Figure 4.19 as a reference. It shows smooth surface without any secondary phase or dirt particles. In the case of the carbon covered Ni mesh (Figure 4.22b), loose carbon was removed by compressed air before SEM observation because the carbon structure was too thick to allow observation of the Ni mesh surface. The surface image shows carbon deposition and blister formation on the Ni mesh surface and the high magnification image shows distribution of tiny Ni particles, indicative of metal dusting behavior [67-69] similar as observed in the anode support. These changes are significant considering the short-term test period of 5 h. Figure 4.22c shows a cross-sectional image of single wire of the contacting Ni mesh. The image shows the delamination of the outer part of the wire as a layer which corresponds to the blisters in Figure 4.22b. The high magnification Ni EDX mapping image of single wire shows not only layered delamination but also small Ni particle detachment from wire surface.

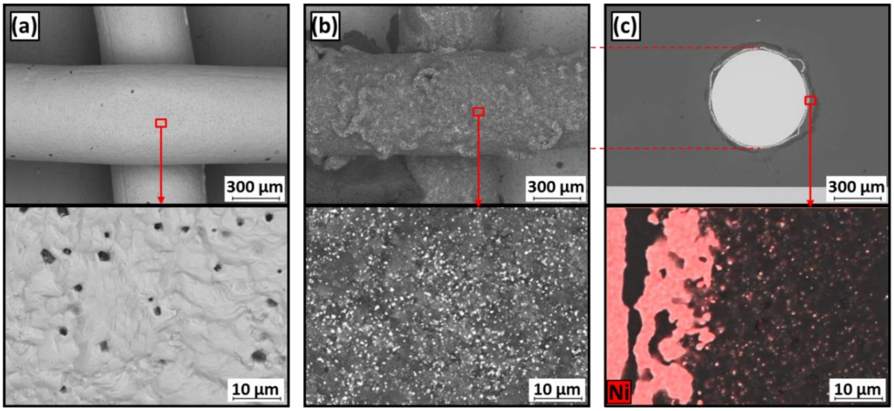

Figure 4.22: SEM images of contacting Ni mesh on the interconnect with low (upper images) and high (bottom images) magnification, the clean Ni mess image of (a) was achieved from the area 4 and carbon covered mesh images of (b) and (c) were achieved from area 5 in Figure 4.19

4.2.4. Raman spectroscopy of the cell

Raman micro-spectroscopy was applied to a fractured cell to examine the carbon deposition throughout the support and anode layers. A small piece of sample was taken from an area of Cell 2 where heavy carbon deposition had occured for the measurement as a representative sample. Figure 4.23a shows a mapping of the carbon distribution in the fractured cross-section of the cell, taken through a mesh of Raman point measurements. Carbon deposition is denoted as red color, and the brightness corresponds to the spectral intensity of the carbon signal. The result shows a high intensity of carbon deposition at the surface of the anode support and a considerable depth into the support covered with carbon, up to about 100 µm deep inside of support. There are a few points of carbon signal in the area near the anode, but not in the anode layer itself. Figure 4.23b shows SEM images of the fractured cross–section of the cell, taken from the anode layer and near the surface of the support. The anode layer shows the typical anode microstructure with clean particles, but the support shows small contaminations and fibers, which cannot be observed in the support after a test with pure H_2. However, there was no specific structure related to carbon which can be found by SEM, despite the strong carbon signal obtained by Raman from the same area. It seems that the operation time was too short to form a visible carbon structure, and carbon is only deposited on the particle surface in a thin layer. Figure 4.23c shows Raman spectroscopy result of carbon powder which was achieved from the surface of anode support and Ni mesh. The Raman result shows spectra pattern of the D band at 1350 cm^{-1}, G band at 1580 cm^{-1}, D’ band at 1620 cm^{-1}, 2D band at 2700 cm^{-1}, and D+G band at 2940 cm^{-1}. The D and D’ bands are induced by disordered carbon species such as amorphous carbon (D band) and nano-crystalline graphite (D' band), the G band on the other hand is induced by graphene or layered graphene structure (graphite, carbon nanotube, and carbon fiber) [119]. The 2D band is an overtone of the D band and D+G band is a combination of D and G bands. The Raman result indicates that the carbon grows as both ordered and disordered structure during the operation. The ordered carbon was already shown in Figure 4.20c as carbon fibers, while the disordered carbon species cannot easily be detected by SEM. It is clearly shown in the Figure 4.23c that the carbon powder from Ni mesh has more disordered structure than carbon on the support. It seems that the Ni particle size governs the carbon growth: the small Ni particles are more suitable for one directional (ordered) carbon growth like tubes and fibers, and bulk Ni wires are more suited to the growth of disordered carbon.

Table 4.2: Chemical analysis result of support material after reduction, clean-syngas test, and tar syngas test

	Carbon (wt.%)	Sulfur (wt.%)	Chlorine (wt.%)
Reduced at 900 ℃, in Ar/H_2	0.0076	< 0.0033	0.00077
After clean-syngas test	0.0175	< 0.0134	0.00067
After tar-syngas test	0.0322	< 0.0133	0.00037

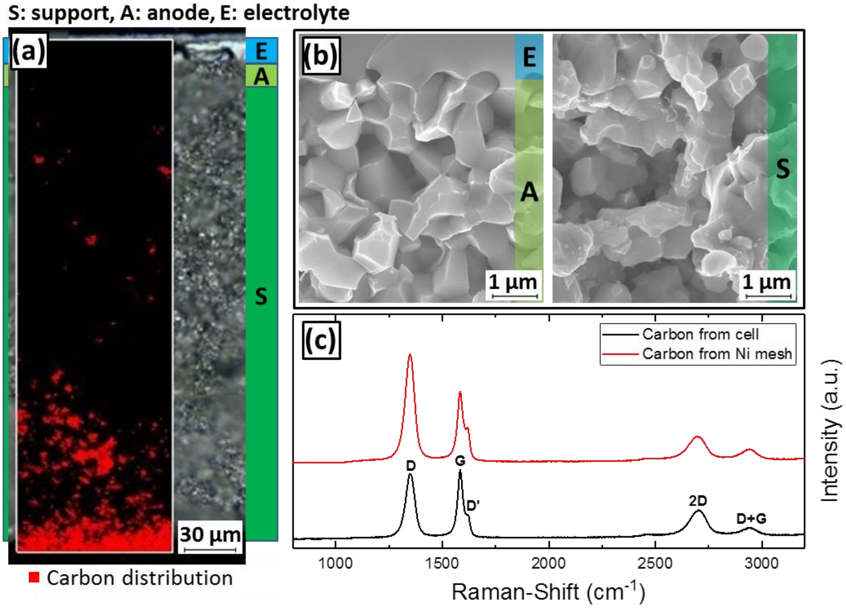

Figure 4.23: Carbon distribution mapping result of fractured cell cross-section by Raman spectroscopy (a), SEM images of fractured cell cross-section (b), and Raman shift result of carbon from cell surface and contacting Ni mesh (c)

4.3. Discussion of Ni/YSZ anode cell degradation

When tar is added to a steam-rich atmosphere like the syngas composition with 50 % steam used in this experiment, the tar undergoes steam reforming. The tar steam-reforming reaction is reported as Equation 4.2. [135-137]:

$$C_xH_yO_z + (x - z)H_2O \rightarrow xCO + \left(x + \frac{y}{2} - z\right) H_2 \qquad \text{Equation 4.2}$$

The carbon monoxide resulting from this reaction and methane (which constitutes 5 % of the base syngas) are reformed by following catalyzed reactions (Equation 4.3-4.5) [137-139]:

$$CH_4 + H_2O \rightarrow CO + 3H_2 \text{ (CH}_4\text{ steam reforming)} \qquad \text{Equation 4.3}$$

$$CH_4 + CO_2 \rightarrow 2CO + 2H_2 \text{ (CH}_4\text{ dry reforming)} \qquad \text{Equation 4.4}$$

$$CO + H_2O \rightarrow CO_2 + H_2 \text{ (water gas shift [WGS] reaction)} \qquad \text{Equation 4.5}$$

This series of reforming reactions requires enough steam, high temperature, and active catalyst material. Otherwise, CH_4 and CO are forming solid carbon by Boudouard reaction (Equation 4.6) and methane decomposition (Equation 4.7) as below.

$$2CO \rightarrow C + CO_2 \text{ (Boudouard reaction)} \qquad \text{Equation 4.6}$$

$$CH_4 \rightarrow C + 2H_2 \text{ (CH}_4\text{ decomposition)} \qquad \text{Equation 4.7}$$

From the C-H-O phase diagram (Figure 4.24), the base syngas composition is C: 9.1 %, H: 61.8 % and O: 29.1 %, which falls into a region where no carbon deposition should occur at 700 °C (in agreement with the SYN test). When the tar is added, the composition changed toward the region of the phase diagram where solid carbon is thermodynamically stable, but the total compositional changes are not significant with 8 g/Nm^3 phenol or 0.5 g/Nm^3 (which is only about ~ 0.1 % of the total fuel). However, the local composition changes right after phenol reforming can be significant in short term period. Moreover, the tar reforming reaction is endothermic (phenol: ΔH_{393K} = +1834.7 kJ/mol, naphthalene: ΔH_{393K} = +1,177.8 kJ/mol) [140] and can cause local cooling, and thus facilitate carbon deposition according to Figure 4.24. As a result, solid carbon is deposited by the reactions of Equation 4.6 and Equation 4.7 on the Ni surface and reduces the density of active sites at the TPB, which is the electrochemically active area [11-14, 64, 141]. This carbon deposition behavior could be directly related with the cell degradation.

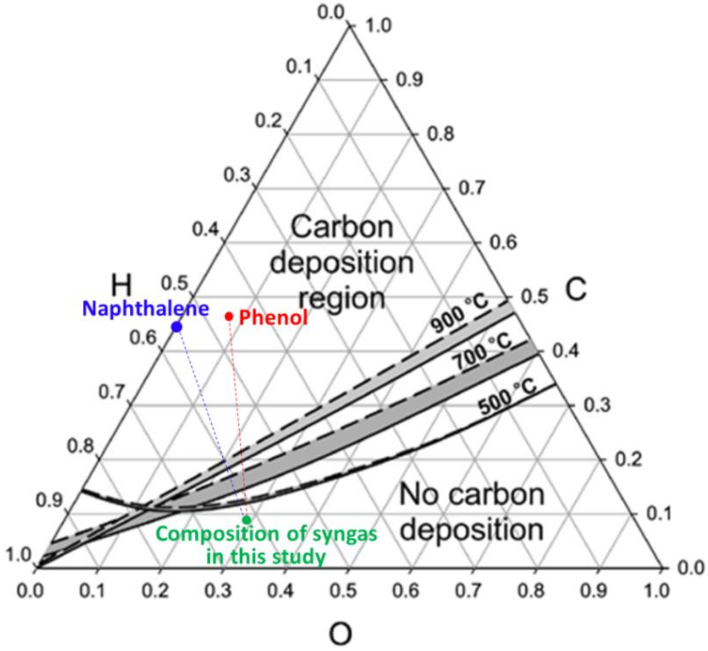

Figure 4.24: C-H-O phase diagram related to carbon deposition at the different temperatures, red dots indicate the composition of syngas in this study and phenol [142]

In the case of PHEN test, material erosion and carbon deposition is also observed without evident cell degradation. Especially the support was affected by phenol very aggressively. The fact that the erosion spreads from the fuel inlet across the cell gives rise to the assumption that the erosion is caused by a reaction involving a gas-phase reactant (in this case phenol) and the support material. The cell tests with phenol yield the following observations:

i) Erosion starts at the fuel inlet and spreads from there across the gas manifold in front of the flow field.

ii) The pronounced trenches eroded into the support imply that erosion is facilitated by an ample gas supply (flow channels without current collector wires), whereas low gas flow (flow channels with current collector wires, or the area between the Ni mesh and the Al_2O_3 housing) show significantly less erosion.

iii) Furthermore, the eroded trenches do not cover the entire support despite the long operation time. This implies that the erosion is not limited by the gas flow velocity, since a much larger volume of gas flowed through the manifold during the 250 h of operation with phenol.

iv) Carbon deposits can be found in locations between the contact points of the Ni mesh current collector across both heavily and slightly eroded areas, as we showed in [114].

v) Carbon formation was only detected close to the support surface for low amounts of phenol, whereas it was detected close to the anode as well for higher amounts of phenol.

These observations lead us to hypothesize that the erosion is caused by the decomposition of phenol, presumably via a chemical reaction catalyzed by the Ni in the support. This decomposition reaction is fast, which means that the reaction is localized at the inlet initially and the fuel is phenol-free (or that the activity of phenol is below a critical threshold value) outside of a localized reaction zone. The erosion of the cell causes a loss of catalytically active sites in the support, which slows down the phenol decomposition in the eroded support area and therefore allows the reaction zone to spread slowly across the gas manifold and finally into the flow field. Simultaneously, higher phenol concentrations cause carbon deposition closer to the anode, indicating that the support acts as a buffer to shield the anode from degradation in this case. Once the buffer is depleted (the degradation of the support sufficiently progressed), we would expect to see massive electrochemical degradation as well.

On the other hand, the NAPH test shows high voltage degradation immediately after 0.5 g/Nm^3 of naphthalene supply in to the syngas. There was no support erosion or visible change of the structure unlike PHEN test. Phenol has a hydroxy group (−OH) which causes a dipole moment in a molecule, but naphthalene has no heteroatoms like oxygen and the symmetric structure (see Figure 3.4). This different polarity of tar derives different reforming reactivity. There is a report about much slower conversion rate of naphthalene than phenol in catalytic reforming test with oxygen [143]. The slow reforming of naphthalene makes it possible to reach the anode layer before reforming. Therefore, the electrochemical reactions can be interrupted by naphthalene chemisorption on the surface of Ni in anode layer. It is also evident from the cell tests that a large part of the strong electrochemical degradation observed for naphthalene is reversible, but the recovery is much slower than the degradation. This may be interpreted as evidence that the adsorption of heavy tars on the active Ni surface (resulting in electrochemical degradation due to blocked active sites) is much faster than the tar reforming reaction or tar desorption under the investigated conditions. This hypothesis corresponds well to a report of Rostrup-Nielsen, stating that irreversible adsorption on to the Ni surface and slow reforming reactions occur for higher hydrocarbons, which is also accompanied by thermal cracking at temperature above 600-650 °C [144].

From the individual tar test of phenol and naphthalene, different cell degradation behaviors were observed with different tars. The stack test with real bio-syngas (including multiple tars) shows the support erosion and cell performance degradation which is observed in the phenol and naphthalene test. Additionally, heavy carbon deposition was found on the support surface and Ni mesh current collector. It is unclear what the reason for heavy carbon deposition is, which is not present in single cell tests with a single tar species. The possible reasons could be a complex reaction of tars, or an effect of one specific tar which is not tested in this study. Hopefully, future investigation could reveal the detailed mechanism of carbon deposition and microstructural changes of cell more clearly.

5. Cell with alternative anodes

5.1. Ni/GDC anode cell

The cell with Ni/GDC anode was chosen as the first alternative anode instead of the current standard Ni/YSZ anode. In the following sections, the manufacturing process, single cell test result, and degradation test using syngas of the Ni/GDC anode cell with contaminant are presented, and the result is discussed by comparing with the Ni/YSZ anode cell test result.

5.1.1. Ni/GDC anode cell development

5.1.1.1. Anode layer composition and thickness optimization

The cell with Ni/GDC anode was manufactured by the same process of the standard Ni/YSZ anode except Ni/GDC anode paste is used instead of Ni/YSZ anode paste. Figure 5.1 shows the cross-sectional SEM images of Ni/GDC anode half-cells with different numbers of screen printing steps: (a) single layer, (b) double layer, and (c) triple layer. The anode layer was screen-printed on the Ni/8YSZ support, and the 8YSZ electrolyte was applied on the anode. The ideal anode thickness is related to a distance of oxygen ions diffusion from electrolyte and fuel transport through the support and anode structure. If the anode is too thin, the oxygen ions will be conducted to the support structure with a less active area for catalytic reactions, thus the cell performance is not optimized. In contrast, if the anode is too thick, a concentration polarization of fuel is caused due to a lower porosity of the anode structure than in the support. Based on the described criteria, the JÜLICH ASC anode thickness was optimized at about 7 μm for Ni-YSZ operating at 700°C [145]. In Figure 5.1, a single layer has a thickness of about 5 μm and a triple layer has a thickness of about 20 μm, which both thicknesses are unsuitable in this cell design. Therefore, the double-layer anode, which has a thickness of approximately 10 μm, was used when manufacturing the Ni/GDC anode cell. The anode composition was 60 wt% for NiO and 40 wt% GDC, respectively, which was the highest performance in a previous study among the different weight ratios of 40, 50, 60, 65, and 80 % [146]. In Figure 5.1b, the GDC phase is denoted as a red color by image processing at the right-hand side of the anode layer. The image shows rather poor connectivity of GDC particles, specifically at the contact point between GDC in the anode and the electrolyte, which is not sufficient for good oxygen ion conduction. Therefore, a different anode paste composition was prepared with a NiO-to-GDC ratio of 50 wt% to improve the connectivity of the anode structure.

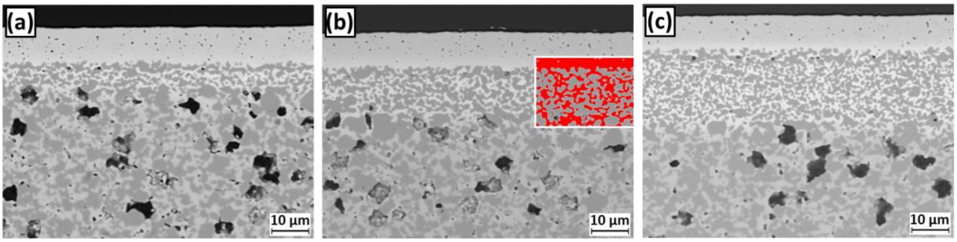

Figure 5.1: The cross-section SEM image of Ni/GDC anode half-cells with different numbers of screen printing: (a) single, (b) double, and (c) triple layer (NiO to GDC ratio: 60/40 wt%)

5.1.1.2. Cell reduction behavior

Figure 5.2a shows a cross-sectional SEM image of Ni/GDC anode half-cell with a NiO-to-GDC composition of 50 to 50 wt%. The area of the GDC phase in the anode layer was denoted as the red color again by image processing, and the connectivity of the GDC phase with an electrolyte was improved compared to the anode structure with 40 wt% GDC in Figure 5.1b. The half-cell was then reduced to analyze microstructure and gas tightness of the electrolyte that is similar to the environment of the cell during operation. Figure 5.2b is a cross-sectional SEM image of the reduced state cell after heat treatment at 900 °C for 3 h in 2.9 % H_2/Ar atmosphere. The reduced state of the anode and the support shows more pores in the structure than in the oxidized state due to the volume change by the reduction of NiO to the Ni metal phase. Figure 5.2c shows the oxidized half-cell picture of the electrolyte side. The green color appears as green NiO in the Ni/GDC anode since the thin YSZ electrolyte is transparent after sintering. Figure 5.2d shows the picture of the half-cell after reduction, which is a brown color and the cell is bent. Since the YSZ is stable in the reducing atmosphere used, the Ni/YSZ anode cell shows gray in color after reduction due to the color of Ni metal. In the case of the Ni/GDC anode, GDC is reduced in low oxygen partial pressure [147]. Therefore, the brown color material suggests a new phase formation in anode and electrolyte layers during cell sintering or reducing by interactions of the NiO, GDC, and YSZ phases.

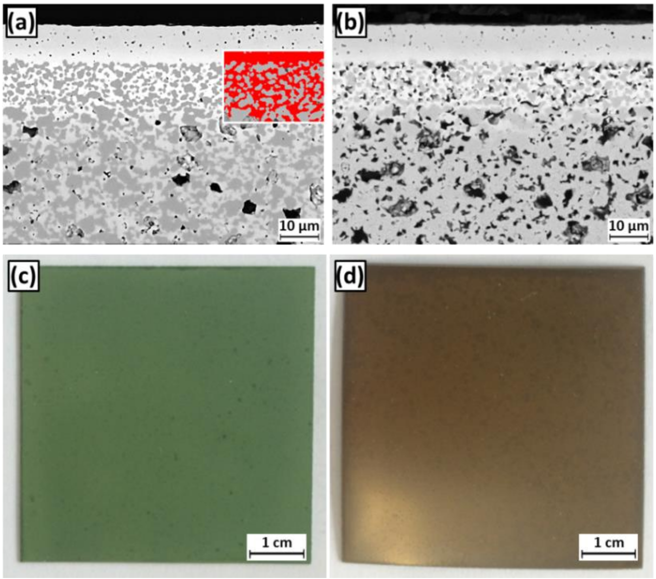

Figure 5.2: Cross-sectional SEM image of Ni/GDC anode half-cell with 50 to 50 composition (a) oxidized and (b) reduced state, and the picture of the cell (c) oxidized and (d) reduced state

5.1.1.3. Half-cell leakage rate test

The electrolyte gas tightness of half-cells was measured for both oxidized and reduced states, and the test results are presented in Table 5.1. The oxidized state of the cell shows a lower leakage rate than the internally determined maximum leakages of the oxidized state cell, and the leakages are 8×10^{-6} for air and 2×10^{-5} $hPa \cdot dm^3 \cdot s^{-1} \cdot cm^{-2}$ for He. The test result shows a lower leakage rate than the limit in both the air and He tests. After reduction, the leakage rate was increased by the pore formation in the anode layer, but the values were still appropriate for the cell operation.

Table 5.1: Leakage test result of Ni/GDC half-cell

	Leakage test ($hPa \cdot dm^3 \cdot s^{-1} \cdot cm^{-2}$)	
	Air	He
Oxidized state	2.53×10^{-6}	4.19×10^{-6}
Reduced state	4.56×10^{-4}	1.72×10^{-4}

5.1.2. YSZ-GDC inter-diffusion*

5.1.2.1. Inter-diffusion between Ni/GDC anode and YSZ electrolyte

As mentioned in Section 5.1.1.2, the Ni/GDC anode cell shows unexpected reduction behavior (cell deformation and brown colored anode) suggesting a chemical reaction or phase transformation in the anode or electrolyte layer. Figure 5.3 shows the XRD phase analysis result of the Ni/GDC anode layer on the Ni/YSZ support after different heat treatments as printed layers (drying in an oven at 60 °C for 2 h) after calcination at 1000 °C for 1 h and after sintering at 1400 °C for 5 h. The XRD result of the as-printed anode layer shows two main phases of NiO and GDC, and the YSZ phase was also detected with low intensity from the support. After the calcination, which done at a relatively low temperature of 1000 °C, there were no phase changes from the XRD result of the as-printed layer. However, in the case of the Ni/GDC anode after sintering, the GDC phase completely disappeared and a new phase appeared between the YSZ and GDC peak positions. It seems that the GDC phase transformed to a new phase by reacting with another material. Since the XRD result of the anode after sintering does not show any changes of NiO, the YSZ-GDC interaction was estimated. Moreover, both YSZ and GDC have similar cubic fluorite structures, so there is no miscibility gap [148-150]. Several results of cerium gadolinium yttrium zirconium oxide in the XRD database such as $Ce_{0.72}Gd_{0.18}Y_{0.016}Zr_{0.092}O_{1.938}$ (brown color) or $Ce_{0.256}Gd_{0.64}Y_{0.01}Zr_{0.776}O_{3.704}$ (yellow color) phases were matched with new phases in Figure 5.3 [151], but there was no identical reference result. This is expected since complete miscibility of the two parent phases means that there is a very small chance of forming a phase of the exact same stoichiometry as the reference patterns in the database.

---

* This subchapter has been published in the “Journal of the American Ceramic Society”, Volume 101, Issue 2, p. 739-748, 05 September 2017

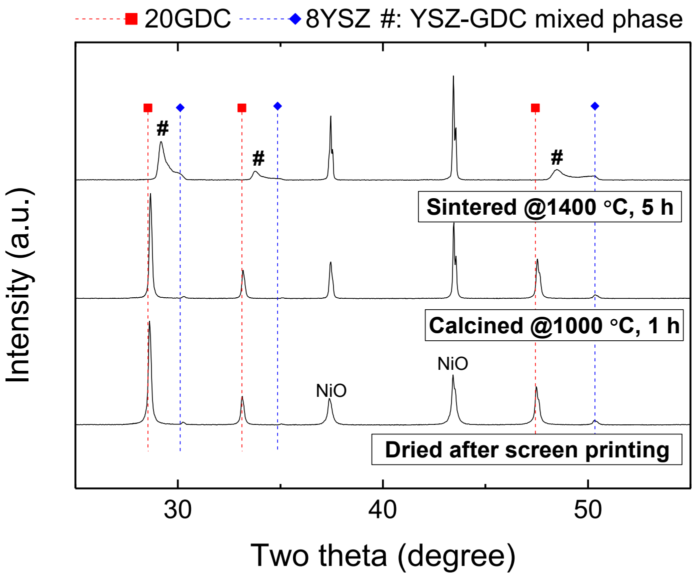

Figure 5.3: XRD result of the Ni/GDC anode layer on the Ni/GDC support

An EDX measurement was applied to the polished cross-section of the half-cell to analyze diffusion behaviors of YSZ and GDC materials. Figure 5.4 shows the point EDX result and the SEM image with different measurement positions from the support to the electrolyte, which is basically the same as a line scan. Since the NiO does not show any phase transformation in Figure 5.3, the results are presented as a relative ratio between four elements—zirconium (Zr), yttrium (Y), cerium (Ce), and gadolinium (Gd). Also, the EDX result shows more active diffusion of Ce and Gd than Zr and Y at both electrolyte-anode and anode-support interfaces. For example, the nearest spectrum in electrolyte to anode (spectrum 3) shows about 30 % of Ce and of 15 % Gd, on the other hand, the nearest spectrum in anode to electrolyte (spectrum 4) shows about 20 % of Zr and of 5 % Y. However, Zr is diffused throughout the anode layer by 10 % even in the center position of the anode layer (spectra 6 and 7). This result supports the XRD result in Figure 5.3, suggesting YSZ and GDC interactions during high-temperature sintering and mixed phase formation in both electrolyte and anode layers.

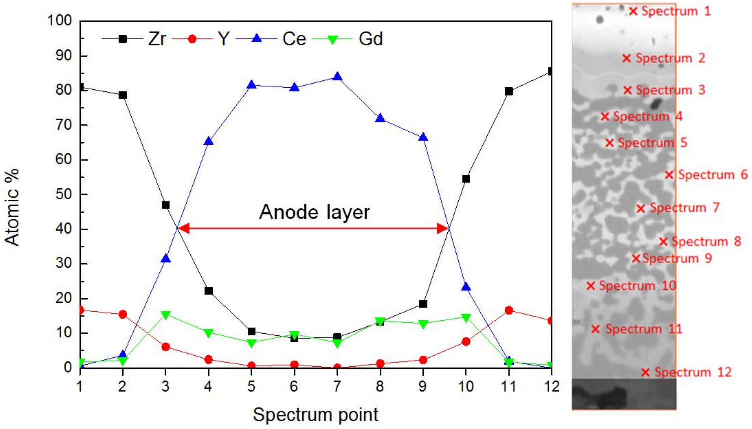

Figure 5.4: Point EDX result of the Ni/GDC half-cell after sintering and SEM image with different measurement position

5.1.2.2. Interaction study of YSZ and GDC phase with raw powders

For the systematic analysis of the interaction between YSZ and GDC phases, the raw powder mixtures of NiO, YSZ, and GDC were prepared and analyzed after sintering at different temperatures, and Table 5.2 shows the pellet pictures after sintering and apparent volume change by reduction. All of the YSZ-GDC pellets show the same white color in oxidized state. However, the color was changed after reduction at the pellet surface which is sintered at 1100 ℃ and the entire pellets which is sintered at 1200, 1300, and 1400 ℃. In contrast, all NiO-YSZ-GDC pellets show green color (the color of NiO) with different brightness according to the different density of pellets. After reducing heat treatment, the pellets show gray color by reduction of NiO to Ni. In both cases of YSZ-GDC and NiO-YSZ-GDC pellets, the apparent volume was expanded by reduction when the pellets were sintered above 1200 ℃.

Table 5.2: NiO-YSZ-GDC and YSZ-GDC pellet pictures after sintering and apparent volume change by reduction

Sintering Temp.	YSZ-GDC mixture			NiO-YSZ-GDC mixture		
	Oxidized state	Reduced state	ΔV (%)	Oxidized state	Reduced state	ΔV (%)
1000			-0.3		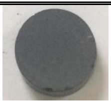	-0.6
1100		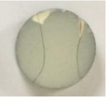	-0.6			0.2
1200			0.1			1.0
1300			1.3		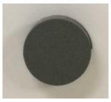	2.2
1400			1.5		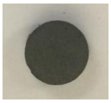	1.7

Figure 5.5 shows the XRD results of the YSZ-GDC and NiO-YSZ-GDC pellets after sintering with different temperatures and after reduction. In the case of the YSZ-GDC mixture (Figure 5.5a), there was no interdiffusion after sintering at 1000 °C, but after sintering at 1100 °C, the YSZ-GDC mixed phase appeared. The peak of the mixed phase was more identical after higher temperature sintering. The YSZ and GDC phases were completely transformed to the mixed phase after sintering at 1300 °C. The relative phase content of the YSZ-GDC mixed phase was calculated by the Rietveld refinement method as 16 % and 27 % for the result after sintering at 1100 °C and 1200 °C, respectively [150]. After reducing at 900 °C for 5 h in 2.9 % H_2/Ar, the XRD results of the non-reacted YSZ and GDC phases, sintered at low temperature, show the same pattern and position as the oxidized state. In contrast, the YSZ-GDC mixed phase shows a peak shift to a lower angle. From Bragg's law (Equation 5.1),

$$2d \sin\theta = n\lambda$$ Equation 5.1

the scattering angle (θ) decrement indicates the lattice inter-planar distance (d) increment, causing a chemical volume expansion of the material that seems related with the cell deformation in Figure 5.2d. This chemical expansion can be explained by the increased repulsive force (electrostatic force) between cations by the loss of oxygen anions. As mentioned in section 5.1.1.2, GDC also shows reducing behavior under low oxygen partial pressure with high temperature [147]. The apparent volume and sample color change of the YSZ-GDC mixture in Table 5.2 also correspond with the XRD results. The color change was observed from the pellets including the mixed phase that was sintered above 1100 °C, and the higher relative phase content of the mixed phase causes a more apparent volume expansion.

The result of the NiO-YSZ-GDC mixture (Figure 5.5b) shows the same trend as the YSZ-GDC mixture without any reaction directly related with the NiO:YSZ-GDC mixed phase formation and chemical expansion by reduction. However, there was a strong influence of the NiO to the mixed phase formation. The presence of NiO accelerates the inter-diffusion kinetics of GDC and YSZ, resulting in a higher ratio of the mixed phase formation at lower temperatures compared to the YSZ-GDC mixture. The result of the relative phase content of the mixed phase shows 39 % and 78 % for the result after sintering at 1100 °C and 1200 °C, respectively [150], without the NiO peak in the calculation of the Rietveld refinement method. Also, it seems that the grain boundary mobility and grain growth kinetics of 8YSZ is changed by the presence of NiO [152, 153].

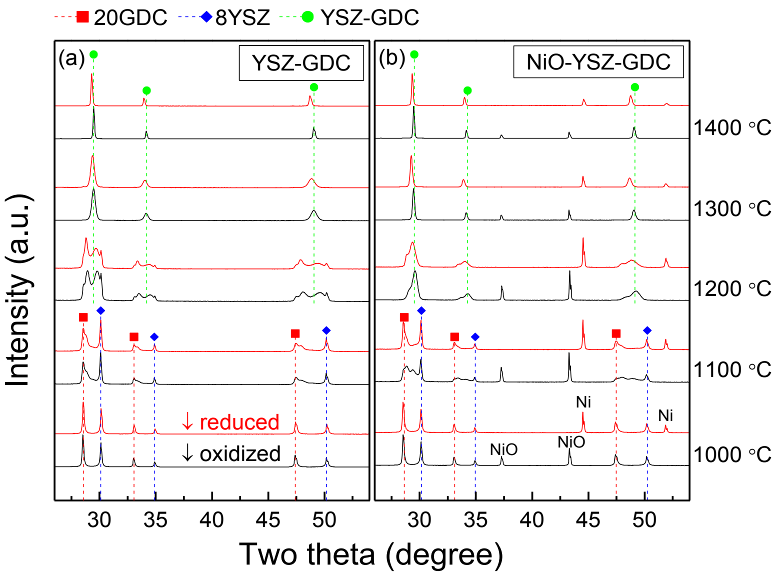

Figure 5.5: XRD result of the YSZ-GDC (a) and NiO-YSZ-GDC (b) powder mixtures after sintering at different temperatures of 1000, 1100, 1200, 1300, and 1400 °C; the red line shows the XRD result after reducing at 900 °C for 5 h in 2.9 % H_2/Ar

5.1.2.3. TGA analysis of GDC and YSZ-GDC mixed phased

As shown in Section 5.1.2.2, the XRD results indirectly imply reduction behavior of the YSZ-GDC mixed phase. To clarify the reduction behavior and to quantify the oxygen loss during reduction, thermo-gravimetric analysis (TGA) was applied. The YSZ-GDC powder mixture and GDC raw powder were sintered at 1400 °C for 5 h and ground to a powder to increase the surface area of the sample. Before the TGA, the samples were heated up to 1100 °C in the air to remove residual organics and impurities. The temperature was then fixed at 900 °C and the atmosphere was switched from air to Ar/H_2 for the reduction of the sample. After 5 h of reduction, the sample was re-oxidized by switching the atmosphere from Ar/H_2 to air again. The redox cycle was performed every 50 ℃ at a lowered temperature until the temperature decreased to 750 ℃. Figure 5.6 shows the TGA curves for the 20GDC and YSZ-GDC mixed phases. The results show weight loss in the Ar/H_2 atmosphere due to the oxygen loss from the GDC and YSZ-GDC mixed phase, proving the reducing behavior of the YSZ-GDC mixed phase. The reducibility of the Ce^{4+} ion to the Ce^{3+} can be calculated as nonstoichiometry δ for each compound of the GDC and YSZ-GDC mixed phases. Since δ is achieved by measuring the weight loss, the concentration of Ce^{3+} (Ce'_{Ce} in Kröger-Vink notation) ion can be calculated using Equation 5.2. In the calculation, the oxygen was considered as the only volatile species in the GDC and YSZ-GDC mixed structures. The calculation results of the Ce^{3+} ion concentration at 900 °C shows 37 and 35.5 % in the GDC and YSZ-GDC mixed phases, respectively [150]. These results show a similar reducibility of Ce^{4+} in the YSZ-GDC mixed phase as in the GDC phase.

$$2[V_O^{\bullet\bullet}] = [Ce'_{Ce}] \qquad \text{Equation 5.2}$$

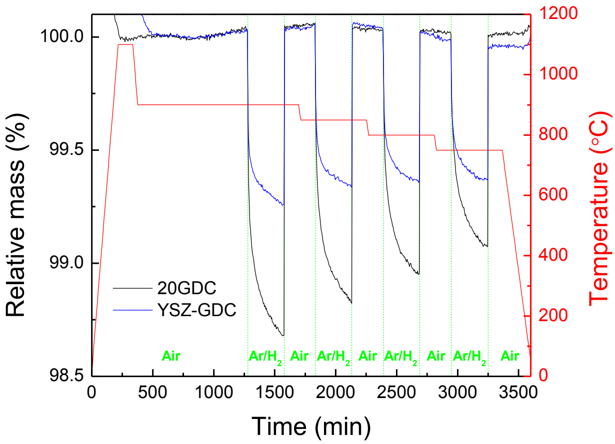

Figure 5.6: TGA analysis of the reduction in GDC (black line) and a GDC–YSZ mixed phase sintered at 1400°C (blue line); the dotted green lines indicate a change in the gas atmosphere [150]

5.1.2.4. Electrical properties of YSZ-GDC mixed phase

Figure 5.7 shows the conductivities of YSZ, GDC, and YSZ-GDC mixed phases as function of temperature in oxidized and reduced states. Literature indicates that when the YSZ and GDC form a mixed phase, the conductivity is decreased compared to the single phases due to lattice distortion [148, 149, 151]. The experimental results also show a lower conductivity of the YSZ-GDC mixed phase than both the conductivities of the YSZ and GDC single phases. In the reduced state, the conductivity of YSZ was not changed by reduction, but the conductivities of the GDC and YSZ-GDC mixed phases increased. The conductivity increased by the reduction of the Ce^{4+} ion to the Ce^{3+} ion, yielding electron charge carriers in the material [151]. Table 5.3 shows the conductivity values at 700 °C and the calculated activation energy in the oxidized and reduced states. In the oxidized state, the conductivity of YSZ is about 7.4 times higher and the activation energy is slightly lower than the YSZ-GDC mixed phase. In the reduced state, the conductivity of YSZ is 1.4 times higher, but the activation energy is also higher than in the mixed phase. The activation energy of the mixed phase was lowed after reduction due to the electronic conduction (electrons are more mobile than oxygen vacancies).

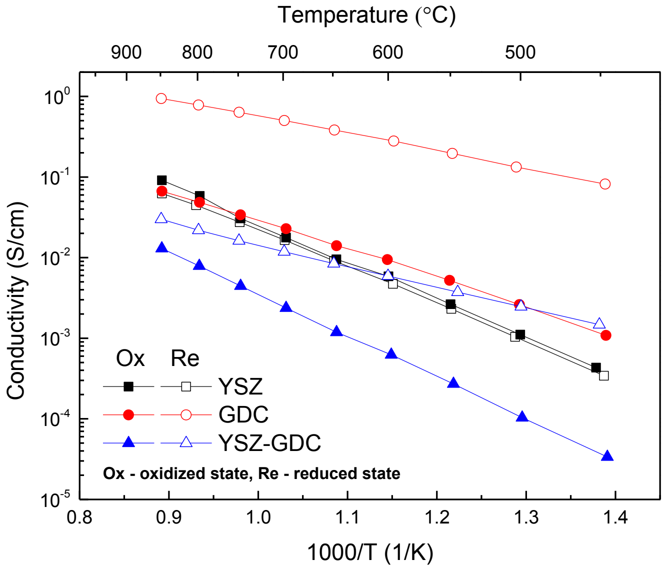

Figure 5.7: Temperature-conductivity plot of YSZ (black), GDC (red), and YSZ-GDC (blue) phases; the conductivities were measured in both oxidized (closed symbol) and reduced (open symbol) state [150]

Table 5.3 Conductivity and activation energy of YSZ, GDC, and YSZ-GDC phases in the oxidized and reduced states

	Oxidized		Reduced	
	σ @700 °C (S/cm)	E_a (eV)	σ @700 °C (S/cm)	E_a (eV)
YSZ	0.0177	0.94	0.0165	0.91
GDC	0.0229	0.71	0.5021	0.43
YSZ-GDC	0.0024	1.03	0.0118	0.52

5.1.3. Ni/GDC cell test result (KIT)

5.1.3.1. Cell performance with single cell measurement

Figure 5.8 shows the microstructure of a Ni/GDC full-cell and the schematic diagram of the phase composition for each layer according to the inter-diffusion studies in Section 5.1.2. The GDC phase in anode layer reacts with the YSZ phase of the electrolyte and the substrate; thus, the YSZ-GDC mixed phase was formed in the anode and the electrolyte layer. Also, the electrolyte shows the different concentration of Ce ion according to the distance from the anode layer.

Figure 5.9 shows the single cell measurement result for the Ni/GDC anode cell, and the cell was measured at 820 °C in hydrogen fuel and laboratory air. A standard Ni/YSZ anode cell was also measured under the same conditions to compare the results to each other, and the dotted blue lines in Figure 5.9 indicate the current density of Ni/YSZ and Ni/GDC anode cell at the voltage of 0.8 V. The result shows less than half of the current density of the Ni/GDC anode cell compared to the Ni/YSZ anode cell. There are several reasons for this low performance with Ni/GDC anode that are related to the YSZ-GDC mixed phase formation. First, due to the mixed phase formation, the ionic conductivity decreased in the anode and the electrolyte. Another reason for the low performance is the agglomeration of the NiO particles in the anode layer near the electrolyte, as shown in Figure 5.8. As described in section 5.1.2, at the intersection of the anode and the electrolyte, the diffusion of GDC in the anode is more rapid than YSZ in the electrolyte during the sintering of the electrolyte. This different diffusion velocity forms Kirkendall pores at the anode/electrolyte interface that reduces the contact area and weakens the adhesion. Moreover, NiO particles in the anode near the electrolyte are easily agglomerated by the loss of the GDC particle. The coarsened Ni causes less surface area and blocks the ion conduction from the electrolyte to the anode.

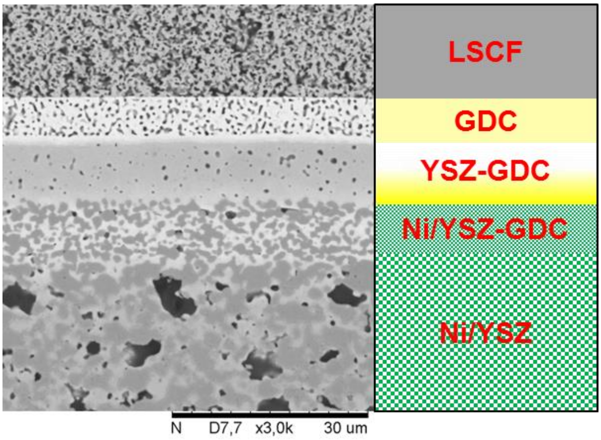

Figure 5.8: Microstructure and schematic diagram of the Ni/GDC anode full-cell

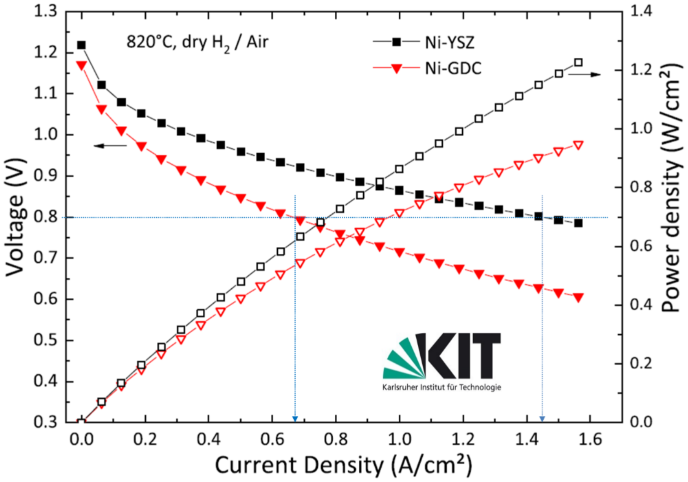

Figure 5.9: Single cell measurement result of the Ni/GDC anode cell (Measured at KIT IAM-WET by N. Russner) [150]

5.1.3.2. Ni/GDC anode cell test results with syngas containing impurities (TU Munich)

The Ni/GDC anode cell was tested with phenol, naphthalene, and sulfur-containing syngas and the results are presented in Figure 5.10. The initial cell voltages for all Ni/GDC cell test results were about 0.1 V lower than Ni/YSZ anode cell at 700 ℃ with simulated syngas, as described in 4.2.3.1.

In the case of the phenol test (Figure 5.10a), the result shows no electrochemical response by 2 g/Nm^3, which is similar to the Ni/YSZ anode cell test result with 2 g/Nm^3 phenol (Figure 4.2a). The average degradation rate during the total operation time of 450 h was about 4 %/1000 h, but the cell voltage degradation during the phenol test was lower than the average value since the cell shows higher degradation at the beginning of the test with syngas. In another test, the phenol content was increased stepwise from 1 g/Nm^3 to 8 g/Nm^3 (Figure 5.10b), which is similar to the test with Ni/YSZ anode (Figure 4.2b). The average degradation rate was about 3.3 %/1000 h, showing again no electrochemical response. When a phenol concentration of 8 g/Nm^3 was applied, the voltage shows larger scale fluctuations than the test with a phenol content of fewer than 4 g/Nm^3, but the voltage does not show distinct degradation. Similar to the Ni/YSZ anode cell test result, there was no additional effect of phenol on the cell performance in this test period.

Figure 5.10c shows the Ni/GDC anode cell test result with naphthalene, and the voltage dropped right after the naphthalene introduction. The degradation rate of the Ni/GDC anode was double the degradation rate of Ni/YSZ anode cell, showing the second stage of degradation with an even higher rate than the Ni/GDC anode the first degradation. Although the voltage reached a steady state after about 50 h, the voltage drop was about 0.23 V from the initial value, and this decrease is much higher than the voltage drop of the Ni/YSZ anode cell test that was about 0.14 V. The voltage was recovered after the naphthalene test up to about 0.65 V during the 30-h operation with syngas, but about 0.07 V of voltage was irreversibly degraded.

As shown in Figure 5.10d, the voltage of Ni/GDC anode cell drastically drops by the addition of 5 ppm of H_2S. Also, the degradation rate of Ni/GDC was almost the same as the degradation rate of the Ni/YSZ anode cell test result with H_2S in Figure 4.12. Since the time of H_2S supply was 2 h, which is shorter than Ni/YSZ cell test, the voltage dropped off about 0.08 V. After the test, the voltage recovered during syngas operation, and the voltage increased about 0.01 V once again with dry H_2. However, the irreversible degradation of Ni/GDC anode (0.06 V) was higher than that for the Ni/YSZ anode (0.04 V).

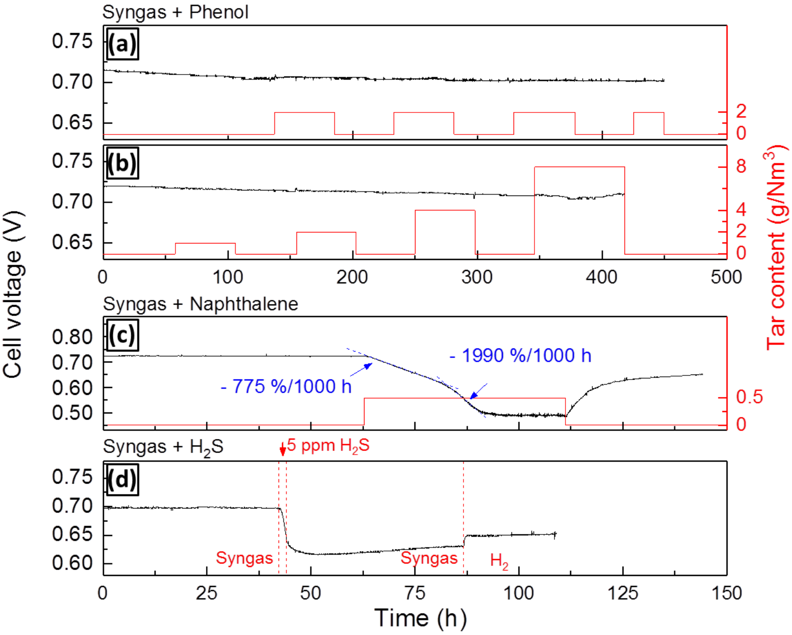

Figure 5.10: Ni/GDC anode cell single measurement result with syngas + phenol (a and b), syngas +naphthalene (c), and syngas + H_2S (d) at 700 °C, 0.34 A/cm^2

5.1.3.3. Post-test analysis

Figure 5.11 shows the optical images and SEM micrographs of the Ni/GDC anode cell support after the phenol test. The images of support after the phenol test (Figure 5.11a and b) show similar support erosion as that already shown in section 4.1.2.3, but with different pattern. Since the erosion pattern is mainly related to fuel gas flow, the difference in the shape of erosion is estimated as the result of replaced contacting materials and different connections to the support. However, the general trend was the same as that for the Ni/YSZ anode cell, showing dusting with carbon deposition near the inlet area. Additionally, the cells show cracks and re-oxidation without cell performance change. Therefore, the cracks are assumed to occur while cooling down after the cell test. The SEM images show the same trend as the previous test with the Ni/YSZ anode cell. The SEM images of the inlet surface (Figure 5.11c and d), where the erosion appeared, show structure changes including connectivity loss between particles and carbon fiber formation. In the case of fractured cross-section images (Figure 5.11e - h), there were no visible changes in the anode layer, but numerous carbon fibers were observed from the inside of support. Also, the effect of phenol, which is limited in the support layer, has already been discussed. Therefore, the Ni/GDC anode cell shows the same result as the Ni/YSZ anode cell since the support materials were the same for both types of cells.

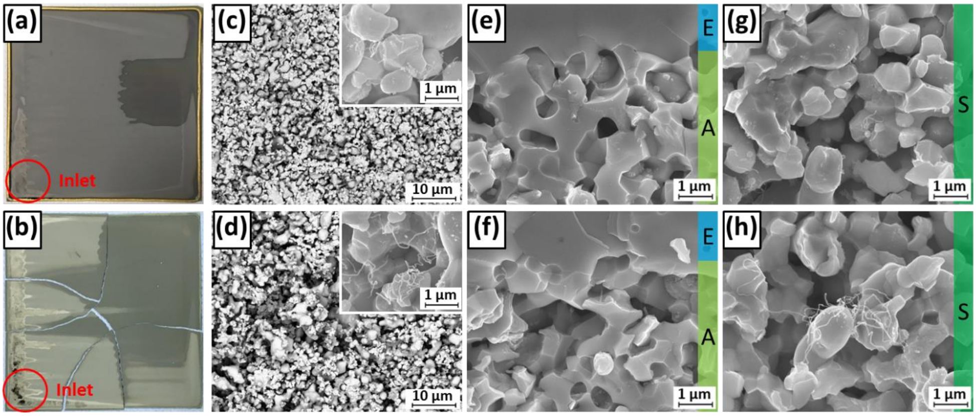

Figure 5.11: Support photo, surface, and fractured cross-section SEM images of the support inlet after the 2g/Nm^3 phenol test (a-d) and the 1-8 g/Nm^3 phenol test (e-h)

Similarly, the cell after the naphthalene test was investigated, as shown in Figure 5.12. There were no macro-scale structure changes on the support similar to the test with the Ni/YSZ cell (Figure 4.9). A crack and re-oxidation were also observed, which is the same as other cells after the test. The fractured cross-section SEM image shows small particles that are estimated as carbon-based structures and carbon fibers, and these fibers are very rare in the structure. The small particles need to be further analyzed to identify their structure and composition with more delicate tools such as TEM.

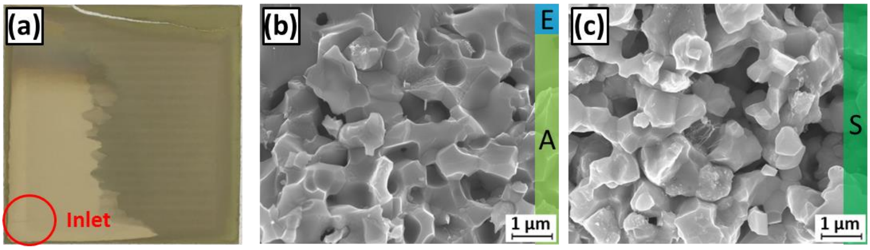

Figure 5.12: Support photo and fractured cross-section SEM images after of support inlet 0.5 g/Nm^3 naphthalene test

Since the SEM, XRD, and Raman tests could not detect sulfur species after the cell test with the Ni/YSZ cell in the previous section, the investigation of the Ni/GDC anode cell with SEM after the H_2S test also could not find any distinct change, as shown in Figure 5.13.

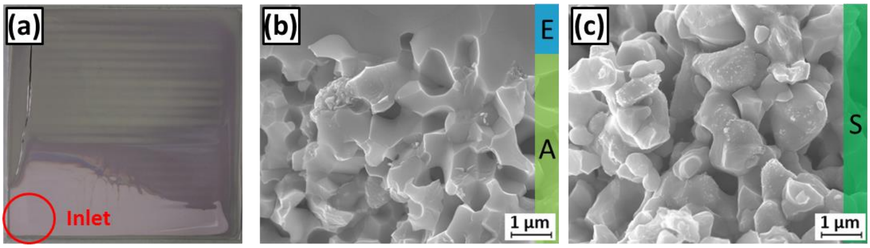

Figure 5.13: Support photo and fractured cross-section SEM images of the support inlet after the 5 ppm H_2S test

5.1.4. Discussion of the Ni/GDC anode cell test results

By using GDC instead of YSZ in the anode, the increase of both ionic and electronic conductivity was expected. However, a YSZ-GDC mixed phase was formed in the anode and electrolyte during the high-temperature sintering step, which is necessary to densify the electrolyte. The YSZ-GDC mixed phase shows lower ionic conductivity than both the YSZ and GDC single phases. Moreover, the different diffusion coefficients of Y^{3+}, Zr^{4+}, Gd^{3+}, and Ce^{4+} induces pore formation during sintering and Ni particle coarsening in the anode layer. Although the mixed phase shows increased electronic conductivity after reduction, the cell performance of the Ni/GDC anode cell with dry hydrogen shows about half of the standard Ni/YSZ anode cell performance at 820 °C and 0.8 V. Despite this poor performance of the Ni/GDC anode cell, the poisoning test was carried out and compared with the Ni/YSZ anode cell results.

From the phenol test, stable operation was observed, and this result is similar as for the test with the Ni/YSZ anode cell. As discussed in Section 4.3, phenol seems to be reformed in the support and degradation was mainly observed in support material such as erosion and carbon deposition. In the test of the Ni/GDC anode cell, 2 g/m^3 phenol seems not to affect the electrochemical reaction at the anode layer due to the pre-reforming of phenol in the support. The support material was the same for the Ni/YSZ and Ni/GDC anode cells (Ni/3YSZ), leading to the expectation of having the same chemical reforming process in both supports.

In the naphthalene test, the Ni/GDC anode cell shows about double the degradation rate at the beginning of the test than the Ni/YSZ anode cell. The primary degradation mechanism is considered as the effect of the catalytically active area such as the TPB reduction by naphthalene chemisorption and carbon deposition. The Ni/GDC anode cell has initially less TPB due to the different microstructure by the YSZ-GDC mixed phase formation. Therefore, the effect of naphthalene in the anode layer can be more pronounced with the same amount of TPB loss. Moreover, the anode has a lower ionic conductivity that interrupts the oxygen ion supply. The lower ionic conductivity causes the slowdown of the CO utilization (Equation 5.3) and favors carbon deposition by the Boudouard reaction (Equation 4.6).

$$\mathrm{CO} + \mathrm{O}^{2-} \rightarrow \mathrm{CO}_2 + 2e^- \qquad \text{Equation 5.3}$$

The sulfur poisoning in this test temperature and H_2S content is mainly induced by sulfur chemisorption on the Ni surface. In general, the performance degradation rate of the Ni/GDC anode cell was similar to the Ni/YSZ cell. However, when the H_2S supply was stopped, the Ni/GDC anode cell performance was recovered much slower than the Ni/YSZ anode cell. Also, the poor ionic conductivity of the YSZ-GDC mixed phase can be the major reason for the slow voltage recovery by interrupting oxygen ion delivery.

Overall, the degradation mechanisms of Ni/GDC anodes are similar to Ni/YSZ anodes, but the degradation mechanisms are more pronounced.

5.2. Anode material with Mo incorporation

In this section, the study of Mo incorporation into the anode layer is described, and this incorporation produces the second alternative anode material. Various cell manufacturing processes with Mo-containing precursors have been tried in ASC and ESC design, and the microstructure and composition of cells analyzed. The cells have been tested with sulfur-containing fuel and the results are summarized and discussed.

5.2.1. ASC type cell development

5.2.1.1. Mo containing anodes and thermal stability of precursor material

The main challenge of Mo incorporation into the anode layer was preventing Mo evaporation during the sintering of the electrolyte. The ASC cell needs a high-temperature sintering to have a gas-tight electrolyte structure (in our manufacturing process, the sintering temperature is 1400 ˚C) [154]. Table 5.4 shows several studies of Mo-containing SOFC anode with their precursor and anode processing method. All the Mo precursors in the list have lower melting points than the electrolyte sintering temperature of 1400 ˚C; therefore, the anode was applied to the ESC that does not need high-temperature sintering or infiltration to the ASC after sintering of the electrolyte. The performance of ESCs are normally lower than ASCs due to the thick electrolyte, and ESCs do not have an anode support structure that has the function of the pre-reformer for tar and sulfur species. In the case of infiltration into ASCs, it has thick support and low porosity in the oxidized state, so it is difficult to achieve a sufficient amount of Mo content in the anode layer by infiltration. Therefore, the other Mo containing precursors are surveyed from the literature that has a high-temperature stability. Some candidates of Mo source material are Mo-doped CeO_2 (CMO) and Mo-Gd co-doped CeO_2 (CMGO), and it has been reported that the CMO and CMGO have higher ionic conductivities than GDC [155, 156]. Moreover, CMO shows Mo precipitation after reduction with dry hydrogen [155], so various anode compositions can be achieved with CMOs such as Ni/CMO, Ni-Mo/CMO, and Ni/MoO_2-CMO. Several results have already been reported about high tolerance to sulfur poisoning and carbon deposition with CMO [91, 157, 158].

Table 5.4: Several studies of SOFC anode materials including Mo

Mo-Precursor	Melting point	Cell Type	Method	Result	Ref.
MoS_2	1185 ℃	Button ESC	SP$^{(a)}$	High sulfur tolerant, 75mW/cm^2 @ 900 °C	[159]
MoO_2	1100 ℃	Button ESC	ES$^{(b)}$	Direct gasoline-fed 30 mW/cm^2	[160]
$(NH_4)_6Mo_7O_{24} \cdot 4H_2O$	MoO_3: 795 ℃, NiMoO4: 1310 ℃	Button ESC	SP	10 h stability	[91]
		Planar ASC	I$^{(c)}$	120 h stability under CH_4+H_2S	[93]
$Ce_{1-x}Mo_xO_{2+\delta}$	unknown	Planar ESC	I	Increased sulfur tolerant by CMO infiltration	[157]
		Planar ASC	I	Increased sulfur tolerant, stable under CH_4 ~200 h	[158]

(a): Screen printing, (b): Electrostatic spray, (c): Infiltration

The thermal stability of CMO and CGMO were analyzed by thermo-gravimetric analysis together with MoO_3 and $NiMoO_4$ precursors, as shown in Figure 5.14. The MoO_3 and $NiMoO_4$ show weight loss from 800 °C and 1250 °C, and these temperatures are approximately their melting points, which are already known. The $Ce_{0.9}Mo_{0.1}O_{2+\delta}$ result shows continuous weight loss about 0.5 % until the temperature of 1000 °C, and then it starts to lose the mass again with a higher percentage at about 1150 °C that indicates the instability of material. Therefore, the CMO was determined to be an unstable precursor at the sintering temperature of ASCs. In the case of $Ce_{0.8}Mo_{0.1}Gd_{0.1}O_{2+\delta}$, it shows weight increase while heating up until the temperature about 1200 °C, and the weight then again until the temperature of 1400 °C, which was the end of the measurement. However, the mass change was smaller than the 1 % range, so that it is difficult to estimate its thermal stability.

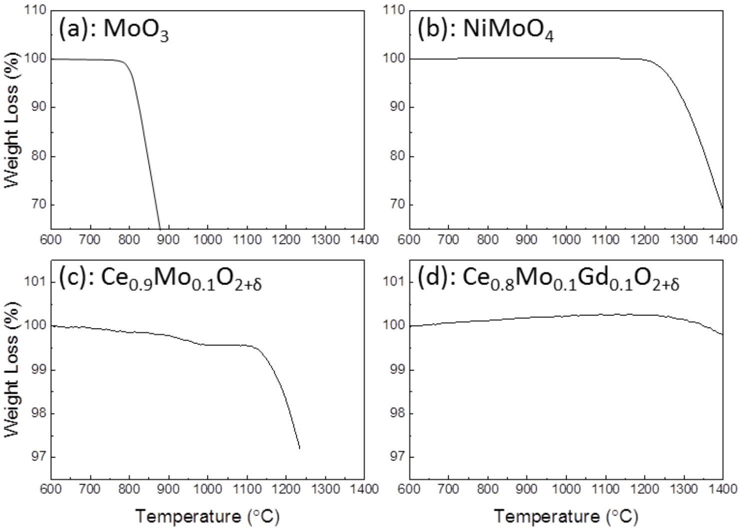

Figure 5.14: TGA result of Mo precursor: MoO_3 (a), $NiMoO_4$ (b), $Ce_{0.9}Mo_{0.1}O_{2+\delta}$ (c), and $Ce_{0.8}Mo_{0.1}Gd_{0.1}O_{2+\delta}$ (d)

5.2.1.2. Mo incorporation with the screen printing method

A conventional screen printing method was used to manufacture the cell with the Mo-containing anode. In Section 5.2.1.1, only CMGO precursor shows stability at the electrolyte sintering temperature of 1400 ℃. The half-cell was manufactured with the Ni/CMGO anode by the conventional screen printing process. Figure 5.15 shows the Ni/$Ce_{0.8}Mo_{0.1}Gd_{0.1}O_{2+\delta}$ anode after sintering at 1400 ℃ for 5 h. The electrolyte was applied before sintering, but it delaminated from the cell. The remaining anode layer shows high porosity and a high ratio of NiO that appears as a darker phase in the SEM image. It seems the CMGO phase was also not stable and diffused out of the anode structure or evaporated. Therefore, another composition of CMGO with lower Mo content was prepared. Figure 5.15b shows the cross-sectional SEM image of the Ni/$Ce_{0.85}Mo_{0.05}Gd_{0.1}O_{2+\delta}$ anode half-cell. Although the electrolyte was not delaminated after sintering, unlike the NiO/$Ce_{0.8}Mo_{0.1}Gd_{0.1}O_{2+\delta}$ anode, the electrolyte was not dense and the anode lost most of its Mo. This result shows that the CMGO, even with low amounts of Mo doping, is an unsuitable anode precursor material due to the poor thermal stability or high reactivity with the YSZ electrolyte material.

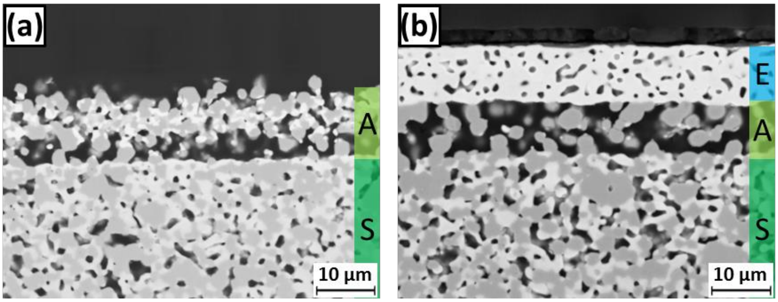

Figure 5.15: SEM images of half-cell after sintering with anode composition of Ni/$Ce_{0.8}Mo_{0.1}Gd_{0.1}O_{2+\delta}$ (a) and Ni/$Ce_{0.85}Mo_{0.05}Gd_{0.1}O_{2+\delta}$ (b)

5.2.1.3. MoO_3 gas infiltration

Various precursor materials containing Mo such as MoO_3, $NiMoO_4$, CMO, and CGMO were studied as a precursor material for anode screen printing paste. However, the results were inadequate due to their instability and volatility at high temperature. Therefore, MoO_3 gas state infiltration has been attempted to incorporate Mo to the anode layer during or after the standard cell manufacturing process. Figure 5.16a shows the support side picture of sintered half-cell after the MoO_3 gas infiltration process. A yellow powder was formed on the surface of the support, and it was identified as $NiMoO_4$ by XRD measurement, as shown in Figure 5.16b.

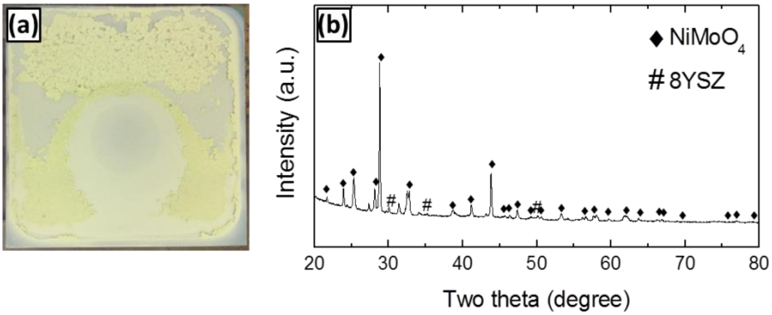

Figure 5.16: XRD result of the yellow powder on the support surface after the gas infiltration process

To check the existence of the $NiMoO_4$ phase at the inside of support, the cell cross-section was investigated by SEM and EDX. As shown in Figure 5.17, the cell microstructure was not significantly changed after the infiltration process except for the delamination and microstructure change at the bottom of the support. The structural change seems the result of the reaction between NiO and MoO_3 gas like $NiMoO_4$ formation, and this was confirmed by the XRD results. The point EDX measurement result also shows the Mo peak at the bottom of the support. However, there was no Mo inside the support. Instead, the MoO_3 reacts with NiO only at the surface of support because the support structure is too dense in the oxidized state to infiltrate MoO_3 gas into the inner structure of support and the dense electrolyte at the opposite side of support interrupts the MoO_3 gas flow through the cell structure. Additionally, the fast reaction between NiO and MoO_3 limit the diffusion depth until all of the NiO reacted.

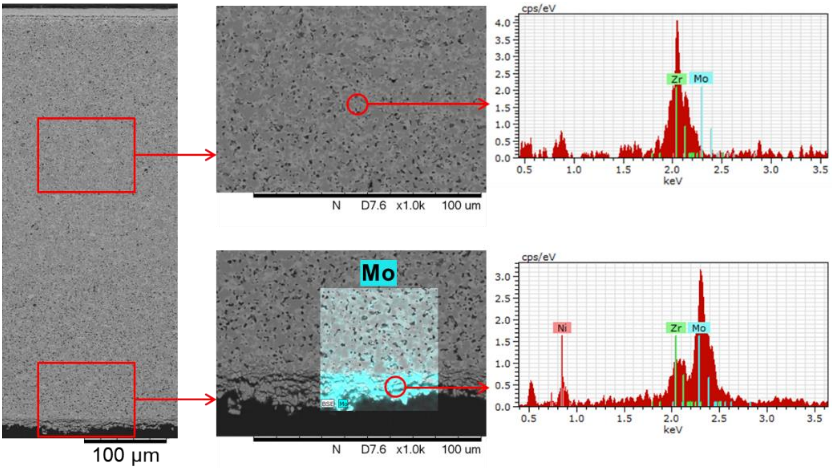

Figure 5.17: The cross-section SEM image and EDX result of the half-cell after the MoO_3 gas infiltration at 1000 °C for 3 h

The porosity of the sintered half-cell was not enough for the MoO_3 gas infiltration. Therefore, MoO_3 gas infiltration was tried during the sintering process. The cross-section microstructures of half-cell after sintering under MoO_3 atmosphere are shown in Figure 5.18 with different concentrations of MoO_3 in the crucible (a: 0.1 g, b: 0.2 g, and c: 0.5 g). The particle sizes of NiO and YSZ in the support after MoO_3 gas infiltration were coarsened compared to the particles in the support after sintering in air. Thus, it is assumed that the MoO_3 gas accelerates the sintering of the NiO and YSZ particles in the support. The electrolyte did not form a dense structure and the anode structure disappeared after sintering in all cases. As shown in Figure 5.18c, although Mo was found from a few particles in the structure, the overall structure was not suitable for cell operation. Initially, it was expected that Mo incorporates into the NiO or GDC in the anode layer without structural change, and the anode composition can be adjusted by the concentration of added MoO_3 powder in the crucible. However, anode structures and the entire cell structures are changed by MoO_3, and only small amounts of MoO_3 significantly affect cell sintering behavior.

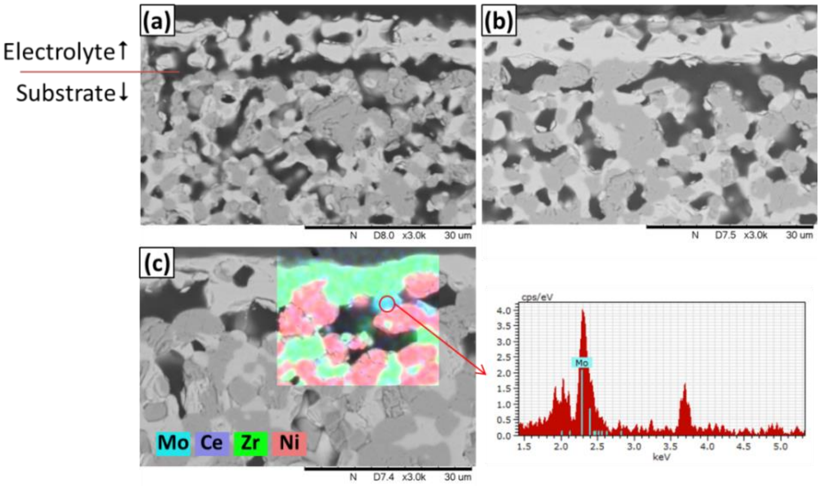

Figure 5.18: The cross-section SEM image of a sintered half-cell in MoO_3 atmosphere with different MoO_3 loading: 0.1 (a), 0.2 (b), and 0.5 (c) g

5.2.1.4. Mo thermal diffusion

In previous attempts of Mo incorporation, anodes with any kinds and states of Mo precursors show that the anode structure was destroyed after anode and electrolyte sintering at 1400 °C. Therefore, a stable Ni/GDC anode structure was prepared by 1400 °C sintering without Mo, and then the Mo precursor was applied on the surface of the anode and diffused into the anode by low-temperature heat treatment. In this case, the electrolyte can be applied afterward by the alternative method such as sputtering or vapor deposition [161, 162] to prevent Mo evaporation during electrolyte sintering. For the thermal diffusion of Mo, two different precursors of MoO_3 and $NiMoO_4$ were used. After the thermal diffusion, the residual powder was removed from the anode surface for the phase and microstructure analysis.

Figure 5.19 shows the microstructure and phase analysis result of Ni/GDC anode after MoO_3 treatment by SEM, EDX, and XRD. The result shows a new structure formation on the anode surface after 600 °C (Figure

5.19a) heat treatment, and this structure was less pronounced after higher temperature heat treatment of 800 °C (Figure 5.19b) and 1000 °C (Figure 5.19c). The new layer structure was identified as Mo and Ce containing composite by EDX mapping results. From the surface SEM images, the decline of the new structure by higher heat treatment was more easily shown. Almost all the Ni/GDC anode surface was covered by a new layer that is a bright phase after 600 °C heat treatment; however, the new structure was removed and a darker color of NiO phase was exposed after higher temperature heat treatments of 800 °C and 1000 °C. The new structure on the surface was analyzed by XRD and the results showed NiO and GDC main phases and secondary phases of $Ce_8Mo_{12}O_{49}$ and $Ce_2Mo_4O_{15}$. The peak intensity was reduced by high-temperature heat treatments, corresponding with the decline of the new layer structure in SEM images. This result shows good agreement with the previously reported study that when CeO_2 and MoO_3 react with each other at 600 °C in air, $Ce_8Mo_{12}O_{49}$ is formed under a CeO_2-rich condition and $Ce_2Mo_4O_{15}$ is formed under a MoO_3-excessive condition [163].

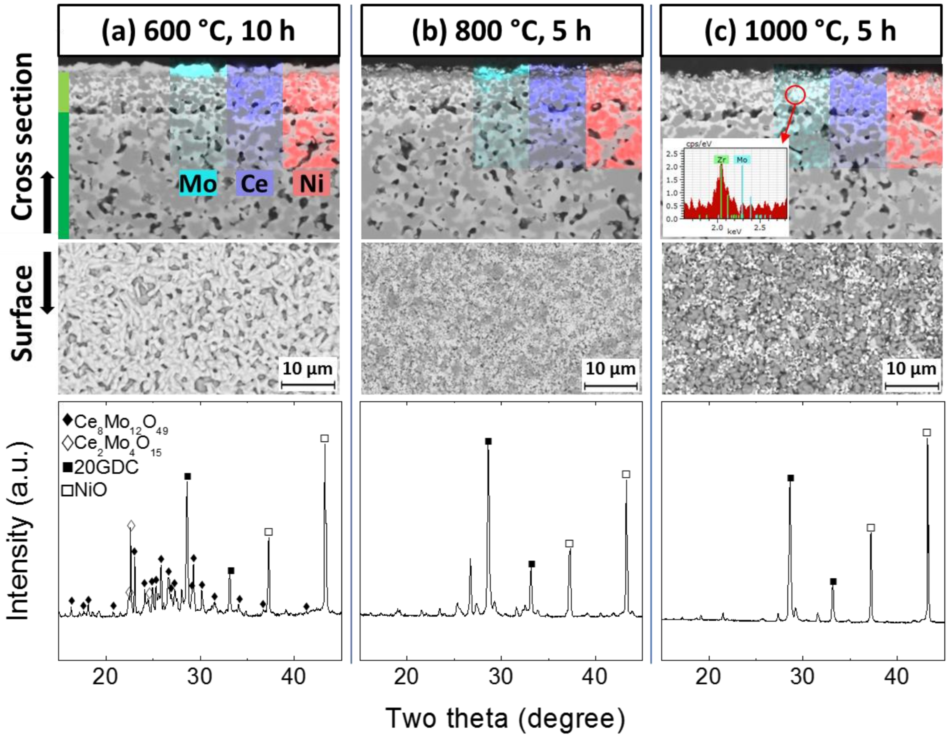

Figure 5.19: The microstructure and phase analysis result of Ni/GDC anode after MoO_3 treatment with different heat treatment 600 ℃, 10 h (a), 800 ℃, 5 h (b), and 1000 ℃, 5 h (c)

The microstructure and phase analysis results of the Ni/GDC anode after $NiMoO_4$ treatment is shown in Figure 5.20. The cross-section SEM image of Ni/GDC anode after 600 °C (Figure 5.20a) does not show any change compared to the microstructure before $NiMoO_4$ treatment in Figure 4.17. In contrast, a new layer structure was confirmed after the heat treatment at 800 °C (Figure 5.20b), and the EDX element mapping result identifies the new layer as Mo and Ce containing phases. After heat treatment at 1000 °C (Figure 5.20c), although the concentration of the new layer structure on the anode surface declined, the Mo-included phase was confirmed from inside the anode layer. The surface SEM images show the different anode structures by different heat treatment temperatures more clearly. After 600 °C heat treatment, a dense structure of the Ni/GDC anode surface was observed, meaning that the anode was simply unchanged by $NiMoO_4$ treatment. In the case of the anode after 800 °C heat treatment with $NiMoO_4$, the entire surface of the anode was covered by a new phase that contains Mo in the structure. After the heat treatment at 1000 °C, the anode surface showed three different phases of Mo, including new phase (larger particle size than others, medium brightness), NiO (low brightness), and GDC (high brightness). Through the XRD measurement, the Mo-containing phase was identified as $Ce(MoO_4)_2$ that was synthesized at the temperature above 800 °C [164].

The anode layer after the Mo thermal diffusion process showed different phase and structure according to the precursor materials. In the case of the MoO_3 precursor, the $Ce_8Mo_{12}O_{49}$ and $Ce_2Mo_4O_{15}$ phases were formed on the Ni/GDC anode surface. Since these Mo-containing phases have poor thermal stability ($Ce_8Mo_{12}O_{49}$ melting point is 964 °C) [163], the new layer was declined and evaporated after heat treatment at 800 °C and 1000 °C. Although the Mo-containing phase was formed on the anode layer using MoO_3, the Mo-containing phase is observed not inside the anode structure but instead only on the surface of the anode, meaning that the electro-catalytically active area was simply unchanged. The $NiMoO_4$ precursor does not react with Ni/GDC anode at 600 °C. Thus, the $NiMoO_4$ phase is more stable than any other Ce-Mo based phase at 600 °C in air. After heat treatment at 800 °C, the $Ce(MoO_4)_2$ phase appeared and could be found inside the anode structure after the heat treatment at 1000 °C. The $Ce(MoO_4)_2$ phase seems more stable than $NiMoO_4$ at temperatures above 800 °C. Although it was possible to incorporate Mo into the sintered NiO/GDC anode by applying $NiMoO_4$ and heat treatment at 1000 °C, further study is required about the $Ce(MoO_4)_2$ phase to develop this process. There are several reports about the $Ce(MoO_4)_2$ phase as pigments and photo-catalysts [165, 166], but the electrochemical and physical property of $Ce(MoO_4)_2$ is not fully studied.

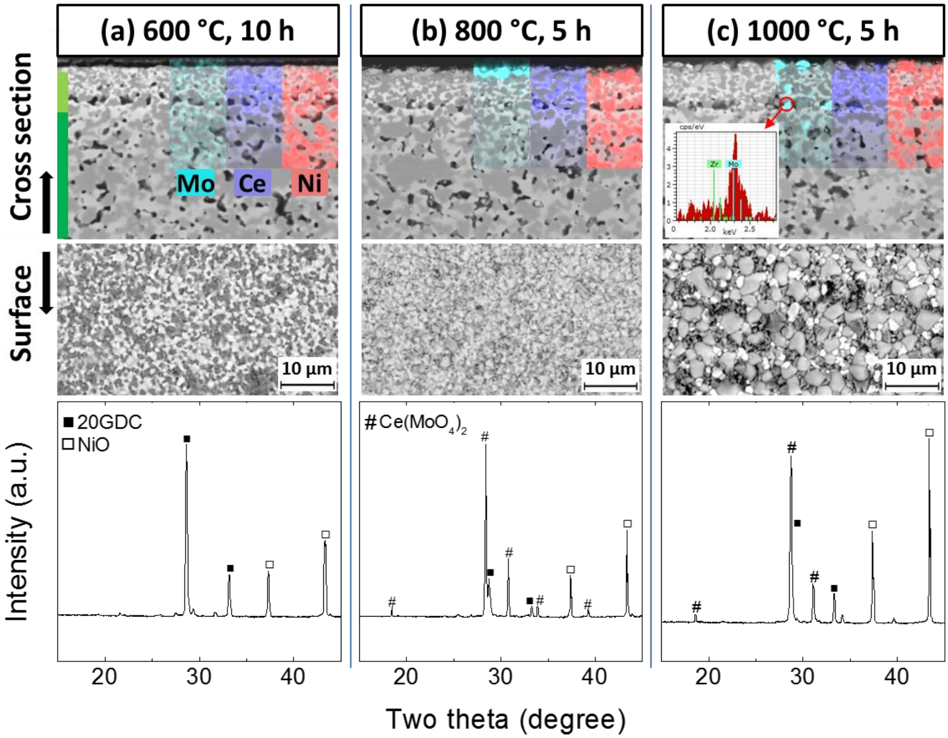

Figure 5.20: The microstructure and phase analysis result of Ni/GDC anode after NiMoO$_4$ treatment with different heat treatment 600 °C, 10 h (a), 800 °C, 5 h (b), and 1000 °C, 5 h (c)

5.2.2. ESC development and outlook of the Mo-containing anode

5.2.2.1. Cell manufacturing with Mo infiltration

Since the ASCs development with Mo containing anode has difficulties in manufacturing by high-temperature electrolyte sintering, an ESC was developed using the pre-sintered electrolyte support. To decide on the electrolyte material, the properties of various oxygen ion conduction materials were compared [167-169] and the 6 mol% scandia stabilized zirconia (6ScSZ) was chosen as the electrolyte support. Although GDC has higher ionic conductivity, GDC can become electronically conductive under reducing atmosphere by Ce ion reduction. The 8YSZ, which is the most preferred electrolyte material in terms of stability and ionic conductivity, shows poor mechanical strength, and this result is quite important for the support material in ESC design. The higher amount of Sc doping causes high ionic conductivity, but it shows poor mechanical strength. Several commercially available electrolyte materials and their properties are listed in Table 5.5.

Table 5.5: The properties of several doped ZrO_2 electrolytes (source: Keramische Folien GmbH & Co, Germany)

	3YSZ	8YSZ	6ScSZ	10Sc1CeSZ
Conductivity @ 850 ℃ (S/m)	2.2	8.0	8.4	17
Relative strength (8YSZ = 100 %)	330	100	260	140
Sinter density (g/cm^3)	6.00	5.95	5.86	5.70

On the electrolyte support, Ni/GDC anode paste was applied and the ammonium molybdate tetrahydrate water-based solution was then infiltrated, as described in Section 3.1.3.4, and Figure 5.21 shows the SEM images of the Mo-Ni/GDC anode after reduction. The surface image of Figure 5.21a shows the typical porous anode structure, but the particle size of Ni and GDC was smaller than the particles in the ASC cell anode. The particle size was affected by the lowered anode sintering temperature of 1200 °C and the pre-sintered electrolyte, and the particle size does not shrink during anode sintering, unlike the anode support in ASC. The EDX was applied to two points of Ni (point 1) and GDC (point 2). Point 1 shows high Ni peak intensity with additional Mo and Ce peaks. At point 2, the peak intensity of Ni is lower and Ce is higher than point 1; simultaneously, the Mo peak intensity is lower than point 1. These results show that the Mo peak intensity corresponds to Ni peak intensity; in other words, Mo forms a composite with Ni instead of entering the GDC in the anode structure. Figure 5.21b shows the fractured cross-section SEM image with different magnifications, and it shows a columnar structured Mo particle in the red circle denoted in the image that does not appear in the Ni/GDC anode without Mo infiltration.

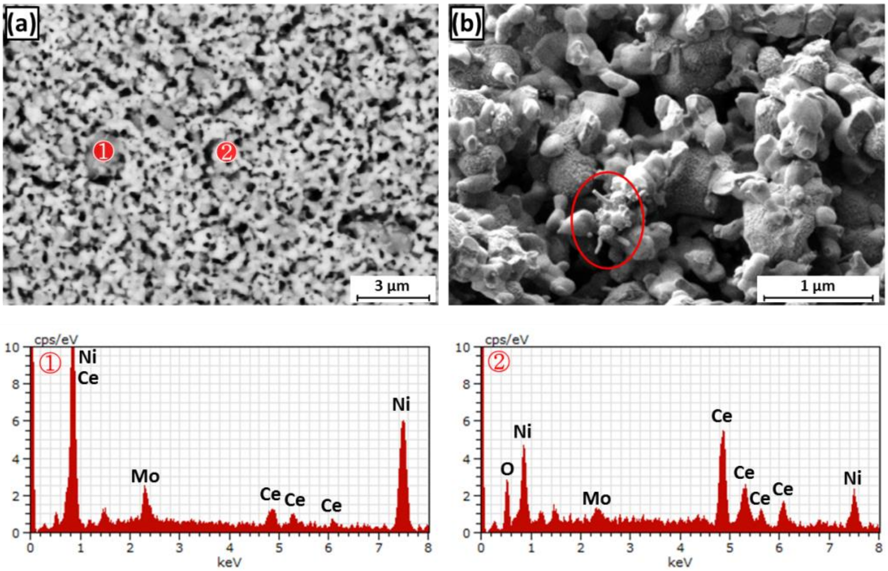

Figure 5.21: SEM images of Ni/GDC anode with Mo infiltration and the point EDX result of Ni (1) and GDC (2) particles

5.2.2.2. Cell test result

Figure 5.22a shows the single cell measurement result of two different cells with a Ni/GDC anode with and without Mo infiltration (Ni/GDC and Mo-Ni/GDC). The cell test result shows significant performance improvement by Mo infiltration, as shown in Figure 5.22a. In the operating condition of 60 % of H_2O and 40 % of H_2 at 800 °C, the current density at 0.7 V of the cells increased from 0.09 to 0.22 A/cm^2 by Mo infiltration. However, the performance of Mo-Ni/GDC anode was much lower than other similar results [170, 171] due to the non-optimized microstructure and electrode thickness. Nonetheless, the result of sulfur tolerance with polarization ASR changes in Figure 5.22b shows an interesting phenomenon. In the case of Ni/GDC anode, ASR increases immediately after the introduction of 1 ppm of H_2S as opposed to the Mo-Ni/GDC anode that shows a decrease in ASR. There are several reports about the sulfur enhancement effect by the Mo-containing anode material [102, 172, 173], but the enhancing mechanism is not clear yet. One hypothesis is a formation of the conductive phase on the anode surface such as MoS_2, which has been identified on the surface of $Gd_2Ti_{1.4}Mo_{0.6}O_7$ anode after exposure to 10% H_2S/90% H_2 [102]. However, the cell performance is still not high enough for practical use and long-term stability test is required.

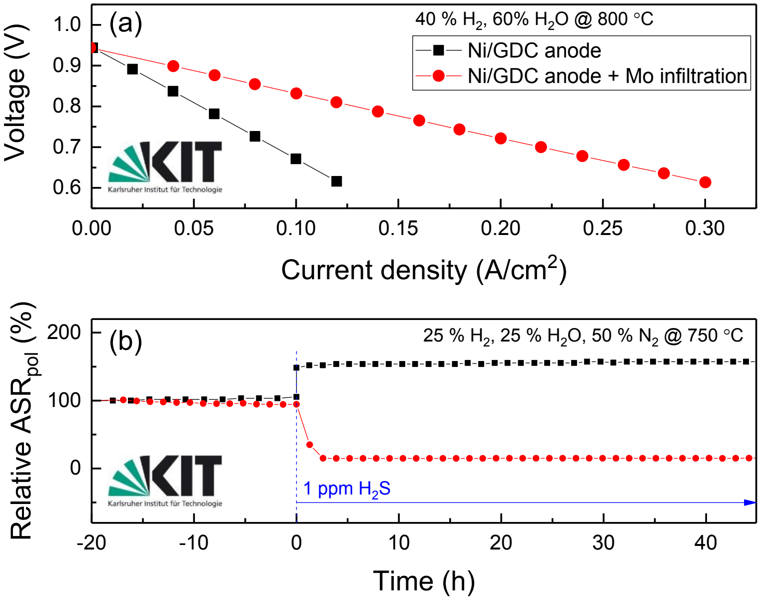

Figure 5.22: Single cell measurement results of the ESC cell with the Ni/GDC anode with and without Mo infiltration and relative ASR (Measured at KIT IAM-WET by N. Russner)

5.2.3. Discussion of Mo incorporation into the anode

In Table 5.6, the processes that have been tried so far in this study are summarized and evaluated. Almost all results with ASC were not successful due to the low thermal stability of Mo-precursors and their high volatility. These reasons seem to be the cause of the limited use of Mo in the high-temperature application although Mo shows in principle superior catalytic activity.

In the case of the ESC cell, the performance was significantly improved by Mo infiltration. This increase is commonly reported in many studies [79, 80, 174, 175], and it is derived by electrochemical property changes by the novel material incorporation and the microstructure changes of the offering more surface area and improved materials connectivity. Since the Ni/GDC anode microstructure was not optimized with ESC structure, it is difficult to conclude how much the performance was improved only by the addition of Mo material. In contrast, the ASR test with 1 ppm H_2S shows sulfur enhancing behavior with Mo incorporation. It needs further analysis such as phase analysis and material stability test as it was totally opposed to the conventional anode materials. This result shows the potential of Mo as a sulfur tolerant anode material; moreover, this Mo infiltration can be applied to ASC cell support. The infiltration method is normally not favorable for an anode in ASC, but support material modification should be relatively easy and could be effective to prevent anode support erosion.

Table 5.6: Summary of Mo containing anode development in this study

Cell type	**Method**		**Feature**	**Applicability(a)**
ASC	Screen printing with Mo included precursor		Anode structure was not established, material melting and evaporation	×
	MoO_3 gas infiltration	After cell sintering	No Mo in the cell Dense cell ➔ slow diffusion velocity	×
		During cell sintering	Particle coarsening, anode and electrolyte structure destroyed	×
	Mo thermal diffusion	MoO_3 diffusion	Mo containing thin layer formed, but evaporated at 1000 ˚C	△
		$NiMoO_4$ diffusion	$Ce(MoO_4)_2$ phase distributed in the anode, but the properties of $Ce(MoO_4)_2$ is unknown	△
ESC	Screen printing + infiltration		Suitable layer structure was formed, the existence of Mo needs to be proven	○

(a) ○: high, △:low, ×: very low (b) HT: heat treatment

6. Conclusion

In this study, a consideration of the flexible fuel application to the SOFC is described related with current status, limitations, and solutions. Various fuels include natural gas, synthetic gas obtained from fossil fuels, and biomass, beyond pure hydrogen. Their biggest problem is the anode poisoning induced by impurities such as tar and sulfur. This problem can be solved by removing impurities from fuel or direct tar and sulfur reforming with developing alternative anode materials. This study analyzed the mechanisms for the effects and degradation of impurities using currently developed SOFC and tried to develop alternative anode materials to improve the resistivity against impurities. The conclusions from the study can be summarized as follows:

i). Although current state-of-the-art SOFC demonstrates excellent stability and performance close to commercialization under pure hydrogen condition, it is highly vulnerable to fuel containing impurities such as tar and sulfur. The erosion of the supports by phenol and the rapid degradation of cell performance by naphthalene were observed, and sulfur indicated significantly faster and higher degradation levels. When the actual bio-syngas was applied to the stack, a large amount of carbon formed by the complex action of multi tars. The carbon deposition leads to significant pressure drop prior to the cell degradation, resulting in the stack's operation halted in a short period. Therefore, it is essential to clean and reform sulfur and tars before applying the current system.

ii). To increase the resistance to impurities contained in fuel, the Ni/GDC anode was applied as an alternative anode material instead of the Ni/YSZ anode. However, the result shows poor performance and resistance due to the inter-diffusion of the YSZ electrolyte and the GDC. The mixed phase shows worse electrical properties than both YSZ and GDC, and the microstructure was also changed by differential diffusion between YSZ and GDC that cause surface area reduction in the anode layer. It is required to replace the electrolyte materials to have a pure GDC phase in the anode layer so that the resistivity of Ni/GDC anode against impurities in the fuel can be discussed compared to the Ni/YSZ anode.

iii). A study was conducted to increase the resistance to impurities by adding Mo in to the anode. However, the ASCs manufacturing process includes high-temperature electrolyte sintering, resulting in the loss of Mo due to its poor thermal stability. It has been concluded that it is practically impossible to produce ASCs using Mo-containing precursors. The ESC design that can avoid high-temperature sintering of the anode layer was used to test the effects of Mo in the anode, and the results show both improved performance and sulfur tolerance.

7. Reference

[1] S.L. Douvartzides, F.A. Coutelieris, A.K. Demin, P.E. Tsiakaras, Fuel options for solid oxide fuel cells: A thermodynamic analysis, AIChE Journal 49(1) (2004) 248-257.

[2] S. McIntosh, R.J. Gorte, Direct hydrocarbon solid oxide fuel cells, Chem Rev 104(10) (2004) 4845-65.

[3] G.J. Saunders, J. Preece, K. Kendall, Formulating liquid hydrocarbon fuels for SOFCs, Journal of Power Sources 131(1-2) (2004) 23-26.

[4] D.X. Cao, Y. Sun, G.L. Wang, Direct carbon fuel cell: Fundamentals and recent developments, Journal of Power Sources 167(2) (2007) 250-257.

[5] J. Van herle, Y. Membrez, O. Bucheli, Biogas as a fuel source for SOFC co-generators, Journal of Power Sources 127(1-2) (2004) 300-312.

[6] C. Athanasiou, F. Coutelieris, E. Vakouftsi, V. Skoulou, E. Antonakou, G. Marnellos, A. Zabaniotou, From biomass to electricity through integrated gasification/SOFC system-optimization and energy balance, Int J Hydrogen Energ 32(3) (2007) 337-342.

[7] S. Al Arni, B. Bosio, E. Arato, Syngas from sugarcane pyrolysis: An experimental study for fuel cell applications, Renewable Energy 35(1) (2010) 29-35.

[8] L. Blum, H.P. Buchkremer, S. Gross, A. Gubner, L.G.J.d. Haart, H. Nabielek, W.J. Quadakkers, U. Reisgen, M.J. Smith, R. Steinberger-Wilckens, R.W. Steinbrech, F. Tietz, I.C. Vinke, Solid Oxide Fuel Cell Development at Forschungszentrum Juelich, Fuel Cells 7(3) (2007) 204-210.

[9] E.J. Naimaster, A.K. Sleiti, Potential of SOFC CHP systems for energy-efficient commercial buildings, Energy and Buildings 61 (2013) 153-160.

[10] H.R. Ellamla, I. Staffell, P. Bujlo, B.G. Pollet, S. Pasupathi, Current status of fuel cell based combined heat and power systems for residential sector, Journal of Power Sources 293 (2015) 312-328.

[11] J. Mermelstein, M. Millan, N.P. Brandon, The impact of carbon formation on Ni–YSZ anodes from biomass gasification model tars operating in dry conditions, Chem Eng Sci 64(3) (2009) 492-500.

[12] T. Namioka, T. Naruse, R. Yamane, Behavior and mechanisms of Ni/ScSZ cermet anode deterioration by trace tar in wood gas in a solid oxide fuel cell, Int J Hydrogen Energ 36(9) (2011) 5581-5588.

[13] M. Liu, M. G. Millan-Agorio, P.V. Aravind, N.P. Brandon, Influence of Operation Conditions on Carbon Deposition in SOFCs Fuelled by Tar-Containing Biosyngas, 2011.

[14] D. Pumiglia, S. Vaccaro, A. Masi, S.J. McPhail, M. Falconieri, S. Gagliardi, L. Della Seta, M. Carlini, Aggravated test of Intermediate temperature solid oxide fuel cells fed with tar-contaminated syngas, Journal of Power Sources 340 (2017) 150-159.

[15] K. Sasaki, K. Susuki, A. Iyoshi, M. Uchimura, N. Imamura, H. Kusaba, Y. Teraoka, H. Fuchino, K. Tsujimoto, Y. Uchida, N. Jingo, H2S poisoning of solid oxide fuel cells, J Electrochem Soc 153(11) (2006) A2023-A2029.

[16] Z. Cheng, H. Abernathy, M. Liu, Raman Spectroscopy of Nickel Sulfide Ni3S2, The Journal of Physical Chemistry C 111(49) (2007) 17997-18000.

[17] W.M. Harris, J.J. Lombardo, G.J. Nelson, B. Lai, S. Wang, J. Vila-Comamala, M. Liu, M. Liu, W.K.S. Chiu, Three-Dimensional Microstructural Imaging of Sulfur Poisoning-Induced Degradation in a Ni-YSZ Anode of Solid Oxide Fuel Cells, Sci Rep-Uk 4 (2014) 5246.

[18] Z. Abu El-Rub, E.A. Bramer, G. Brem, Review of Catalysts for Tar Elimination in Biomass Gasification Processes, Industrial & Engineering Chemistry Research 43(22) (2004) 6911-6919.

[19] W.R. Grove, LXXII. On a gaseous voltaic battery, The London, Edinburgh, and Dublin Philosophical Magazine and Journal of Science 21(140) (1842) 417-420.

[20] I. Pilatowsky Figueroa, R.J. Romero, C.A. Isaza, S.A. Gamboa, P.J. Sebastian, W. Rivera, Cogeneration fuel cell-sorption air conditioning systems, Springer-Verlag, London ; New York, 2011.

[21] E.J. Cairns, Liebhafs.Ha, Increased Irreversibility Caused by Composition Changes in Fuel Cells, Energ Convers 9(2) (1969) 63-&.

[22] A.I. Ioffe, D.S. Rutman, S.V. Karpachov, On the nature of the conductivity maximum in zirconia-based solid electrolytes, Electrochim Acta 23(2) (1978) 141-142.

[23] J.A. Kilner, B.C.H. Steele, 5 - Mass Transport in Anion-Deficient Fluorite Oxides, in: O.T. Sørensen (Ed.), Nonstoichiometric Oxides, Academic Press1981, pp. 233-269.

[24] M. Filal, C. Petot, M. Mokchah, C. Chateau, J.L. Carpentier, Ionic conductivity of yttrium-doped zirconia and the “composite effect”, Solid State Ionics 80(1) (1995) 27-35.

[25] J.W. Fergus, Electrolytes for solid oxide fuel cells, Journal of Power Sources 162(1) (2006) 30-40.

[26] Q.M. Nguyen, T. Takahashi, Science and technology of ceramic fuel cells, Elsevier Science, Amsterdam ; New York, 1995.

[27] M. Yashima, M. Kakihana, M. Yoshimura, Metastable-stable phase diagrams in the zirconia-containing systems utilized in solid-oxide fuel cell application, Solid State Ionics 86-88 (1996) 1131-1149.

[28] H. Fujimori, M. Yashima, M. Kakihana, M. Yoshimura, β-cubic phase transition of scandia-doped zirconia solid solution: Calorimetry, x-ray diffraction, and Raman scattering, J Appl Phys 91(10) (2002) 6493-6498.

[29] T. Ishihara, H. Matsuda, Y. Takita, Doped LaGaO3 Perovskite Type Oxide as a New Oxide Ionic Conductor, J Am Chem Soc 116(9) (1994) 3801-3803.

[30] M. Hrovat, A. Ahmad-Khanlou, Z. Samardzija, J. Holc, Interactions between lanthanum gallate based solid electrolyte and ceria, Mater Res Bull 34(12-13) (1999) 2027-2034.

[31] Z. Gao, L.V. Mogni, E.C. Miller, J.G. Railsback, S.A. Barnett, A perspective on low-temperature solid oxide fuel cells, Energ Environ Sci 9(5) (2016) 1602-1644.

[32] L. Blum, L.G.J. de Haart, J. Malzbender, N.H. Menzler, J. Remmel, R. Steinberger-Wilckens, Recent results in Jülich solid oxide fuel cell technology development, Journal of Power Sources 241 (2013) 477-485.

[33] E.N. Armstrong, K.L. Duncan, E.D. Wachsman, Effect of A and B-site cations on surface exchange coefficient for ABO3 perovskite materials, Physical Chemistry Chemical Physics 15(7) (2013) 2298-2308.

[34] S. Uhlenbruck, T. Moskalewicz, N. Jordan, H.J. Penkalla, H.P. Buchkremer, Element interdiffusion at electrolyte–cathode interfaces in ceramic high-temperature fuel cells, Solid State Ionics 180(4-5) (2009) 418-423.

[35] F. Han, R. Muecke, T. Van Gestel, A. Leonide, N.H. Menzler, H.P. Buchkremer, D. Stover, Novel high-performance solid oxide fuel cells with bulk ionic conductance dominated thin-film electrolytes, Journal of Power Sources 218 (2012) 157-162.

[36] F. Morin, G. Trudel, Y. Denos, The phase stability of La 0.5Sr 0.5CoO 3 − δ, Solid State Ionics 96(3) (1997) 129-139.

[37] L. Blum, B. De Haart, J. Malzbender, N. H Menzler, J. Remmel, R. Steinberger-Wilckens, Recent Results in JÜLICH SOFC Technology Development, 2012.

[38] J.G. Railsback, A.C. Johnston-Peck, J. Wang, J.B. Tracy, Size-Dependent Nanoscale Kirkendall Effect During the Oxidation of Nickel Nanoparticles, ACS Nano 4(4) (2010) 1913-1920.

[39] T. Klemenso, C. Chung, P.H. Larsen, M. Mogensen, The mechanism behind redox instability of anodes in high-temperature SOFCs, J Electrochem Soc 152(11) (2005) A2186-A2192.

[40] M. Ettler, G. Blaß, N.H. Menzler, Characterisation of Ni–YSZ-Cermets with Respect to Redox Stability, Fuel Cells 7(5) (2007) 349-355.

[41] M.C. Tucker, H. Kurokawa, C.P. Jacobson, L.C. De Jonghe, S.J. Visco, A fundamental study of chromium deposition on solid oxide fuel cell cathode materials, Journal of Power Sources 160(1) (2006) 130-138.

[42] D.-J. Liu, J. Almer, T. Cruse, Characterization of Cr Poisoning in a Solid Oxide Fuel Cell Cathode Using a High Energy X-ray Microbeam, J Electrochem Soc 157(5) (2010) B744-B750.

[43] M. Kornely, N.H. Menzler, A. Weber, E. Ivers-Tiffée, Degradation of a High Performance SOFC Cathode by Cr-Poisoning at OCV-Conditions, Fuel Cells 13(4) (2013) 506-510.

[44] N. Shaigan, W. Qu, D.G. Ivey, W.X. Chen, A review of recent progress in coatings, surface modifications and alloy developments for solid oxide fuel cell ferritic stainless steel interconnects, Journal of Power Sources 195(6) (2010) 1529-1542.

[45] N.S. Waluyo, R.H. Song, S.B. Lee, T.H. Lim, S.J. Park, J.W. Lee, Electrophoretically Deposited LaNi0.6Fe0.4O3 Perovskite Coatings on Metallic Interconnects for Solid Oxide Fuel Cells, J Electrochem Soc 163(10) (2016) F1245-F1250.

[46] N. Grünwald, D. Sebold, Y.J. Sohn, N.H. Menzler, R. Vaßen, Self-healing atmospheric plasma sprayed Mn1.0Co1.9Fe0.1O4 protective interconnector coatings for solid oxide fuel cells, Journal of Power Sources 363 (2017) 185-192.

[47] A. Demirbaş, Hydrogen Production from Biomass by the Gasification Process, Energy Sources 24(1) (2002) 59-68.

[48] M. Puig-Arnavat, J.C. Bruno, A. Coronas, Review and analysis of biomass gasification models, Renew Sust Energ Rev 14(9) (2010) 2841-2851.

[49] C. Higman, M.v.d. Burgt, Gasification, 2nd ed., Gulf Professional Pub./Elsevier Science, Amsterdam ; Boston, 2008.

[50] A. van der Drift, J. van Doorn, J.W. Vermeulen, Ten residual biomass fuels for circulating fluidized-bed gasification, Biomass Bioenerg 20(1) (2001) 45-56.

[51] J. Gañan, A. Al-Kassir Abdulla, A.B. Miranda, J. Turegano, S. Correia, E.M. Cuerda, Energy production by means of gasification process of residuals sourced in Extremadura (Spain), Renewable Energy 30(11) (2005) 1759-1769.

[52] A.V. Bridgwater, The Technical and Economic-Feasibility of Biomass Gasification for Power-Generation, Fuel 74(5) (1995) 631-653.

[53] J. Gil, J. Corella, M.P. Aznar, M.A. Caballero, Biomass gasification in atmospheric and bubbling fluidized bed: Effect of the type of gasifying agent on the product distribution, Biomass Bioenerg 17(5) (1999) 389-403.

[54] M. Asadullah, Biomass gasification gas cleaning for downstream applications: A comparative critical review, Renewable and Sustainable Energy Reviews 40 (2014) 118-132.

[55] C.G. Visconti, L. Lietti, P. Forzatti, R. Zennaro, Fischer–Tropsch synthesis on sulphur poisoned Co/Al2O3 catalyst, Applied Catalysis A: General 330 (2007) 49-56.

[56] D.E. Sparks, G. Jacobs, M.K. Gnanamani, V.R.R. Pendyala, W. Ma, J. Kang, W.D. Shafer, R.A. Keogh, U.M. Graham, P. Gao, B.H. Davis, Poisoning of cobalt catalyst used for Fischer–Tropsch synthesis, Catalysis Today 215 (2013) 67-72.

[57] K. Gerdes, M.C. Williams, R. Gemmen, B. White, A Global Framework for Examination of Degradation in SOFC, Solid Oxide Fuel Cells 13 (Sofc-Xiii) 57(1) (2013) 289-297.

[58] A. Nakajo, F. Mueller, J. Brouwer, J. Van Herle, D. Favrat, Mechanical reliability and durability of SOFC stacks. Part I: Modelling of the effect of operating conditions and design alternatives on the reliability, Int J Hydrogen Energ 37(11) (2012) 9249-9268.

[59] X. Wang, A. Atkinson, Simulation and Prediction of 3-D Microstructural Evolution and Long Term Performance of Ni-YSZ Anode, Ecs Transactions 68(1) (2015) 2867-2873.

[60] M. Finsterbusch, A. Lussier, J.A. Schaefer, Y.U. Idzerda, Electrochemically driven cation segregation in the mixed conductor La0.6Sr0.4Co0.2Fe0.8O3-delta, Solid State Ionics 212 (2012) 77-80.

[61] W.J. Quadakkers, J. Piron-Abellan, V. Shemet, L. Singheiser, Metallic interconnectors for solid oxide fuel cells – a review, Materials at High Temperatures 20(2) (2003) 115-127.

[62] M. Finsterbusch, A. Lussier, J.A. Schaefer, Y.U. Idzerda, Electrochemically driven cation segregation in the mixed conductor La0.6Sr0.4Co0.2Fe0.8O3 − δ, Solid State Ionics 212 (2012) 77-80.

[63] G.M. Rupp, H. Téllez, J. Druce, A. Limbeck, T. Ishihara, J. Kilner, J. Fleig, Surface chemistry of La0.6Sr0.4CoO3−δ thin films and its impact on the oxygen surface exchange resistance, J Mater Chem A 3(45) (2015) 22759-22769.

[64] T. Chen, W.G. Wang, H. Miao, T.S. Li, C. Xu, Evaluation of carbon deposition behavior on the nickel/yttrium-stabilized zirconia anode-supported fuel cell fueled with simulated syngas, Journal of Power Sources 196(5) (2011) 2461-2468.

[65] W. Wang, C. Su, Y.Z. Wu, R. Ran, Z.P. Shao, Progress in Solid Oxide Fuel Cells with Nickel-Based Anodes Operating on Methane and Related Fuels, Chem Rev 113(10) (2013) 8104-8151.

[66] J. Xiao, Y. Xie, J. Liu, M. Liu, Deactivation of nickel-based anode in solid oxide fuel cells operated on carbon-containing fuels, Journal of Power Sources 268 (2014) 508-516.

[67] H.J. Grabke, R. Krajak, E.M. Müller-Lorenz, S. Strauß, Metal dusting of nickel-base alloys, Materials and Corrosion 47(9) (1996) 495-504.

[68] J. Klöwer, H.J. Grabke, E.M. Müller-Lorenz, Metal dusting of nickel-base alloys, Materials and Corrosion 49(5) (1998) 328-329.

[69] C.M. Chun, G. Bhargava, T.A. Ramanarayanan, Metal Dusting Corrosion of Nickel-Based Alloys, J Electrochem Soc 154(5) (2007) C231.

[70] A. Zekri, K. Herbrig, M. Knipper, J. Parisi, T. Plaggenborg, Nickel Depletion and Agglomeration in SOFC Anodes During Long-Term Operation, Fuel Cells 17(3) (2017) 359-366.

[71] K. Ke, A. Gunji, H. Mori, S. Tsuchida, H. Takahashi, K. Ukai, Y. Mizutani, H. Sumi, M. Yokoyama, K. Waki, Effect of oxide on carbon deposition behavior of CH4 fuel on Ni/ScSZ cermet anode in high temperature SOFCs, Solid State Ionics 177(5) (2006) 541-547.

[72] H. Jeong, M. Geis, C. Lenser, S. Lobe, S. Herrmann, S. Fendt, N.H. Menzler, O. Guillon, Coupling SOFCs to biomass gasification – The influence of phenol on cell degradation in simulated bio-syngas. Part II – Post-test analysis, Int J Hydrogen Energ (2018).

[73] N.J.J. Dekker, J.P.P. Ouweltjes, B. Rietveld, Conversion of Simulated Biogas in a SOFC: The Effect of Organic Compounds, Ecs Transactions 7(1) (2007) 1465-1473.

[74] M. Hauth, W. Lerch, K. König, J. Karl, Impact of naphthalene on the performance of SOFCs during operation with synthetic wood gas, Journal of Power Sources 196(17) (2011) 7144-7151.

[75] D. Papurello, A. Lanzini, P. Leone, M. Santarelli, The effect of heavy tars (toluene and naphthalene) on the electrochemical performance of an anode-supported SOFC running on bio-syngas, Renewable Energy 99 (2016) 747-753.

[76] S.K. Schubert, M. Kusnezoff, A. Michaelis, S.I. Bredikhin, Comparison of the performances of single cell solid oxide fuel cell stacks with Ni/8YSZ and Ni/10CGO anodes with H2S containing fuel, Journal of Power Sources 217 (2012) 364-372.

[77] T.S. Li, W. Guo Wang, Sulfur-poisoned Ni-based solid oxide fuel cell anode characterization by varying water content, 2011.

[78] J.-H. Wang, M. Liu, Computational study of sulfur–nickel interactions: A new S–Ni phase diagram, Electrochem Commun 9(9) (2007) 2212-2217.

[79] H. Kurokawa, T.Z. Sholklapper, C.P. Jacobson, L.C. De Jonghe, S.J. Visco, Ceria nanocoating for sulfur tolerant Ni-based anodes of solid oxide fuel cells, Electrochem Solid St 10(9) (2007) B135-B138.

[80] J.W. Yun, S.P. Yoon, S. Park, H.S. Kim, S.W. Nam, Analysis of the regenerative H2S poisoning mechanism in Ce0.8Sm0.2O2-coated Ni/YSZ anodes for intermediate temperature solid oxide fuel cells, Int J Hydrogen Energ 36(1) (2011) 787-796.

[81] K.J. Meador, A. Gevins, D.W. Loring, L.K. McEvoy, P.G. Ray, M.E. Smith, G.K. Motamedi, B.M. Evans, C. Baum, Neuropsychological and neurophysiologic effects of carbamazepine and levetiracetam, Neurology 69(22) (2007) 2076-2084.

[82] O.A. Marina, C.A. Coyle, M.H. Engelhard, L.R. Pederson, Mitigation of Sulfur Poisoning of Ni/Zirconia SOFC Anodes by Antimony and Tin, J Electrochem Soc 158(4) (2011) B424-B429.

[83] H.J. Park, G.M. Choi, Oxygen permeability of gadolinium-doped ceria at high temperature, J Eur Ceram Soc 24(6) (2004) 1313-1317.

[84] L.D. Jadhav, M.G. Chourashiya, K.M. Subhedar, A.K. Tyagi, J.Y. Patil, Synthesis of nanocrystalline Gd doped ceria by combustion technique, J Alloy Compd 470(1-2) (2009) 383-386.

[85] L. Zhang, S.P. Jiang, H.Q. He, X.B. Chen, J. Ma, X.C. Song, A comparative study of H2S poisoning on electrode behavior of Ni/YSZ and Ni/GDC anodes of solid oxide fuel cells, Int J Hydrogen Energ 35(22) (2010) 12359-12368.

[86] C.H. Bartholomew, P.K. Agrawal, J.R. Katzer, Sulfur Poisoning of Metals, Adv Catal 31 (1982) 135-242.

[87] H.P. He, R.J. Gorte, J.M. Vohs, Highly sulfur tolerant Cu-ceria anodes for SOFCs, Electrochem Solid St 8(6) (2005) A279-A280.

[88] W. Wang, H.Y. Zhu, G.M. Yang, H.J. Park, D.W. Jung, C. Kwak, Z.P. Shao, A NiFeCu alloy anode catalyst for direct-methane solid oxide fuel cells, Journal of Power Sources 258 (2014) 134-141.

[89] H.C. Tsai, S.I. Morozov, T.H. Yu, B.V. Merinov, W.A. Goddard, First-Principles Modeling of Ni_4M (M = Co, Fe, and Mn) Alloys as Solid Oxide Fuel Cell Anode Catalyst for Methane Reforming, J Phys Chem C 120(1) (2016) 207-214.

[90] H.J. Wu, V. La Parola, G. Pantaleo, F. Puleo, A.M. Venezia, L.F. Liotta, Ni-Based Catalysts for Low Temperature Methane Steam Reforming: Recent Results on Ni-Au and Comparison with Other Bi-Metallic Systems, Catalysts 3(2) (2013) 563-583.

[91] M.J. Escudero, I.G. de Parada, A. Fuerte, J.L. Serrano, Analysis of the electrochemical performance of MoNi-CeO_2 cermet as anode material for solid oxide fuel cell. Part I. H_2, CH_4 and H_2/CH_4 mixtures as fuels, Journal of Power Sources 253 (2014) 64-73.

[92] C. Neofytidis, M. Athanasiou, S.G. Neophytides, D.K. Niakolas, Sulfur Tolerance of Au-Mo-Ni/GDC SOFC Anodes Under Various CH_4 Internal Steam Reforming Conditions, Top Catal 58(18-20) (2015) 1276-1289.

[93] B. Hua, M. Li, Y.Q. Zhang, J. Chen, Y.F. Sun, N. Yan, J. Li, J.L. Luo, Facile Synthesis of Highly Active and Robust Ni-Mo Bimetallic Electrocatalyst for Hydrocarbon Oxidation in Solid Oxide Fuel Cells, Acs Energy Lett 1(1) (2016) 225-230.

[94] M. Kuhn, J.A. Rodriguez, J. Hrbek, Reaction of S_2 with XMo(110) (X=Fe, Pt or Al) surfaces: Admetal-promoted sulfidation of Mo and the behavior of hydrodesulfurization catalysts, Surf Sci 365(1) (1996) 53-68.

[95] J.A. Rodriguez, Properties of Fe, Co, Ni, Cu and Zn on S/Mo(110) surfaces and MoS_x films: Metal-metal interactions and the behavior of HDS catalysts, Polyhedron 16(18) (1997) 3177-3184.

[96] S. Harris, R.R. Chianelli, Catalysis by Transition-Metal Sulfides - a Theoretical and Experimental-Study of the Relation between the Synergic Systems and the Binary Transition-Metal Sulfides, J Catal 98(1) (1986) 17-31.

[97] O.A. Marina, J.W. Stevenson, Development of ceramic composites as SOFC anodes, 2003.

[98] R. Mukundan, E.L. Brosha, F.H. Garzon, Sulfur tolerant anodes for SOFCs, Electrochem Solid St 7(1) (2004) A5-A7.

[99] Y.H. Huang, R.I. Dass, J.C. Denyszyn, J.B. Goodenough, Synthesis and characterization of Sr2MgMoO6-delta - An anode material for the solid oxide fuel cell, J Electrochem Soc 153(7) (2006) A1266-A1272.

[100] L. Aguilar, S.W. Zha, Z. Cheng, J. Winnick, M.L. Liu, A solid oxide fuel cell operating on hydrogen sulfide (H2S) and sulfur-containing fuels, Journal of Power Sources 135(1-2) (2004) 17-24.

[101] Z. Cheng, S.W. Zha, L. Aguilar, M.L. Liu, Chemical, electrical, and thermal properties of strontium doped lanthanum vanadate, Solid State Ionics 176(23-24) (2005) 1921-1928.

[102] S. Zha, Z. Cheng, M. Liu, Gd2Ti2-XMoXO7-Based Anode Materials for H2S-Air Solid Oxide Fuel Cells, Ecs Transactions 1(7) (2006) 293-302.

[103] L. Blum, P. Batfalsky, Q. Fang, L.G.J. de Haart, J. Malzbender, N. Margaritis, N.H. Menzler, R. Peters, SOFC Stack and System Development at Forschungszentrum Jülich, J Electrochem Soc 162(10) (2015) F1199-F1205.

[104] V.D.M. ThyssenKrupp, Material Data Sheet, No. 4046, (2008).

[105] X. Montero, F. Tietz, D. Sebold, H.P. Buchkremer, A. Ringuede, M. Cassir, A. Laresgoiti, I. Villarreal, MnCo1.9Fe0.1O4 spinel protection layer on commercial ferritic steels for interconnect applications in solid oxide fuel cells, Journal of Power Sources 184(1) (2008) 172-179.

[106] S.M. Gross, D. Federmann, J. Remmel, M. Pap, Reinforced composite sealants for solid oxide fuel cell applications, Journal of Power Sources 196(17) (2011) 7338-7342.

[107] H. Timmermann, W. Sawady, R. Reimert, E. Ivers-Tiffée, Kinetics of (reversible) internal reforming of methane in solid oxide fuel cells under stationary and APU conditions, Journal of Power Sources 195(1) (2010) 214-222.

[108] M. Mayerhofer, P. Mitsakis, X.M. Meng, W. de Jong, H. Spliethoff, M. Gaderer, Influence of pressure, temperature and steam on tar and gas in allothermal fluidized bed gasification, Fuel 99 (2012) 204-209.

[109] C. Brage, Q. Yu, G. Chen, K. Sjöström, Use of amino phase adsorbent for biomass tar sampling and separation, Fuel 76(2) (1997) 137-142.

[110] R. Mücke, N.H. Menzler, H.P. Buchkremer, D. Stöver, Cofiring of Thin Zirconia Films During SOFC Manufacturing, J Am Ceram Soc 92(s1) (2009) S95-S102.

[111] F. Tietz, V.A.C. Haanappel, A. Mai, J. Mertens, D. Stöver, Performance of LSCF cathodes in cell tests, Journal of Power Sources 156(1) (2006) 20-22.

[112] L. Blum, L.G.J. de Haart, J. Malzbender, N. Margaritis, H. Menzler Norbert, Anode-Supported Solid Oxide Fuel Cell Achieves 70 000 Hours of Continuous Operation, Energy Technology 4(8) (2016) 939-942.

[113] L. Blum, Q. Fang, L.G.J. de Haart, J. Malzbender, N. Margaritis, N.H. Menzler, R. Peters, SOC Development at Forschungszentrum Jülich, Ecs Transactions 78(1) (2017) 1791-1804.

[114] M. Geis, S. Herrmann, S. Fendt, H. Jeong, C. Lenser, N.H. Menzler, H. Spliethoff, Coupling SOFCs to biomass gasification - The influence of phenol on cell degradation in simulated bio-syngas. Part I: Electrochemical analysis, Int J Hydrogen Energ (2018).

[115] H.G. Scott, Phase relationships in the zirconia-yttria system, J Mater Sci 10(9) (1975) 1527-1535.

[116] H. Tsubakino, M. Hamamoto, R. Nozato, Tetragonal-to-monoclinic phase transformation during thermal cycling and isothermal ageing in yttria-partially stabilized zirconia, J Mater Sci 26(20) (1991) 5521-5526.

[117] M. Ettler, H. Timmermann, J. Malzbender, A. Weber, N.H. Menzler, Durability of Ni anodes during reoxidation cycles, Journal of Power Sources 195(17) (2010) 5452-5467.

[118] M. Kubota, T. Okanishi, H. Muroyama, T. Matsui, K. Eguchi, Microstructural Evolution of Ni–YSZ Cermet Anode Under Thermal Cycles With Redox Treatments, 2015.

[119] F. Rosenburg, E. Ionescu, N. Nicoloso, R. Riedel, High-Temperature Raman Spectroscopy of Nano-Crystalline Carbon in Silicon Oxycarbide, Materials 11(1) (2018) 93.

[120] R.J. Nemanich, S.A. Solin, First- and second-order Raman scattering from finite-size crystals of graphite, Phys Rev B 20(2) (1979) 392-401.

[121] D. Papurello, A. Lanzini, S. Fiorilli, F. Smeacetto, R. Singh, M. Santarelli, Sulfur poisoning in Ni-anode solid oxide fuel cells (SOFCs): Deactivation in single cells and a stack, Chemical Engineering Journal 283 (2016) 1224-1233.

[122] P. Caliandro, S. Diethelm, J. Van herle, Triode Solid Oxide Fuel Cell Operation Under Sulfur-Poisoning Conditions, Fuel Cells 17(4) (2017) 457-463.

[123] C. Suciu, H. Tikkanen, I. Wærnhus, F. Goga, E. Dorolti, Water-based tape-casting of SOFC composite 3YSZ/8YSZ electrolytes and ionic conductivity of their pellets, Ceram Int 38(1) (2012) 357-365.

[124] A. C Müller, A. Weber, D. Herbstritt, E. Ivers-Tiffee, Long term stability of yttria and scandia doped zirconia electrolytes, 2003.

[125] M. Asadikiya, H. Sabarou, M. Chen, Y. Zhong, Phase diagram for a nano-yttria-stabilized zirconia system, Rsc Adv 6(21) (2016) 17438-17445.

[126] M. Salavati-Niasari, F. Davar, H. Emadi, Hierarchical nanostructured nickel sulfide architectures through simple hydrothermal method in the presence of thioglycolic acid, 2010.

[127] N. Feng, D. Hu, P. Wang, X. Sun, X. Li, D. He, Growth of nanostructured nickel sulfide films on Ni foam as high-performance cathodes for lithium ion batteries, Physical Chemistry Chemical Physics 15(24) (2013) 9924-9930.

[128] L.G.J. de Haart, J. Mougin, O. Posdziech, J. Kiviaho, N.H. Menzler, Stack Degradation in Dependence of Operation Parameters; the Real-SOFC Sensitivity Analysis, Fuel Cells 9(6) (2009) 794-804.

[129] P. Batfalsky, J. Malzbender, N.H. Menzler, Post-operational characterization of solid oxide fuel cell stacks, Int J Hydrogen Energ 41(26) (2016) 11399-11411.

[130] B. Novosel, M. Marinšek, J. Maček, Deactivation of Ni-YSZ Material in Dry Methane and Oxidation of Various Forms of Deposited Carbon, Journal of Fuel Cell Science and Technology 9(6) (2012) 061003-061003-7.

[131] D. Yoon, A. Manthiram, Hydrogen tungsten bronze as a decoking agent for long-life, natural gas-fueled solid oxide fuel cells, Energ Environ Sci 7(9) (2014) 3069-3076.

[132] K. Otsuka, H. Ogihara, S. Takenaka, Decomposition of methane over Ni catalysts supported on carbon fibers formed from different hydrocarbons, Carbon 41(2) (2003) 223-233.

[133] Y. Li, B. Zhang, X. Xie, J. Liu, Y. Xu, W. Shen, Novel Ni catalysts for methane decomposition to hydrogen and carbon nanofibers, J Catal 238(2) (2006) 412-424.

[134] K. Großmann, P. Treiber, J. Karl, Steam methane reforming at low S/C ratios for power-to-gas applications, Int J Hydrogen Energ 41(40) (2016) 17784-17792.

[135] S. Czernik, R. French, C. Feik, E. Chornet, Hydrogen by Catalytic Steam Reforming of Liquid Byproducts from Biomass Thermoconversion Processes, Industrial & Engineering Chemistry Research 41(17) (2002) 4209-4215.

[136] G. Garbarino, V. Sanchez Escribano, E. Finocchio, G. Busca, Steam reforming of phenol–ethanol mixture over 5% Ni/Al2O3, Applied Catalysis B: Environmental 113-114 (2012) 281-289.

[137] J.-P. Cao, P. Shi, X.-Y. Zhao, X.-Y. Wei, T. Takarada, Catalytic reforming of volatiles and nitrogen compounds from sewage sludge pyrolysis to clean

hydrogen and synthetic gas over a nickel catalyst, Fuel Process Technol 123 (2014) 34-40.

[138] S. Bebelis, A. Zeritis, C. Tiropani, S.G. Neophytides, Intrinsic Kinetics of the Internal Steam Reforming of CH4 over a Ni−YSZ−Cermet Catalyst−Electrode, Industrial & Engineering Chemistry Research 39(12) (2000) 4920-4927.

[139] L. Maier, B. Schädel, K. Herrera Delgado, S. Tischer, O. Deutschmann, Steam Reforming of Methane Over Nickel: Development of a Multi-Step Surface Reaction Mechanism, Top Catal 54(13-15) (2011) 845-858.

[140] S. Vivanpatarakij, D. Rulerk, S. Assabumrungrat, Removal of tar from biomass gasification process by steam reforming over nickel catalysts, 2014.

[141] X. Wu, Y. Tian, X. Zhou, X. Kong, J. Zhang, W. Zuo, D. Wang, X. Ye, Performance and long-term stability of nickel/yttria-stabilized zirconia anode-supported solid oxide fuel cell in simulated biosyngas, Energy 114 (2016) 1-9.

[142] Z. Jaworski, B. Zakrzewska, P. Pianko-Oprych, On thermodynamic equilibrium of carbon deposition from gaseous C-H-O mixtures: updating for nanotubes, Reviews in Chemical Engineering 33(3) (2017).

[143] T.B. Dörr, S. Schmidt, A. Drochner, H. Vogel, Catalytic Tar Removal from Bio-Syngas via Oxidation on Metal Oxide Catalysts, Chemical Engineering & Technology 40(2) (2017) 351-358.

[144] J.R. Rostrup-Nielsen, Conversion of hydrocarbons and alcohols for fuel cells, Physical Chemistry Chemical Physics 3(3) (2001) 283-288.

[145] S. Dierickx, J. Joos, A. Weber, E. Ivers-Tiffée, Advanced impedance modelling of Ni/8YSZ cermet anodes, Electrochim Acta 265 (2018) 736-750.

[146] K.T. Lee, N.J. Vito, M.A. Camaratta, H.S. Yoon, E.D. Wachsman, Effect of Ni-GDC AFL Composition on Performance of IT-SOFCs, Ionic and Mixed Conducting Ceramics 7 28(11) (2010) 151-163.

[147] S.R. Wang, T. Kobayashi, M. Dokiya, T. Hashimoto, Electrical and ionic conductivity of Gd-doped ceria, J Electrochem Soc 147(10) (2000) 3606-3609.

[148] A. Tsoga, A. Naoumidis, W. Jungen, D. Stover, Processing and characterisation of fine crystalline ceria gadolinia-yttria stabilized zirconia powders, J Eur Ceram Soc 19(6-7) (1999) 907-912.

[149] A. Tsoga, A. Gupta, A. Naoumidis, P. Nikolopoulos, Gadolinia-doped ceria and yttria stabilized zirconia interfaces: Regarding their application for SOFC technology, Acta Mater 48(18-19) (2000) 4709-4714.

[150] C. Lenser, H. Jeong, J. Sohn Yoo, N. Russner, O. Guillon, H. Menzler Norbert, Interaction of a ceria-based anode functional layer with a stabilized zirconia electrolyte: Considerations from a materials perspective, J Am Ceram Soc 101(2) (2017) 739-748.

[151] N.M. Sammes, Z.H. Cai, Ionic conductivity of ceria/yttria stabilized zirconia electrolyte materials, Solid State Ionics 100(1-2) (1997) 39-44.

[152] P.M. Delaforce, J.A. Yeomans, N.C. Filkin, G.J. Wright, R.C. Thomson, Effect of NiO on the Phase Stability and Microstructure of Yttria-Stabilized Zirconia, J Am Ceram Soc 90(3) (2007) 918-924.

[153] J. White, I.E. Reimanis, S. Menzer, G. Coors, The Enhanced Stabilization of the Cubic Phase in Yttria-Stabilized Zirconia with the Addition of Nickel Oxide, J Am Ceram Soc 94(7) (2011) 2030-2036.

[154] R. Mucke, N.H. Menzler, H.P. Buchkremer, D. Stover, Cofiring of Thin Zirconia Films During SOFC Manufacturing, J Am Ceram Soc 92(1) (2009) S95-S102.

[155] Q. Li, V. Thangadurai, Synthesis, Structure and Electrical Properties of Mo-doped CeO_2–Materials for SOFCs, Fuel Cells 9(5) (2009) 684-698.

[156] Q. Li, V. Thangadurai, A comparative 2 and 4-probe DC and 2-probe AC electrical conductivity of novel co-doped $Ce_{0.9-x}RE_xMo_{0.1}O_{2.1-0.5x}$ (RE = Y, Sm, Gd; x = 0.2, 0.3), J Mater Chem 20(37) (2010) 7970-7983.

[157] B. Mirfakhraei, V. Birss, V. Thangadurai, S. Paulson, K.E. Bere, F. Gitzhofer, Electrochemical Performance and H_2S Poisoning Study of Mo-doped Ceria (CMO) SOFC Anodes, Ecs Transactions 35(1) (2011) 1727-1734.

[158] Y. Chen, J. Bunch, C. Jin, C.H. Yang, F.L. Chen, Performance enhancement of Ni-YSZ electrode by impregnation of $Mo_{0.1}Ce_{0.9}O_2+\delta$, Journal of Power Sources 204 (2012) 40-45.

[159] Z.-R. Xu, J.-L. Luo, K.T. Chuang, The study of Au/MoS2 anode catalyst for solid oxide fuel cell (SOFC) using H2S-containing syngas fuel, Journal of Power Sources 188(2) (2009) 458-462.

[160] X. Hou, O. Marin-Flores, B.W. Kwon, J. Kim, M.G. Norton, S. Ha, Gasoline-fueled solid oxide fuel cell using MoO2-Based Anode, Journal of Power Sources 268 (2014) 546-549.

[161] S. Uhlenbruck, R. Nedelec, D. Sebold, H.P. Buchkremer, D. Stover, Electrode and Electrolyte Layers for Solid Oxide Fuel Cells Applied by Physical Vapor Deposition (PVD), Ecs Transactions 35(1) (2011) 2275-2282.

[162] H.Q. Wang, W.J. Ji, L. Zhang, Y.H. Gong, B. Xie, Y.S. Jiang, Y.Z. Song, Preparation of YSZ films by magnetron sputtering for anode-supported SOFC, Solid State Ionics 192(1) (2011) 413-418.

[163] J.C.J. Bart, N. Giordano, Phase Relationships in Cerium-Molybdenum Oxide System, J Less-Common Met 46(1) (1976) 17-24.

[164] L.H. Brixner, J.F. Whitney, M.S.L. Kay, Lattice-Parameters and Space Group of $Ce(MoO_4)_2$, J Solid State Chem 6(4) (1973) 550-552.

[165] K.J. Sreeram, R. Srinivasan, J.M. Devi, B.U. Nair, T. Ramasami, Cerium molybdenum oxides for environmentally benign pigments, Dyes Pigments 75(3) (2007) 687-692.

[166] A. Sobhani-Nasab, M. Maddahfar, S.M. Hosseinpour-Mashkani, $Ce(MoO_4)_2$ nanostructures: Synthesis, characterization, and its photocatalyst application through the ultrasonic method, J Mol Liq 216 (2016) 1-5.

[167] T.H. Etsell, S.N. Flengas, Electrical Properties of Solid Oxide Electrolytes, Chem Rev 70(3) (1970) 339-&.

[168] B.C.H. Steele, OXYGEN ION CONDUCTORS, High Conductivity Solid Ionic Conductors, WORLD SCIENTIFIC2013, pp. 402-446.

[169] N.Q. Minh, Ceramic Fuel-Cells, J Am Ceram Soc 76(3) (1993) 563-588.

[170] N. Trofimenko, M. Kusnezoff, A. Michaelis, Optimization of ESC Performance for Co-Electrolysis Operation, Ecs Transactions 78(1) (2017) 3025-3037.

[171] M. Kusnezoff, N. Trofimenko, M. Müller, A. Michaelis, Influence of Electrode Design and Contacting Layers on Performance of Electrolyte Supported SOFC/SOEC Single Cells, Materials 9(11) (2016) 906.

[172] Y.-H. Huang, R.I. Dass, J.C. Denyszyn, J.B. Goodenough, Synthesis and Characterization of Sr2MgMoO6 – δ : An Anode Material for the Solid Oxide Fuel Cell, J Electrochem Soc 153(7) (2006) A1266-A1272.

[173] G. Xiao, Q. Liu, X. Dong, K. Huang, F. Chen, Sr2Fe4/3Mo2/3O6 as anodes for solid oxide fuel cells, Journal of Power Sources 195(24) (2010) 8071-8074.

[174] S. Islam, J.M. Hill, Barium oxide promoted Ni/YSZ solid-oxide fuel cells for direct utilization of methane, J Mater Chem A 2(6) (2014) 1922-1929.

[175] K. Park, S. Lee, G. Bae, J. Bae, Performance analysis of Cu, Sn and Rh impregnated NiO/CGO91 anode for butane internal reforming SOFC at intermediate temperature, Renewable Energy 83 (2015) 483-490.

Band / Volume 447
TRENDS 2017
Transition to Renewable Energy Devices and Systems
D. Stolten, R. Peters (Eds.) (2018), 206 pp
ISBN: 978-3-95806-376-1

Band / Volume 448
3D simulation of impurity transport in a fusion edge plasma using a massively parallel Monte-Carlo code
J. Romazanov (2018), xvi, 149 pp
ISBN: 978-3-95806-377-8

Band / Volume 449
Projektbericht Adelheid – aus dem Labor heraus in die Lüfte
R. Peters, J. Pasel, R. C. Samsun, A. Tschauder, C. Wiethege, F. Scharf, D. Stolten (2018), xxi, 321 pp
ISBN: 978-3-95806-378-5

Band / Volume 450
Microstructure and Thermomechanical Properties of $SrTi_{1-x}Fe_xO_{3-\delta}$ Oxygen Transport Membranes and Supports
R. Oliveira Silva (2019), vi, 148 pp
ISBN: 978-3-95806-381-5

Band / Volume 451
Sodium Ion Conducting Ceramics for Sodium Ion Batteries
S. Naqash (2019), vii, 134 pp
ISBN: 978-3-95806-382-2

Band / Volume 452
Quantitative Analyse der Trocknungsverläufe von Katalysatordispersionen
F. Scheepers (2019), VIII, 191 pp
ISBN: 978-3-95806-384-6

Band / Volume 453
Neue Optionen für einen wirtschaftlichen Betrieb von Wasserstoffzügen durch Nutzung der LOHC-Technologie?
P. Wasserscheid, T. Grube, D. Sternfeld, M. Essl, M. Robinius, D. Stolten (2019), II, 88 pp
ISBN: 978-3-95806-386-0

Band / Volume 454
Reformierung von BtL-Kraftstoffen für die HT-PEFC in luftfahrttechnischen Systemen
C. Wilbrand (2019), IV, 312 pp
ISBN: 978-3-95806-387-7

Schriften des Forschungszentrums Jülich
Reihe Energie & Umwelt / Energy & Environment

Band / Volume 455
Entwicklung von thermischen Spritzprozessen für fortschrittliche Schutz- und Funktionsschichten
G. Mauer (2019), vi, 57 pp
ISBN: 978-3-95806-388-4

Band / Volume 456
Columnar Structured Thermal Barrier Coatings Deposited by Axial Suspension Plasma Spraying
D. Zhou (2019), VI, 126 pp
ISBN: 978-3-95806-391-4

Band / Volume 457
Modellierung zeitlich aufgelöster Ladeenergienachfragen von batterie-elektrischen Fahrzeugen und deren Abbildung in einem Energiesystemmodell
J. F. Linßen (2019), VIII, 189 pp
ISBN: 978-3-95806-395-2

Band / Volume 458
Synthesis and Analysis of Spinel Cathode Materials for High Voltage Solid-State Lithium Batteries
A. Windmüller (2019), iv, 142 pp
ISBN: 978-3-95806-396-9

Band / Volume 459
Monazite-type ceramics as nuclear waste form: Crystal structure, microstructure and properties
Y. Arinicheva (2019), 194 pp
ISBN: 978-3-95806-397-6

Band / Volume 460
Coupling a Solid Oxide Fuel Cell with a Biomass Gasifier: Degradation Mechanisms and Alternative Anode Materials
H. Jeong (2019), II, 112 pp
ISBN: 978-3-95806-398-3

Weitere ***Schriften des Verlags im Forschungszentrum Jülich*** unter
http://wwwzb1.fz-juelich.de/verlagextern1/index.asp

Energie & Umwelt / Energy & Environment
Band / Volume 460
ISBN 978-3-95806-398-3

Mitglied der Helmholtz-Gemeinschaft

JÜLICH
Forschungszentrum